Bottom up Engineering of Group IV Color Centers in Nanodiamonds and Nanoscale Diamond Membranes by MPCVD

A thesis submitted for the degree of Doctor of Philosophy at

University of Technology Sydney

Faculty of Science

School of Mathematical and Physical Sciences

Author

Aleksandra Teresa TRYCZ

Supervisor

Prof. Igor AHARONOVICH

Co supervisors

A. Prof. Charlene LOBO

Dr Mehran KIANINIA

August 2021

Certificate of Original Authorship

I declare that this thesis has not been previously submitted for a degree nor has it been submitted as part of requirements for a degree except as fully acknowledged within the text. I confirm that:

- This work was done wholly while in candidature for a research degree at the University of Technology Sydney.
- Where the thesis is based on work done by myself jointly with others, I have made clear exactly what was done by others and what I have contributed myself.
- Where I have consulted the published work of others, the source is always clearly attributed. With the exception of such quotations, this thesis is entirely my own work.

This research is supported by an Australian Government Research Training Program Scholarship.

Signature of student:

Production Note:
Signature removed prior to publication.

Date: August 2021

Copyright notice

© Copyright by Aleksandra Teresa Trycz 2021. All rights reserved.

"It Always Seems Impossible Until It's Done".

Nelson Mandela

Dedication

To my loved ones

Acknowledgments

The 3.5 years of my Ph.D. have been the most beautiful, challenging, complicated, both happy and sad years of my life. On the one side, I have been offered an exciting opportunity to do a Ph.D. at UTS in Australia, and I started greatly, but in the meantime, my personal life went through a hurricane forcing me to make many difficult decisions. However, I wasn't totally alone and I discovered to be surrounded by marvellous people and many friends ready to help me at any time during my Ph.D. I consider myself very lucky.

Firstly, I would like to thank my supervisor Prof. Igor Aharonovich, for allowing me to undertake my Ph.D. and to be able to explore the interesting fields of diamond fabrication and nanophotonics. Thank you for your guidance, for being there for me while I was struggling to put my life together again, trying to do my best as a student and a single mum. Thank you for the top-up scholarship that allowed me to bring my baby back to Australia and continue my research. I would never be able to arrive that far without your support, mentorship and friendship, and I will be endlessly grateful. You have helped me to find the strength and to build up my resilience.

I would like to acknowledge my co-supervisors A. Prof. Charlene Lobo, Dr Mehran Kianinia and Prof. Milos Toth. Thank you for all of your support and help.

I would like to express my gratitude to the academic staffs –Dr Sejeong Kim and Dr Carlo Bradac who get involved in my projects and shared their invaluable experience.

I would like to express my gratitude to the technical staff of the Micro Analysis Unit (MAU), clean room, and vacuum lab. - Katie McBean for all the help in the lab, by training me on the various instruments, Geoff McCredie for his constant assistance around the MAU and vacuum labs. for maintaining, troubleshooting, and upgrading the facilities so I could have completed my experiments in time. I am also thankful to Mark Lockrey for his assistance with MAU equipment.

I would like to thank all my friends near and far: Moko, Sara, Iunia, Pavla, Daria, Ryan, Jacquie, and Mayna. Your friendship is precious and knowing all of you have made my life better.

A big thank you to all the fellow students at the MAU for creating a positive and joyful environment to work in, for all the support and laughter, even in the most difficult moments of my life. I was fortunate to work with many amazing people: Kerem Bray, Rodolfo Previdi, Mika Westerhausen, Connor Stewart, Johannes Fröch, Chi Li, Hanh Duong, Minh Nguyen, Noah Mendelson, Milad Nonahal and all the fantastic people from our group. Special thanks go to Blake Regan, who recently become ANFF Technical Coordinator. Your positivity, sense of humor, and your view of life helped me to handle many bad days. Your help in the lab was invaluable and your presence a joy.

To all my colleagues from level 5. Thank you for cheering me up so many times.

To my mother Teresa Trycz. Without you, I could not have been able to finish what I have started. Thank you for your unconditional love and support through all of the years, for your patience and help in raising my baby so I could have completed my Ph.D. degree. You left everything and moved to Australia without hesitation in the way I could have reached my dream. I will always be grateful.

To my brothers Sebastian and Marcin Trycz. Growing up together was a pleasure and a challenge sometimes, and I thank you guys for making me strong and resilient.

To Urso family: Emanuele, Raimonda and Alessio. You were my family for more than 12 years and I am grateful for your love and support.

In loving memory of Adriano Urso. It was a tragedy to lose you so early. I will always remember you as a brother, a friend and a genius/crazy jazz pianist.

Finally, to Hanna, my beautiful baby girl and the most important person in my life. I have to admit that it was extremely difficult to be a mum and a full-time Ph.D. student. I hope you will understand all the sacrifices I have done in these years and might be proud of me as I am always proud of you. This work is dedicated to you my darling.

List of Publications

Refereed journal publications

- K. Bray, B. Regan, **A. T. Trycz**, R. Previdi, G. Seniutinas, K. Ganesan, M. Kianinia, S. Kim, I. Aharonovich, "*Single crystal diamond membranes and photonic resonators containing germanium vacancy color centers*", ACS Photonics (2018), 5, 4817−4822.
- **A. T. Trycz**, B. Regan, M. Kianinia, K. Bray, M. Toth, I. Aharonovich, "*Bottom up doping of single crystal diamond membrane with germanium vacancy color centers*", Opt. Mater. Express 9, 4708-4715 (2019).
- B. Regan, S. Kim, A. Tu Huy Ly, **A. T. Trycz**, K. Bray, K. Ganesan, M. Toth, I. Aharonovich, "*Photonic devices fabricated from (111) oriented single crystal diamond*", InfoMat. 2020; 1–6.
- **A. T. Trycz** and M. T. Westerhausen, C. Stewart, M. Nonahal, B. Regan, M. Kianinia, I. Aharonovich, "*Controlled doping of GeV and SnV color centers in diamond using chemical vapor deposition*", ACS (2020).
- B. Regan, **A. T. Trycz**, J. Fröch, O. Cranwell Schaeper, S. Kim, I. Aharonovich, *"Nanofabrication of high* Q*, transferable, diamond resonators",* Nanoscale (2021).
- M. Nonahal, S. White, B. Regan, C. Li, **A. T. Trycz**, S. Kim, I. Aharonovich, M. Kianinia, "Bottom up synthesis of single crystal diamond pyramids containing germanium vacancy centres", Advanced Quantum Technologies (2021).
- **A. T. Trycz**, S. Kim, B. Regan, K. Bray, T. Odom, I. Aharonovich, "*Photoluminescence enhancement from SiV and GeV emitters embedded in single crystal diamond membranes*" manuscript in preparation.

Conference presentation (Poster)

- **A. T. Trycz** et al., "*Fabrication of diamond membranes with homogenous SiV, GeV and SnV color centers for photonic applications", 1st virtual TMOS retreat*, Sydney, December 2020.

Contents

Certificate of Original Authorship ..... **iii**

Copyright notice ..... **iv**

Acknowledgments ..... **vii**

List of Publications ..... **ix**

Refereed journal publications ix

Conference presentation (Poster) x

List of Figures ..... **xv**

List of Tables ..... **xxiv**

List of Abbreviations ..... **xxv**

Abstract ..... **xxvii**

Preface ..... **xxix**

Chapter 1 Introduction **1**

1.1 Research Motivation 1

1.2 Research Objectives 3

1.3 Thesis Outline 5

Chapter 2 Background and Literature Survey **9**

2.1 Diamond structure and photophysical properties 12

2.2 Classification of diamonds 15

2.3 The synthesis of diamond 16

2.3.1 High Pressure High Temperature (HPHT) synthesis 18

2.3.2 Chemical Vapor Deposition (CVD) growth 19

2.4 Diamond for photonic applications and single photon sources 19

2.5 Color centers in diamonds....23
2.5.1 Nitrogen vacancy defect....27
2.5.2 Group IV color centers in diamonds....29
Chapter 3 Fabrication and characterization methods....35
3.1 Microwave Plasma Chemical Vapor Deposition....37
3.1.1 Surface chemistry during the diamond growth by MPCVD....41
3.2 Inductively Coupled Plasma Reactive Ion Etching....45
3.3 Devices patterning and fabrication....48
3.3.1 Electron Beam Lithography....48
3.4 Confocal Microscope Spectroscopy....49
3.5 Scanning Electron Microscopy....51
3.6 Atomic Force Microscopy....54
3.7 Raman Spectroscopy....55
Chapter 4 Growth and doping of NDs by MPCVD....57
4.1 Introduction....57
4.2 Growth and characterisation....57
Chapter 5 Bottom up doping of single crystal diamond membranes with germanium vacancy color centers....61
5.1 Abstract....61
5.2 Introduction....62
5.3 Experimental section....63
5.3.1 Metallic germanium as a precursor....65
5.3.2 Germanium dioxide as a precursor....66
5.3.3 Metallic germanium and germanium dioxide combination....67
5.4 Conclusions....71

Chapter 6 Single crystal diamond membranes and photonic resonators containing germanium vacancy color centers 73

6.1 Abstract 73

6.2 Introduction 74

6.3 Experimental section 75

6.3.1 Direct drop cast of germanium dioxide solution and metallic germanium source 75

6.3.2 Characterization of the membranes 76

6.3.3 PL measurements at room and cryogenic temperatures 78

6.4 Conclusion 83

Chapter 7 Controlled doping of GeV^- and SnV^- color centers in diamond using chemical vapor deposition 85

7.1 Abstract 85

7.2 Introduction 86

7.3 Results and discussion 87

7.4 Conclusion 94

Chapter 8 Plasmonic enhanced photoluminescence from SiV^- and GeV^- emitters embedded in single crystal diamond membranes 97

8.1 Abstract 97

8.2 Introduction 98

8.3 Results and Discussion 99

8.4 Conclusion 106

Chapter 9 Summary and Outlook 107

9.1 Summary and conclusions 107

9.2 Outlook and future directions 109

Bibliography 113

List of Figures

Figure 2.1. A diagram illustrating the worldwide estimated production of synthetic diamonds for the years 2009 - 2030. An estimated production in 2030 is expected to triple and exceed 19 million carats per year [70]. 10

Figure 2.2. A diagram showing the bandgap energies and lattice constants at room temperature for various direct and indirect bandgap semiconductors including ZnO, SiC, hBN, and diamond added for comparison [80]. 12

Figure 2.3. Some of the most common allotropes of carbon (structurally different forms of the same element) including graphene, nanotube, fullerene, graphite, and diamond. The capacity of carbon to form many different allotropes resides in its valency. 13

Figure 2.4. a) An sp^3 hybridized carbon atom in the diamond. b) A schematic of the diamond's crystallographic cubic structure. 13

Figure 2.5. Diamond classification based on the dimension of the crystal. 15

Figure 2.6. Classification of diamond substrates based on the level and type of chemical impurities. 16

Figure 2.7. Classification of diamond substrates based on the fabrication method. 17

Figure 2.8. Phase diagram of carbon displaying the regions for the natural (highlighted in green), HPHT (pink), and CVD diamond growth (blue region) [85]..... 17

Figure 2.9. a) A schematic diagram of a two-level, b) a three-level system, k_{xy} are the transition rates from level x to level y. c) An example of a $g^{(2)}(\tau)$ function where the blue curve denotes a single photon source with $g^{(2)}(0) < 0.5$. 22

Figure 2.10. Schematic diagram of a confocal microscope with a spectrometer and HBT interferometer to measure the second order autocorrelation function. 23

Figure 2.11. Point defects present in diamond lattice. Intrinsic point defects including a vacancy (missing carbon atom) or self-interstitial carbon. Extrinsic point defects are

based on foreign atom impurity in the lattice that can occupy a substitutional or interstitial position. 25

Figure 2.12. A spectral map of various single photon emitters found in diamond. The length of the bar indicates all emission for the centre, including phonon side bands. The value noted is the ZPL. The intrinsic carbon interstitials (TR12) has a ZPL of ~470 nm while the H3 consists of two nitrogen atoms with a vacancy with emission at 503 nm. An unidentified defect from the diamond, so-called ST1 centre is consists of a ZPL of ~550 nm and allows optical manipulation of its spin. The NiSi is a nickel-silicon complex with emission 760-770 nm. While this map is not a full representation of the all discovered photon emitters in diamond, it is an indication of the variation of known centres [80]. 26

Figure 2.13. An illustration of group IV element for visual comparison of empirical covalent atomic radii: carbon 70 pm (1 picometer = 1 x 10^{-12} m), silicon 110 pm, germanium 125 pm, tin 145 and lead 180 pm [106] 27

Figure 2.14. a) Crystallographic model of NV center in diamond, b) RT PL spectrum of neutral NV^0 and negatively charged NV^- nitrogen color centers. c) Electronic structure of the negatively charged NV center. 28

Figure 2.15. a) Crystallographic model of group IV color centers in diamond. b) A room-temperature PL spectrum for all group IV emitters [124]. 29

Figure 2.16. a) Energy structure of group IV color centers without and with the application of external magnetic field B. b) Predicted energies of the ground and excited states for all group IV emitters. 32

Figure 3.1. A schematic illustration that shows the main processes in diamond membrane fabrication: a) a high dose and high energy He^+ ions implantation (5 x 10^{16} ions/cm^2, 1 MeV) of the bulk diamond that creates the damaged layer 1.7 µm beneath the diamond surface shown in b). c) A high temperature vacuum annealing (at 900°C for 1 hour). d) Electrochemical etching to detach the formed membranes from the bulk diamond [168]. 36

Figure 3.2. a) Photo of the experimental setup employed for the liftoff. The electro-chemical etching was carried out using a constant forward bias of 60 V. b) Zoom image of the probes. During the etching, a positively biased tip in the contact with the top surface of the diamond while the negatively biased tip positioned above in close proximity. 37

Figure 3.3. a) MPCVD experimental setup ASTeX. b) Schematic of the CVD system [169]. 38

Figure 3.4. Picture of the puck with plasma ball during the overgrowth: a) symmetrical, centered on the substrate b) slightly moved on the side c) covering only part of the puck with sample partially uncovered underlying the importance of correct positioning of the puck inside the chamber. 40

Figure 3.5. LabView software interface for MPCVD ASTeX reactor. 41

Figure 3.6. a) Schematic processes and chemical reactions involved in the diamond growth. b) Chemical reactions involved during the MPCVD diamond process. The radicals are formed by gas ionization and transported to the surface to generate a pristine diamond layer. 43

Figure 3.7. a) Diagram of Reactive Ion Etching System (Oxford Instruments). b) ICP-RIE system used for etching and cleaning of the diamond surface. 46

Figure 3.8. SEM images of the diamond membrane at different steps of the fabrication process: a) as transferred, b) after 10 minutes of MPCVD overgrowth and c) after flipping and etching step (~ 300 nm thick). 47

Figure 3.9. Illustration of resolution limit with airy disk and corresponding wave front [190] 50

Figure 3.10. a) Schematic diagram of the scanning confocal microscope. b) Picture of the confocal setup employed in the experiments. 51

Figure 3.11. a) Schematic illustration of signals generated in a SEM by electron beam-sample interactions, and regions from which the different signals can be detected. b)

The Zeiss Supra 55VP SEM used to investigate the structural features, morphology, and quality of the fabricated samples. 53

Figure 3.12. Park XE7 AFM scanning probe microscope. The inset shows a zoomed image of the scanning probe. 54

Figure 3.13. Raman spectra and corresponding lattice vibration for a) a single crystal diamond and b) graphite [193] 56

Figure 4.1. a) Spray gun used for seeding of the sapphire substrates with ND suspension. b) A sapphire substrate showing well dispersed individual NDs after 10 min MPCVD growth. c) Examples of individual NDs zoomed to evidence the well faceted growth and good morphology (samples grown at 60 Torr, 1% CH_4, 900 W for 10 minutes). 58

Figure 5.1. a) Incorporation of Germanium during MPCVD growth of diamond. The precursors are dissociated in the plasma region, creating active species which will eventually incorporate into the growing diamond. b) Representative SEM image of a thick 1.7 µm and c) a thin diamond membrane ~ 300 nm. 64

Figure 5.2. Schematic illustration of three approaches for germanium incorporation into diamond membranes by MPCVD using solid precursors: a) metallic germanium, b) germanium dioxide, and c) a combination of both metallic and oxide sources. .. 64

Figure 5.3. Incorporation of GeV using metallic source. a) Schematic of the growth geometry of the diamond membrane and metallic sources. Inset, is the actual photograph of the puck with diameter of ~ 1 inch. b) Optical and c) SEM images of the membrane after overgrowth process in MPCVD. Visible square areas in SEM image is the result of secondary nucleation from micromasking with sputtered germanium during the growth. d) PL spectrum from the membrane after overgrowth did not show any peak at ~602 nm from GeV centers. 66

Figure 5.4. Incorporation of GeV using a germanium oxide source. a) Schematic of the growth geometry of the diamond membrane and oxide sources. Inset, is the actual photograph of the puck with diameter of ~ 1 inch. b) Optical and c) SEM images of the membrane after the overgrowth, resulting in smooth surface after the growth.

d) Room temperature PL spectrum of the membrane, with the peak centered at ~ 602 nm confirms the successful incorporation of GeV into the diamond membrane. 67

Figure 5.5. Incorporation of GeV using both metallic and oxide sources. a) Schematic of the growth geometry of the diamond membrane and metallic and oxide sources with larger distance compared to the previous approaches. Inset, is the actual photograph of the puck with diameter of 1 inch. The locations of both metallic and oxide germanium sources are marked. b) Optical and c) SEM images of the membrane after overgrowth process in MPCVD indicating the smooth surface after the growth. d) The pronounced peak at ~ 602 nm confirms the successful incorporation of GeV into the diamond membrane. 68

Figure 5.6. a) Room temperature PL spectra collected from three random position on the diamond membrane confirming the homogeneous incorporation of GeV into the diamond. b) An intensity confocal map from the membrane grown with the third method showing uniform distribution of GeV^- in all measured points across the membrane. c) Low magnification SEM image of the fabricated microring from diamond membrane containing GeV^- centers. d) PL spectrum from the diamond showing whispering gallery modes as well as GeV^- peak. Inset shows a zoomed image of one diamond ring. 70

Figure 6.1. Schematic illustration of the fabrication process to engineer single crystal diamond membranes containing GeV^- color centers. a) An electrochemically etched single crystal diamond membrane (dark grey) is transferred to a sapphire substrate using a 0.5 mg/mL GeO_2 solution in ethanol. b) Subsequent MPCVD overgrowth with an additional metallic germanium source nearby. c) The sample is flipped and thinned by ICP-RIE, to remove the original material to generate d) a diamond membrane with GeV^- centers (yellow). e), f) Representative SEM images of the overgrown and the final (thinned) diamond membrane, respectively. The thicknesses of the original and the thinned membrane are ~ 2.10 µm and ~ 0.3 µm, respectively. g) AFM scans of the surface roughness of the original (red curve), overgrown (black curve) and thinned

(dark blue curve) diamond membranes. The surface roughness of these membranes is ~1 nm. The curves are off-set in 1 nm intervals for clarity. 76

Figure 6.2. GeV^- incorporation into the membrane when only one metallic source is used. a) A confocal map of the membrane. b) Six typical spectra from points 1 – 6 in a). GeV^- is incorporated only at the edges. 78

Figure 6.3. Spectra of the diamond membranes doped with ensemble of GeV^- centers. a) A RT spectrum showing a characteristic peak at 602 nm. Inset, schematic structure of the GeV^- color center. b) A spectrum of the GeV^- ensemble taken at 15K (blue curve), with the characteristic splitting corresponding to the transitions from the excited to the ground state manifolds. The red dashed line is a double Lorentzian fit. Inset, is the schematic of the electronic level structure of the GeV^-. c) A confocal map of the overgrown diamond membrane where each number corresponds to a spectrum in d) showing the uniform distribution of the GeV^- emitters. d) Six representative RT spectra of the GeV emitters in the diamond membrane, showing a uniform distribution of the GeV^- emission.....79

Figure 6.4. Diamond microdisk and microring cavities fabricated from the overgrown diamond membranes containing GeV^- color ceters. a) Low magnification SEM image of microring and microdisk resonators with a diameter of 5 μm etched into the diamond membrane (blue dashed line). b), c) False color SEM images of a diamond microdisk and a diamond microring, respectively. The diamond are false colored blue for clarity. 81

Figure 6.5. a) PL spectrum recorded from the diamond microring cavity under 532 nm excitation at room temperature. WGMs are clearly visible. The ZPL of the GeV^- center is observed at 602 nm. Inset, a zoom in spectrum of the mode at 596 nm. The red line is a Lorentzian fit. b) a spectrum of a WGM at ~ 755 nm, showing a Q ~ 1500. c) Simulation data of the microring sample. Inset, FDTD field profile of the 1^{st} order mode. d) Comparison of emission from ensemble of GeV color centers recorded from a working microring where the GeV^- ensemble is coupled to the WGMs (blue curve), compared to a microring that does not show WGMs fabricated from the same membrane (black curve). 82

Figure 6.6. Lifetime of GeV ensembles in a) a coupled microring, b) membrane and c) comparison of the $Ge^{-}V$ signal only. The red curve is the pristine GeV^{-} while the blue one is the coupled ensemble. 83

Figure 7.1. Schematic diagram of dropcast dopant for the incorporation of group IV color centers in CVD diamond growth. a) Dopant solution diluted in ultrapure Milli-Q water and dropcast on sapphire substrate at 40°C and left to dry for 10 minutes to prepare the dopant coating shown in b). c) Diamond membranes or nanodiamonds are transferred to dopant coating. d) CVD overgrowth of diamond platform. The plasma conditions slowly release dopant ions into plasma for incorporation. e) Resultant overgrown diamond with incorporated group IV defects in diamond lattice. 88

Figure 7.2. Diamond growth quality for germanium doped nanodiamonds grown at 50 (a ,scale bar 100 µm), 60 (b ,scale bar 1 µm) , 70 (c ,scale bar 1 µm) and 80 Torr (d ,scale bar 1 µm). Inset, corresponding PL spectra with clear ZPL at ~ 601.0 nm a), 603.1 nm b), 603.1 nm c), and 603.9 nm d) corresponding to GeV^{-} color center. 89

Figure 7.3. Raman spectra of nanodiamonds grown at 70 Torr with germanium a) and tin precursors b). Raman peaks at ~1333 cm^{-1} with FWHM of ~ 12 nm are measured. 90

Figure 7.4. a) Optical image of the membrane after 10 min growth showing a smooth, high quality surface. Inset shows an SEM image of the membrane. b) Room temperature PL spectra comparison between edge and center of membrane (offset for clarity), with the ZPL centered at ~ 603.2 nm corresponding to the GeV^{-} emitters. 91

Figure 7.5. a) SEM images of the nanodiamonds after 10 min growth showing uniform distribution on the sapphire substrate. b) SEM image with high magnification shows the high quality diamond growth. c) Confocal PL map of the diamonds. d) Room temperature PL spectra of the NDs (offset for clarity), with peaks of ND-1,2 and 3 centered at 621.1 nm, 621.2 nm and 621.1 nm respectively corresponding to the ZPL of the SnV^{-}. 92

Figure 7.6. a) Optical images of the membrane after 10 min growth. Inset shows SEM image of the membrane with a smooth, high quality surface. The scale bar is 10 µm. b) Room temperature PL spectra comparison between edge and center of membrane (offset for clarity), with the peak centered at ~ 620 nm (emitter on the edge of the membrane) and ~ 619.4 nm nm (emitter in the middle of the membrane) confirms the successful incorporation of SnV^- into the membrane. 93

Figure 7.7. Raman data from diamond membranes grown with a) germanium and b) tin precursors. Both membranes show a strong Raman peak at ~1332 cm^{-1} indicating a high quality diamond growth. 94

Figure 8.1. a) Schematic illustration of metal nanodisk array on fused silica with a thin single crystal diamond membrane on top. b) SEM image of the plasmonic lattice consisting of Ag nanodisks spaced 500 nm on fused silica. The inset shows the photograph of the plasmonic device employed in the experiment. 100

Figure 8.2. Coupling between SiV^- emitter in the diamond membrane and a silver nanodisk array on fused silica with a resonance frequency that lies at ~ 740 nm. a) SEM image of single crystal diamond membrane after 8 min of MPCVD overgrowth on silicon dioxide substrate. The thickness of the membrane after growth is ~ 2.7 µm. The inset shows the SEM image of the plasmonic array with a scale bar of 500 nm. b) PL spectrum of a pristine (pink line) and coupled (blue line) SiV^- emitter. c) Typical time-resolved PL measurement from the pristine (pink circles) and coupled systems (blue squares). Solid lines are exponential fits. The measured lifetime values are τ_P = 1.18 ns and τ_C = 0.93 ns for the pristine and coupled emitter respectively. d) Comparison of PL intensity for 10 pristine (pink bars) and coupled (blue bars) SiV^- emitters. A 532 nm continuous- wave laser was used for PL measurements.....101

Figure 8.3. a) Comparison of the measured lifetime values for ten pristine (pink circles) and coupled (blue squares) SiV- emitters. We observe a small but consistent reduction in the lifetime when the sample is placed on the plasmonic nanodisk array evidenced by the mean value represented with dashed lines for pristine (pink line with the mean value of ~1.1 ns) and coupled (blue line with mean value of ~ 1 ns) color centers. b) Histogram of the lifetime measurements for 10 pristine (pink bars)

and c) coupled (blue bars) emitters. A 633 nm pulsed laser with a repetition rate of 10 MHz and 100 ps pulse width was used. 103

Figure 8.4. Coupling between GeV^- emitter in diamond membrane and a silver nanodisk array on fused silica with resonance frequency that lies at ~590 nm. a) SEM image of single crystal diamond membrane after 18 min of ICP-RIE etching. Thickness of the membrane after thinning is ~ 300 nm. b) PL spectra of a pristine (pink curve) and coupled (blue curve) GeV^- emitter. c) Time-resolved PL measurements from the pristine (pink circles) and coupled systems (blue squares). Solid lines are double exponential fits. The measured lifetime values are τ_P = 3.70 ns and τ_C = 3.27 ns for the pristine and coupled emitter respectively. A 405 nm continuous- wave laser was used in b) and 405 nm pulsed laser (0.5 mW) with a rotated 630 nm band pass filter was used in c). d) Fluorescence saturation curves obtained from the pristine (pink open circles) and coupled (blue open squares) systems. Pink and blue solid lines are fits obtained from the eq. $I_{sat} = I_{max}xP/(P + P_{sat})$ where I_{max} and P_{sat} are the maximum emission rate and excitation power at which saturation is reached, respectively. The value of 25 mW was the maximum for our system and the saturation condition was not reached. 105

List of Tables

Table 2.1. Optical, thermal, and mechanical proprieties of diamond and other relevant materials. E_g is the bandgap energy, E is the Young's modulus, κ is the thermal conductivity, ρ is the mass density, and c is the sound velocity [73, 74]. 11

Table 2.2. Diamond characteristics: electrical, optical, thermal, and mechanical properties of diamond [83-87] and their useful applications. 14

Table 2.3. Proprieties of ideal Single Photon Source [88]. 20

Table 2.4. Group IV color centers and their photophysical properties [22, 105, 125, 139, 142-147].....31

Table 5.1. Summary of the conditions used to achieve GeV color centres in thin diamond membranes. 69

List of Abbreviations

Abbreviation	Meaning
AFM	Atomic Force Microscope
APD	Avalanche Photo Diode
CL	Cathodoluminescence
CVD	Chemical Vapor Deposition
CW	Continuous Wavelength
FIB	Focused Ion Beam
FWHM	Full Width at Half Maximum
GaN	Gallium Nitride
GeV	Germanium Vacancy
HBT	Hanbury Brown and Twiss
HPHT	High Pressure High Temperature
ICP-RIE	Inductively Coupled Plasma - Reactive Ion Etching
IR	Infrared
MPCVD	Microwave Plasma Chemical Vapor Deposition
MW	Microwave
ND	Nanodiamond
NIR	Near Infra-Red

NV	Nitrogen Vacancy
PbV	Lead Vacancy
PL	Photoluminescence
QDs	Quantum Dots
QE	Quantum Efficiency
SCD	Single Crystal Diamond
SEM	Scanning Electron Microscopy
SiC	Silicon Carbide
SiV	Silicon Vacancy
SnV	Tin-Vacancy
SPE	Single Photon Emitter
SPS	Single Photon Source
SRIM	Stopping and Range of Ions in Matter
TEM	Transmission Electron Microscope
UV	Ultraviolet
ZPL	Zero Phonon Line

Abstract

Single crystal diamonds have emerged as important elements in a wide range of technological applications spanning from photonics, to sensing, quantum metrology, and computing boosted by the commercial availability of high-quality synthetic diamonds and improvements in nanofabrication methods.

This thesis responds to the current need to develop robust, cost-effective, and reliable protocols to engineer a homogeneous distribution of selected optically active defects (also called color centers or emitters) into nanoscale diamond membranes and nanodiamonds, and extensively investigates the introduction of group IV impurities (silicon, germanium, tin, and lead) while maintaining the highest possible material quality. The importance of group IV emitters has been demonstrated as they operate as photo-stable, single photon sources at room temperature and present suitable candidates for solid-state quantum applications.

The fabrication methods herein presented are based on a bottom up approach employing a microwave plasma chemical vapor deposition reactor with different types of doping precursors.

In this thesis I describe a detailed fabrication protocols that led to the generation of silicon, germanium, and tin vacancies into nanoscale single crystal diamond membranes and nanodiamonds using a combination of different precursors. The fabrication of different types of optical cavities from these membranes by electron beam lithography demonstrates the feasibility to grow high quality membranes that can be immediately processed for realization of photonic resonators with quality factors of Q ~ 1500, enabling superior light confinement and field enhancement. The doping processes are further improved by matching the melting temperature of the precursors to the plasma temperature reached during the growth. The main advantage of consists in the minute amount of dopants required (only 8 µL droplet), being often toxic and harmful, for the successful generation of emitters, making this method greener and safer for the operator and the environment.

Finally, I illustrate for the first time the feasibility to couple group IV emitters hosted in ~ 300 nm thick diamond membranes to plasmonic silver nanodisk arrays. The resulting photoluminescence intensity is increased by a factor of ~ 1.5 – 4, associated with a lifetime reduction achieving the resonant coupling of emitters with plasmonic lattices which enables a wide range of future applications for flat hybrid photonic-plasmonic systems based on color centers in diamonds.

My research opens the way for broader adaptation of doping protocols to engineer diamonds with color centers beyond the group IV elements showing the potential to accelerate the integration of solid-state emitters embedded in thin diamond membranes with scalable devices for photonic applications.

Preface

In this work, the ion implantation of bulk diamond with helium was performed in collaboration by K. Ganesan at the School of Physics at the University of Melbourne, Victoria, Australia.

In all circumstances, I actively participated in the experimental work design, performed the measurements, and analysed the data.

In certain places throughout this thesis, figures from other sources have been used and appropriate references have been inserted in the figure caption to acknowledge the sources of the figures.

Chapter 1 Introduction

1.1 Research Motivation

Nanoscale single crystal diamond (SCD) membranes and nanodiamonds (NDs) hosting optically active defects have emerged as prime candidates for many sensing and nanophotonic applications. The miniaturization of nanophotonics, a branch of nanotechnology that studies the light-matter interactions at the nanometer scale, has been the subject of intensive research in recent years with impressive fabrication at single component level [1]. Diamond, a remarkable material with exceptional and extreme properties [2], emerged as an important platform for many technological applications [3]. Some of the diamond's properties such as exceptional hardness, high thermal conductivity, chemical inertness, and electrical insulation have been highly exploited in different fields [4] to create optical elements, high energy beam combining amplifiers working in the kilowatt regime [5], heat spreaders [6, 7], spectroscopes for harsh environments [8, 9] and Raman lasers from DUV (deep ultraviolet) to mid-IR (infra red) [10-13] only to name a few from the myriad of existing and potential applications in the rapidly growing field of diamond-based technology.

For photonics-based applications, it is imperative to synthesize high-quality (type IIa or better) single crystal diamond substrates. While type II are pure diamonds with the content of chemical impurities below 5 ppm (parts per million), diamond for quantum application can reach the level of impurity concentration of less than 1 ppb (one part per billion). The higher performance of SCD is due to the absence of grain boundaries, making them more suitable for the aforementioned applications in comparison to the polycrystalline diamond (PCD), which show higher propagation loss due to the scattering at grain boundaries, strain and defects [14], surface roughness and higher background noise limiting the performance of photonic components and sensors. The development of diamond nanofabrication techniques has begun to realize structures such as nanophotonic components, including waveguides [15],

photonic crystals (PhC) [16], cavities [15], nanopillars [17-22], optical antennas, metalenses [23], solid immersion lenses (SIL) [24, 25] and other optical resonators for the manipulation, propagation, and trapping of the light. These structures embed the diamond emitters in cavity structures enhanced by the Purcell effect [26, 27]. Further research avenues, including nanomechanical systems such as nanoresonators [28, 29], allow high sensitivities in force detection while optomechanical systems are able to couple optical and mechanical modes [30, 31].

Significant work has been done to improve the nanofabrication methods, realizing different diamond structures from free-standing thin diamond membranes (~ 200 nm) [32]. The discovery of stable, solid-state single photon emitters (SPEs) which are the individual optically-active point defects hosted in SCD [33], have enabled a multitude of quantum technology applications in quantum optics [33], imaging [34], sensing [35-40], quantum metrology (temperature, strain, pressure, radiation, electric and magnetic fields sensing with nanoscale resolution [41]), quantum information [42-45], communication [46, 47], computing [43] and many other quantum technology applications [34, 48-50] comprehending a highly desirable realization of a quantum computer based on color centers in diamond [51] and the development of a quantum internet. For that purpose, multiplexed quantum repeaters or modular quantum computers based on solid-state spins have already been successfully demonstrated on a proof-of principle level[52].

Further, the employment of SCD membranes instead of bulk crystals offers the advantages of free-standing, optically isolated, scalable high-quality devices that can be thinned to the desired thickness (down to tens of nanometers) and transferred onto a substrate of choice for further processing [16] and fabrication of integrated photonic devices [53].

Many of the above-mentioned applications are based on the employment of diamond color centers and require stable, optically active emitters. The relevant findings illustrated throughout this thesis are on the forefront of diamond colour centre incorporation techniques, and lead towards large scale use of solid state diamond platforms for quantum applications.

1.2 Research Objectives

Despite the intensive research in diamond color centers and a myriad of possible applications, there were no available protocols for in situ doping with group IV color centers by CVD with total domination of ion implantation following high pressure high temperature synthesis of diamond.

Diamond has the capability to host hundreds of different emitters with interesting optical properties that can be generated either by ion implantation [54-58], high pressure high temperature (HPHT) [59-61] synthesis, or by chemical vapor deposition (CVD) [61], tailoring the fabrication method to the requested features and final applications. All the above-mentioned doping methods have their advantages and limitations. The ion implantation introduces the external atoms by bombardment, with associated damage to structure and reduces the overall quality of the crystal lattice [62] that cannot be fully recovered by subsequent high temperature annealing. However, ion implantation offers precise control on doping density, distribution, and depth, along with the ability to generate SPEs. HPHT cannot be used in nanometer-thick membranes as they are prone to break and fracture under the extreme conditions of pressure and temperature involved in the process; despite this it offers high material quality, which in turn improves the optical properties of incorporated group IV emitters. A bottom up CVD method is preferred for this work as it offers several advantages. The growth process generates a new pristine, homoepitaxial layer of diamond with improved optical and physical properties giving additional control over the doping process. While membrane fabrication is now an established and mature technology, homogeneous in-situ doping with new color centers is still a significant obstacle to overcome.

This thesis is devoted to the development of robust growth strategies for successful incorporation of fluorescent defects (color centers) in NDs and nanoscale diamond membranes by means of MPCVD and fabrication of devices for nanophotonic applications. Generating the high-quality SCD membranes, with uniform thickness of

~ 300 nm and embedded homogeneous distribution of group IV emitters have been of paramount importance for this project as they represent the fundamental building blocks for further photonic device fabrication. The thickness is critical for fabrication of optical waveguides and cavities and is chosen to satisfy the single-mode condition in the vertical direction (as a ratio between the operational vacuum wavelength and the refractive index of the diamond n = 2.4) necessary in cavity fabrication for our projects. All fabrication processes have been optimized, including growth, etching, transfer, and patterning of the membranes.

Group IV color centers have demonstrated room temperature, stable SPE; however, this work doesn't explicitly focus on this aspect of their emission. The presented methods are successful for fabrication of ensembles of group IV color centers that can find many applications in integration of these color centers into photonic devices such as resonators, waveguides, or photonic crystal cavities benefiting from the use of high-density ensembles to achieve a higher sensitivity. These applications rely upon the strong luminescence displayed by the ensembles compared to single defect emission, which can reduce photon-shot noise leading to the simplification and miniaturization of sensor systems. Single defects possess low transduction efficiencies being weakly coupled to the microwave and optical fields, and one of the approaches to overcome these limitations is to use ensembles of such emitters to enhance the coupling by a factor that is directly proportional to the number of emitters forming a collective superradiant state. One of the prominent examples of application of group IV ensembles of color centers is the germanium vacancy (GeV^-) based temperature sensor for optical nanothermometry implemented in the fiber-optic format that can reach resolution below 0.1 K in a wide range of temperatures [63].

Therefore, this work is focused on generation of high quality SCD membranes with superior optical properties that are the starting point for further fabrication of devices for nanophotonic applications with bottom up integration of selected, optically active fluorescent defects. All doping protocols were at the same time tested to grow NDs to prove the incorporation methods in nanosize diamond crystals.

1.3 Thesis Outline

The main effort of my experimental work has been devoted to developing a successful, robust, and reliable protocol for direct doping of NDs and SCD membranes with group IV emitters (such as silicon, germanium, tin, and lead). Several precursors have been tested in different aggregation states, starting with metallic dopants, oxides, and chloride powders, as well as various liquid suspensions of powder dopants in different concentrations. MPCVD has been employed to overgrow diamond material from either membrane or NDs. Through the controlled addition of inorganic precursors, designed specifically to match the reactive temperature of the CVD chamber (~1000°C), the successful direct incorporation of group IV elements has been achieved.

Furthermore, different combinations of precursors were investigated, requiring a consistent load of experimental testing, changing one parameter at each experiment varying the pressure, microwave (MW) power, the concentration of H_2 and CH_4 gases, time of the growth, pre-treatment of the substrates, employing membranes with different crystallographic orientation and doping (undoped 100 and 111 membranes and boron doped 100 membranes), as well as varying the sample holder dimensions (carbon puck). Metallic oxide and chloride suspensions have been demonstrated to be the most efficient precursor for homogenous distribution of ensemble color centers in thin diamond membranes and in NDs.

Room temperature confocal microscopy has been utilized to interrogate the quality and distribution of generated color centers after each successful doping, and line scans have been employed to confirm a homogenous distribution of emitters in the membranes. Diamond growth quality was demonstrated through Scanning Electron Microscopy (SEM) analysis in combination with Raman spectroscopy and Electron Backscatter Diffraction (EBSD) to confirm the continuation of single crystal direction during the overgrowth. Further, SEM and photoluminescence (PL) excitation studies have been undertaken to determine the quality of fabricated photonic crystal and

resonator devices, confirming the architecture quality and quality factor of emitted modes.

This thesis is organized in 9 chapters as follows:

Chapter 2 introduces diamond as a material, presenting its photo-physical properties, classification according to the impurity content or crystal size followed by the description of the two main synthesis methods. The examples of photonic applications of diamond are described underlying the importance of diamond emitters as robust, stable room temperature single photon sources describing theoretical aspects of and ideal single photon emitter. Following paragraph details the diamond color centers that work as SPS describing their photoluminescence properties and technological applications with the focus on group IV emitters.

Chapter 3 provides information about the experimental methods and the equipment employed during the fabrication of membranes and diamond nanodevices. The second section illustrates the equipment involved in diamond characterization to assess the quality of the growth and the properties of engineered emitters, followed by the description of NDs growth by MPCVD illustrated in Chapter 4.

The second part of the thesis details the experimental work undertaken during my PhD candidature that turned into publications and consists of four chapters.

Chapter 5 is the first experimental chapter of the thesis, which focuses on a comparative study for the bottom up generation of germanium color centers in SCD membranes using metallic and oxide solid precursors. After the investigation of performance of the fabricated membranes and emitters, the membranes are further processed to fabricate photonic resonators in form of microrings. Significant portions of this chapter are copied verbatim from the peer-reviewed article: “Bottom up doping of single crystal diamond membrane with germanium vacancy color centers”, Opt. Mater. Express 9, 4708-4715 (2019).

Chapter 6 details methods to generate germanium vacancies in SCD membranes employing metallic germanium and germanium oxide solutions drop cast directly on the membrane. Significant portions of this chapter are copied verbatim from the

peer-reviewed article: “Single Crystal Diamond Membranes and Photonic Resonators Containing Germanium Vacancy Color Centers”, ACS Photonics (2018), 5, 4817−4822.

In Chapter 7, oxide and chloride solutions are used to create a coating doping layer on the substrate which is a source of precursors for NDs and SCD membranes. Significant portions of this chapter are copied verbatim from the peer-reviewed article: “Controlled doping of GeV and SnV color centers in diamond using chemical vapor deposition”, ACS (2020).

Chapter 8 demonstrates for the first time the feasibility to couple silicon and germanium vacancies engineered in nanoscale, high quality SCD diamond membranes to plasmonic silver nanodisk array achieving the enhancement of ~ 1.5 - 4 in PL signal associated with a lifetime reduction for both types of emitters. Significant portions of this chapter are copied verbatim from the manuscript in preparation: “Photoluminescence enhancement from SiV and GeV emitters embedded in single crystal diamond membranes”.

Finally, Chapter 9 gives the summary of the work and thesis contributions and discusses the perspectives and outlook for further extension of all doping and fabrication methods.

Chapter 2 Background and Literature Survey

In ancient Greek diamond (*αδάμας adámas*), means "proper", "unalterable" or "unbreakable" and throughout history, it has been a prized material, holding a unique position of prominence as a measurement of wealth and beauty. Natural diamonds are one of the rarest and most expensive minerals thus their industrial uses were very limited until synthetic fabrication methods were developed. The price of 1 carat natural diamond may vary between 1k and 16k US dollars depending on many factors that influence diamond's quality and color. However, we are approaching a third decade where diamond is highly appreciated not only as desirable gem stone to the general public but emerged as a fascinating object both for science and industry because of its outstanding mechanical, thermal, electrochemical, electronic, and optical properties [4]. Modern uses of diamonds like drilling, mining and precision machining applications increased rapidly since 1955 when the first synthetic diamonds were produced by HPHT techniques at an industrial scale [64]. Nowadays, the application of synthetic or lab-grown diamonds spans fields such as material science, medicine, optics, photonics, and quantum computing.

An estimated world production of synthetic diamonds for only the year 2021 is 7.4 million carats, and the industrial production is expected to grow rapidly in the next decade as shown in Figure2.1. exceeding 19 million carats in 2030, which will result in a revenue surpassing 30 billion of U.S. dollars per year. Such a strong and established industrial production of millions of carats per year and commercial availability of synthetic diamonds of high quality and purity, with different size and crystal orientation from several companies (e.g., Applied Diamond Ink. [65], AuDiaTec [66] and Element 6 [67]) has led to the explosion of interest in the application of diamond to important twenty-first-century technologies and boosted the worldwide research in diamond-based technology as a part of fourth industrial revolution [68].

Lab-grown diamonds, also known as synthetic diamonds, man-made diamonds, and cultured diamonds, possess the same physical properties of natural diamonds

utilizing synthetic technologies to effectively replicate the natural formation process. A key advantage of synthetic diamonds is the processing time, considering that synthetic diamonds can be grown in one to four weeks, depending on their size, instead of taking 1 - 3 billions of years to form like natural diamonds. The extreme control over the quality and purity of lab-grown diamonds can be tailored to specific applications, for instance, with quantum grade diamonds being recently synthesised [69], while it also enables features such as isotopic engineering, which is not possible through other means.

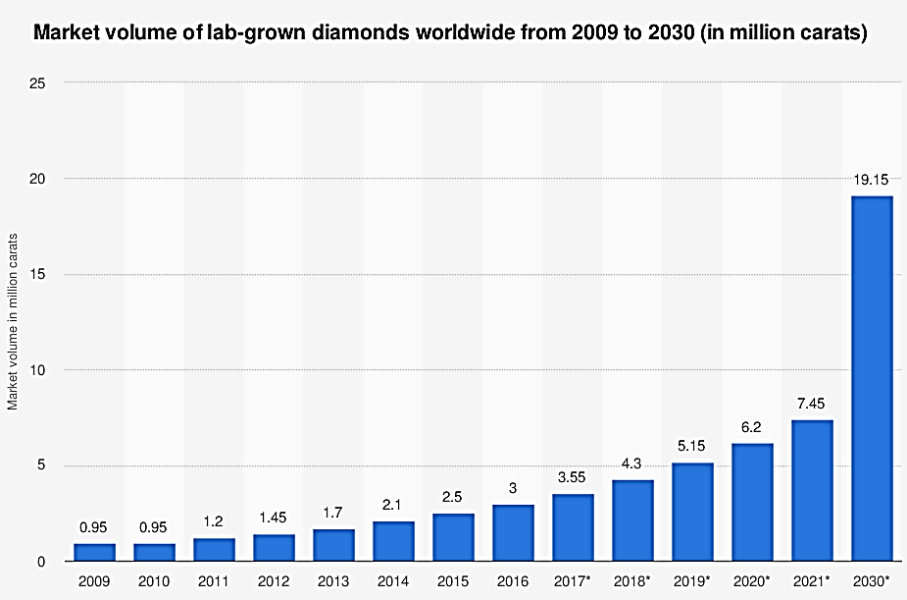

Figure 2.1. A diagram illustrating the worldwide estimated production of synthetic diamonds for the years 2009 - 2030. An estimated production in 2030 is expected to triple and exceed 19 million carats per year [70].

In the last two decades, synthetic diamonds have been extensively studied as a platform for modern communication and information technology [71], and have the potential to surpass the material quality of 20th-century silicon and silica-based technologies due to the difficulties of silica translating into the quantum regime [71, 72]. The improvement of growth and doping techniques of synthetic diamonds have allowed the development of new engineering materials for advanced mechanical,

electronic, optical, and thermal applications by taking advantage of some of the diamond's extreme photo-physical proprieties. Some of the properties of diamond are illustrated in Table 2.1. in comparison to other common materials employed in nanofabrication and photonics, such as gallium nitride (GaN), zinc oxide (ZnO), and others.

	E_g (eV)	Refractive index (n)	Transmission window (µm)	E (GPa)	κ (W/mK)	ρ (g/cm^3)	c (m/s)
Diamond	**5.47**	**2.4**	**0.22 - 20**	**1100**	**2200**	**3.52**	**17700**
Si	1.12	3.5	1.1 – 6.5	162	140	2.33	8300
SiO_2	9	1.5	0.38 – 2.2	95	10	2.65	6000
Sapphire	9.9	1.8	0.17 – 5.5	340	24	3.98	9200
GaN	3.44	2.4	0.36 – 7	294	130	6.1	6900
GaAs	1.42	3.7	0.9 – 17.3	116	52	5.32	4700
ZnO	3.4	2	0.37 – 1.5	110	30	5.6	4400
TiO_2	3.5	2.5	0.42 - 4	250	10	4.26	7700

Table 2.1. Optical, thermal, and mechanical proprieties of diamond and other relevant materials. E_g is the bandgap energy, E is the Young's modulus, κ is the thermal conductivity, ρ is the mass density, and c is the sound velocity [73, 74].

Some of the additional characteristics of this remarkable material are: a high refractive index (~ 2.4), strong optical nonlinearity (Kerr and Raman), large optical bandgap of ~ 5.5 eV, excellent thermal conductivity [75] with low thermal expansion, high carrier mobility, and a high breakdown voltage. Figure 2.2 shows diamond's band gap and lattice constant at room temperature in comparison to different semiconductors commonly employed in nanotechnology. However, the high refractive index of diamond makes the light extraction challenging and requires the fabrication of devices (e.g., waveguides, one and two-dimensional photonic cavities, pillars, ring resonators [15, 76-78]) to enhance the light collection efficiency. A feature

important in many biological applications is diamond's biocompatibility and chemical inertness which make it a suitable material for use in biomedical device industry in prostheses, sensing, imaging, drug delivery, biological engineering, bone repair, brain research, and other health care applications [79].

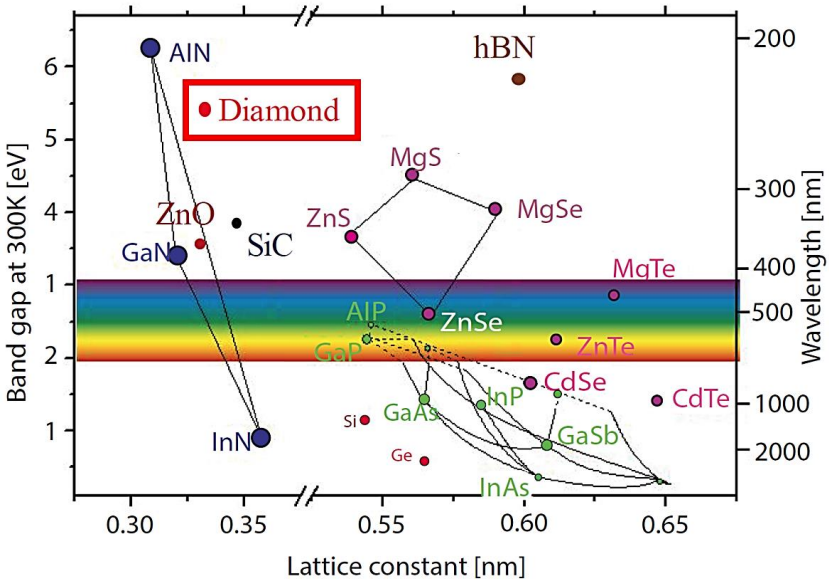

Figure 2.2. A diagram showing the bandgap energies and lattice constants at room temperature for various direct and indirect bandgap semiconductors including ZnO, SiC, hBN, and diamond added for comparison [80].

2.1 Diamond structure and photophysical properties

Diamond is one allotrope of carbon (Figure 2.3.), and its crystal structure consists of the only sp^3 hybridized carbon atoms, each forming a tetrahedral symmetry with four other neighbors carbons with an angle of 109.5° between each of the hybrid orbitals [81] as shown in Figure 2.4a. The nearest-neighbor bond length is 0.154 nm which is the shortest of any three-dimensional crystal, leading to a highly compact structure with a relatively large atomic density (3.5 g/cm^3). The strong covalent bonds between the different carbon atoms ensure a very high binding energy (~ 347 kJ/mol), making the diamond one of the hardest known material on the Mohs scale. According to

Hermann Mauguin geometry notation, the diamond is classified as Fd3m-07_h or as face-centered cubic (FCC) Bravais lattice. It can be viewed as two superimposed FCC lattices, one displaced relative to the other along a body diagonal by one-quarter of the lattice parameter, and is schematically illustrated in Figure 2.4b.

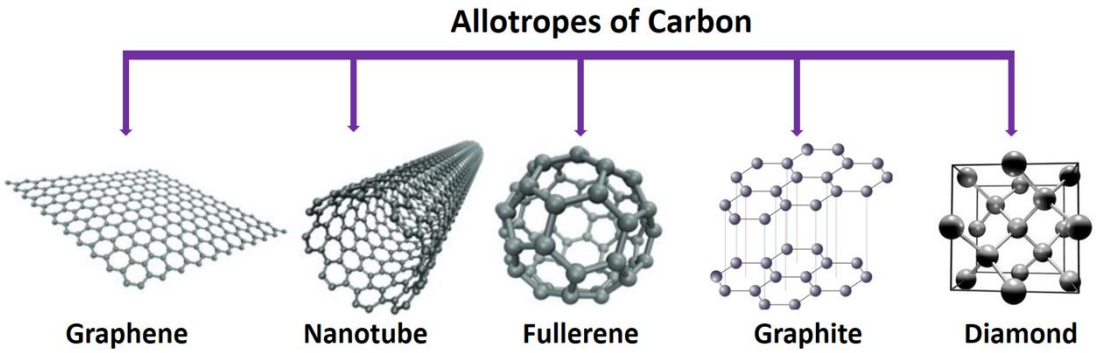

Figure 2.3. Some of the most common allotropes of carbon (structurally different forms of the same element) including graphene, nanotube, fullerene, graphite, and diamond. The capacity of carbon to form many different allotropes resides in its valency.

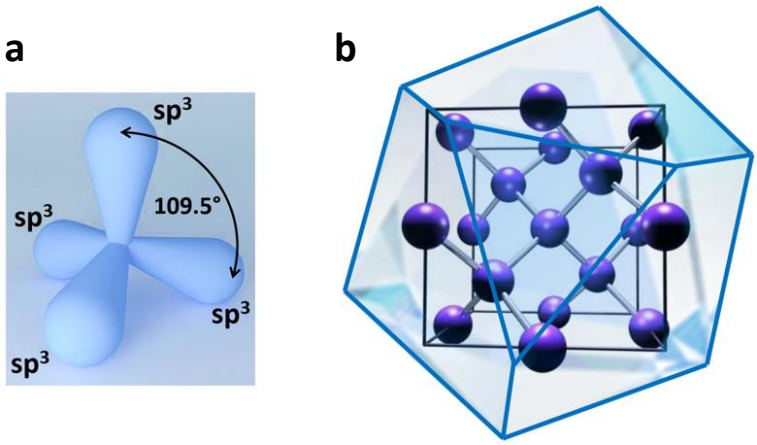

Figure 2.4. a) An sp^3 hybridized carbon atom in the diamond. b) A schematic of the diamond's crystallographic cubic structure.

Diamond represents an extreme form of atomic aggregation in nature, possessing a multitude of exceptional properties, including high optical transparency, extreme mechanical hardness, chemical inertness, and many potential applications of the

diamonds are strongly dependent on their purity and crystallinity [2]. Main diamond features are summarized in Table 2.2. with possible technological applications.

Another important feature of diamond's crystal lattice is almost a total lack of nuclear spins as ^{12}C, the most abundant carbon isotope (98.9%), possesses no nuclear spin [69, 82]. This leads to low magnetic noise (if the concentration of paramagnetic impurities is kept low) and long coherence times, even at room temperature.

Properties	Values	Applications
Wide bandgap, E_g (eV)	~ 5.5	High temperature operation
High thermal conductivity, (W/cm·K)	24	Heat spreaders
High electric breakdown, E_c (kV/cm)	10000	High power electrical devices
Electrical resistivity (Ω·cm)	10^{14} – 10 [16]	Good electrical insulator
High bond strength	5.8 x 10^{19} J per bond	Radiation detectors
Wide spectral transparency	~ 71% from UV (225 nm) to far IR	Transmission components, high power laser windows
High thermal conductivity Low loss tangent (tan δ)	n = 2.6 at 266 nm, n = 2.46 at 405 nm	Output gryotron windows

Table 2.2. Diamond characteristics: electrical, optical, thermal, and mechanical properties of diamond [83-87] and their useful applications.

Diamond has the capability to contain a huge variety of color centers and more than 500 have already been discovered originating from defects or foreign impurities embedded in the crystal lattice. Some of these defects possess a very important characteristic to act as single photon sources [88, 89]. This topic is covered in more detail in § 2.5.

2.2 Classification of diamonds

The classification of diamonds may be based on different criteria like crystal dimension, production method, or the level and type of chemical impurities hosted in the lattice.

According to the crystal size we can distinguish two main categories: polycrystalline diamonds and single crystal diamonds. Polycrystalline diamond can be further divided into three groups according to the difference in the size of crystallities: a) microcrystalline, b) nanocrystalline, and c) ultrananocrystalline diamond [90, 91], all of which are shown in Figure 2.5. with their respective crystal dimensions.

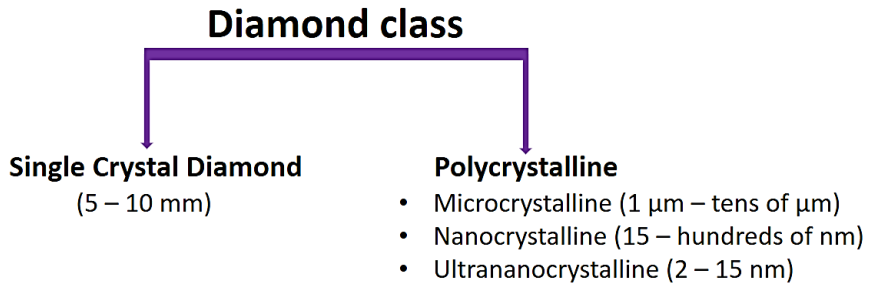

Figure 2.5. Diamond classification based on the dimension of the crystal.

Nanodiamond (ND) is a term referred to diamond crystals with structures of less than 100 nm in size. There are different techniques to synthesise bulk diamonds and NDs and the most common are ND detonation, high pressure high temperature (HPHT), which transforms sp^2 carbon in sp^3 diamond, and chemical vapor deposition (CVD) growth. The last two processes will be described in more detail in paragraph 2.3.

Initially, natural diamonds were divided into two groups I and II according to the content of nitrogen and later with the improvement of investigation techniques these classifications have been extended.

More than 95% of natural diamonds are rich in nitrogen (N >5 ppm up to 3000 ppm (parts per million)) as their formation occurs in the air; diamonds fitting these specifications belong to the category I. This group can be further separated into subclass Ia where (N is present in aggregates with concentration ~ 2000 ppm assuming a yellow color) and Ib (with single, isolated substitutional nitrogen). The diamond subdivision based on impurity content is shown schematically in Figure 2.6.

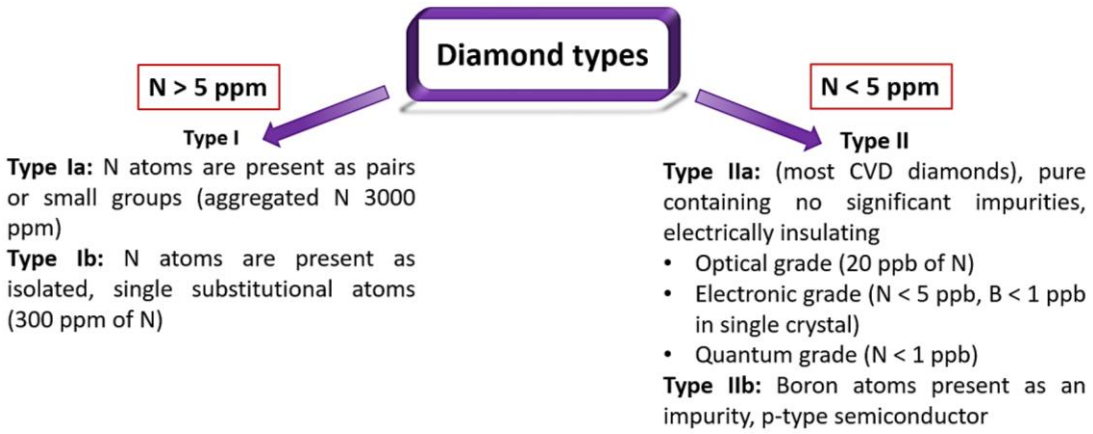

Figure 2.6. Classification of diamond substrates based on the level and type of chemical impurities.

Diamonds that belong to type II, are pure crystals that do not contain any significant impurities (N < 5 ppm). Most of the CVD industrial diamonds fall into this category and the improvements in fabrication methods required a further division of CVD diamonds into optical grade, electronic grade, and recently a quantum grade diamonds [69]. Type IIb diamonds contain significant amounts of boron as a dopant, making the diamond a p-type semiconductor and giving the crystals a blue coloration.

2.3 The synthesis of diamond

Diamonds form naturally in a slow process that can take up to 3 billion years. At a depth within the earth of ~200 km, the pressure is high (70 - 80 kbar) and temperatures can reach 1400 - 1600°C. Such formed diamonds can be brought to the

surface by volcanic or seismic activity generated by the movement of the Earth's tectonic plates [85] and successively extracted. The classification of diamond substrates based on the fabrication method is schematically illustrated in Figure 2.7.

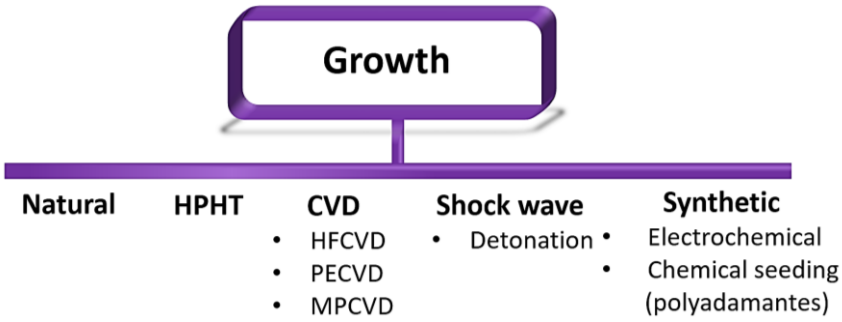

Figure 2.7. Classification of diamond substrates based on the fabrication method.

Lab-grown diamonds possess the same physical properties of natural ones and the two main production methods at industrial scale are high pressure high temperature (HPHT) [60] synthesis and chemical vapor deposition (CVD) [61] growth. The carbon phase diagram in Figure 2.8. schematically illustrates the main regimes for diamond synthesis in function of the pressure and the temperature.

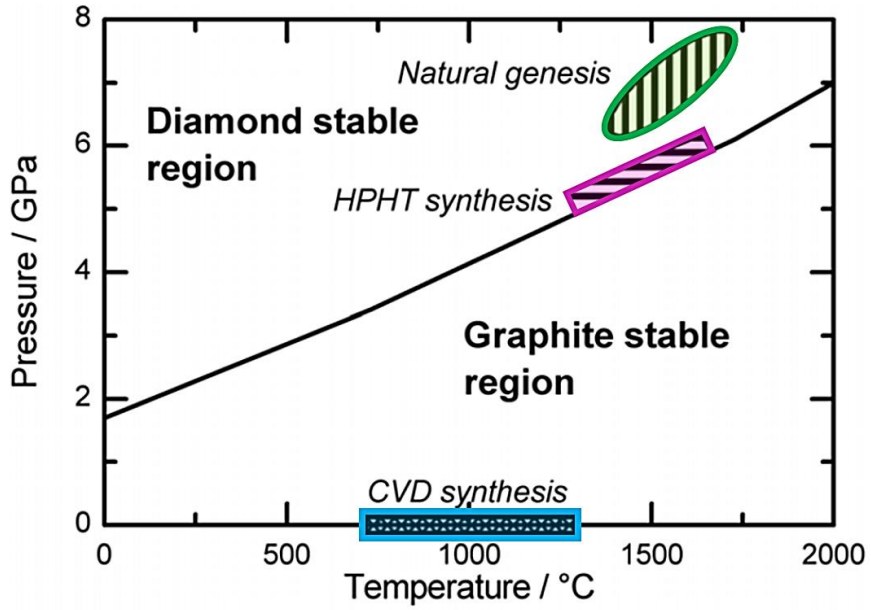

Figure 2.8. Phase diagram of carbon displaying the regions for the natural (highlighted in green), HPHT (pink), and CVD diamond growth (blue region) [85].

2.3.1 High Pressure High Temperature (HPHT) synthesis

Since the discovery at the beginning of the 19th century that diamond is an allotrope of carbon, there have been many attempts to try to convert graphite into diamond. Thermodynamic calculations established that at ambient conditions of temperature/pressure, the stable allotrope is graphite while diamond is in a metastable state, and the idea to apply high temperature and high pressure mimicking the natural diamond formation process led to the first diamond synthesis by HPHT in 1955 [92]. HPHT methods are widely employed in industry and can be divided into four categories: solubility-gradient method, where molten metals such as Fe, Ni or Co are added to solve the graphite at HPHT, temperature gradient, no-catalyst conversion, and shock compression methods [59, 93]. Generally high pressures of hundreds of kilo bar and two thousand degrees of temperature along with solvent and catalyst metals necessary to break strong carbon bonds were used to grow first synthetic diamond crystals. The catalysts used in the process, along with high concentration of nitrogen from the air ~ 100 ppm (type Ib diamond, yellow or amber color), contributed to diamond contamination. The quality and morphology of diamonds depends strongly on temperature and pressure with the possibility to achieve extremely low dislocation density [94]. This process makes it difficult to manage impurity incorporation and impurities are usually inhomogeneously distributed leading to local variations in material properties [95]. Although, this process, can brighten some of the group IV emitters (by making the emission lines narrower) and has been greatly refined over the past years resulting in diamond IIa quality, it remains a complicated process requiring high equipment maintenance costs. Furthermore, this method is only applicable to the bulk and nanoparticles being unsuitable for thin membrane doping and the final size of the diamond is limited by the growth apparatus making this method unsuitable for wafer production and large-scale integration.

2.3.2 Chemical Vapor Deposition (CVD) growth

Diamond can be also grown in its metastable regime by CVD which requires much lower pressure and temperature compared to HPHT. During this process complex chemical reactions occur on the surface which fuse the deposited material with the structure of the substrate [96]. The main advantages of this method are low maintenance prices due to simplicity of the process, high reproducibility, and flexibility in controlling dopants. CVD is routinely employed in microfabrication, depositing various materials as monocrystalline, polycrystalline, amorphous, and epitaxial structural forms. While there are many forms of CVD which use heat (thermal CVD) or radiation sources (UV photo assisted CVD), at low (Low Pressure CVD, LPCVD) or atmospheric pressure (Atmospheric Pressure CVD, APCVD), the best method for the fabrication of diamond is plasma enhanced CVD (PECVD). This method is also used by diamond manufacturers to achieve high purity CVD bulk diamonds for commercial purchase.

A microwave plasma chemical vapor deposition (MPCVD) synthesis has been used in this work, therefore this type of reactor will be described in more detail in Chapter 3.

2.4 Diamond for photonic applications and single photon sources

Thanks to the development of new technologies, that allow a controlled introduction into the synthetic diamond lattice of various impurities and defects, new colour centres can be used as the components for optically active emitters in integrated quantum nanophotonics.

Over 500 different colour centres are known to exist in diamonds and due to the large bandgap the emission from the colour centres can escape without absorption from

the crystal. The recent explosion of interest of researchers towards diamonds is due to the fact that some of these colour centres possess characteristics that make them bright Single Photon Sources (SPSs)[88, 89] at room temperature. Table 2.3 illustrates some of the properties of an ideal SPS.

Application	Main requirement
Linear optical quantum computing	Photons with identical spectral properties
Single- photon-based quantum cryptography	Polarization and high repetition rate
Bio-marking	Clear emission spectrum
Practical scalable photonic technologies	High coupling efficiency, photons of certain spatial modes

Table 2.3. Proprieties of ideal Single Photon Source [88].

SPSs can be approximated as a two-level system without a metastable state, narrow PL linewidth (with the luminescence concentrated mostly in the zero phonon line (ZPL)), photostable emission without blinking or bleaching, short excited state lifetimes between pico and nano seconds, and polarization in absorption and emission.

Photoluminescence from optically active defects in diamond has been studied for years [88, 97]. It is based on a bright laser excitation of an electron in the colour centre from its electronic ground state to above the lowest excited level. As this state quickly relaxes vibronically to an excited state. Soon the emitter returns to the ground state emitting a photon with emission energy given by Equation 2.1.:

$$\hbar\omega = E_{|e\rangle} - E_{|g\rangle} \tag{2.1}$$

PL involves the transitions between the ground and excited states of the emitter with no interactions with the valance and conduction band of the material considering it as an isolated atom-like system.

The second order autocorrelation function, $g^{(2)}(\tau)$ commonly employed to describe the photon statistics of the emitted light, measures in terms of the probability the detection of a photon at a delay time of τ as follows:

$$g^{(2)}(\tau) = \langle I(t)I(t+\tau)\rangle / \langle I(t)\rangle^2 \tag{2.2}$$

where $\langle\ \rangle$ stands for the expectation values and I = the intensity of the photon. Furthermore, this equation determines the single photon emission.

At the zero-time delay $\tau = 0$, the function $g^{(2)}(0)$ can be simplified resulting in:

$$g^{(2)}(0) = \frac{n(n-1)}{n^2} \tag{2.3}$$

The equations below show the possible solutions to the second order correlation function $g^{(2)}(\tau)$ and the statistics of the corresponding light source.

$$g^{(2)}(0) = \begin{cases} g^{(2)}(0) > 1 & \text{Chaotic/Thermal light} \\ g^{(2)}(0) = 1 & \text{Coherent light} \\ g^{(2)}(0) = 1 - \frac{1}{n} & \text{Squeezed light} \end{cases} \tag{2.4}$$

At zero-delay time **Light Source**

Practically, the value of $g^{(2)}(\tau)$ gives the probability to detect a second photon within the given delay time. If $g^{(2)}(0) > 1$ there is a probability to detect another photon after the first have been detected (event called as bunching). When $g^{(2)}(0) = 1$ the probability to detect a second photon is independent with the time difference to previous events and if $g^{(2)}(0) < 1$, the antibunching occurs giving the probability of detecting a second photon is less than in the case of coherent light.

The theoretical aspect of single photon source is that more than one photon cannot be generated at any given time, $n = 1$ and $g^{(2)}(0) = 0$. If the antibunching curve has no peak at zero-delay time, it means that the investigated emitter is indeed a single photon source. In practice the value of $g^{(2)}(0) = 0$ is difficult to observe due to background emission, and therefore the value $g^{(2)}(0) < 0.5$ is accepted as a single photon emission.

A single photon sources can be imagined as a two-state quantum system with a ground state and an excited state as illustrated schematically in Figure 2.9a. Upon the external excitation, from the ground to the excited state, one photon is emitted that can be detected only by one avalanche photodiode (APD). However, many quantum emitters are not just simple two-level systems and may present additional metastable levels for photons trapping and decay. In general color centers in diamond are approximated as three level systems, where an additional metastable state exists lying energetically between the ground and excited states [98-100] as shown in Figure 2.9b.

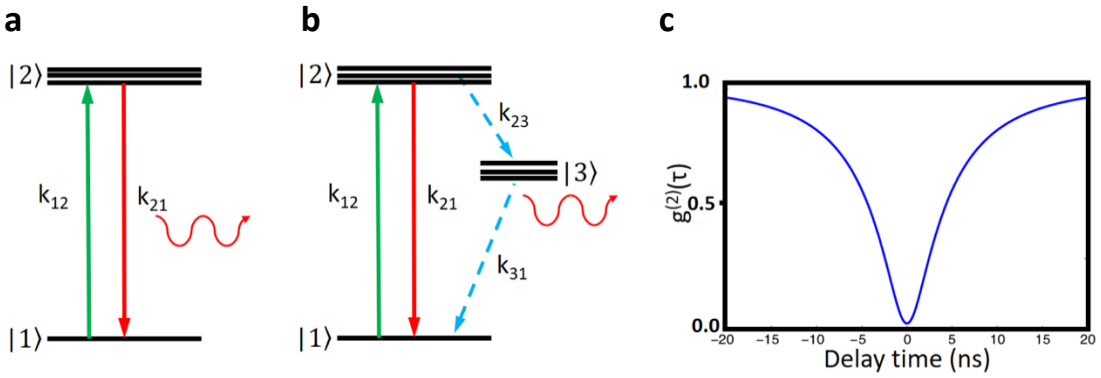

Figure 2.9. a) A schematic diagram of a two-level, b) a three-level system, k_{xy} are the transition rates from level x to level y. c) An example of a $g^{(2)}(\tau)$ function where the blue curve denotes a single photon source with $g^{(2)}(0) < 0.5$.

The Hanbury-Brown-Twiss (HBT) [101] setup (Figure 2.10.) is a standard method employed for the experimental detection of the second-order autocorrelation function $g^{(2)}(\tau)$ and consists of an HBT interferometer, a confocal microscope and

a spectrometer. When the emitter is excited by a laser (green line) it generates photons and the emission, which travels along the beam path (red line) is coupled into a fibre coupler. At this point the light can be sent to a spectrometer or go through a 50:50 beam splitter and measured by two photodetectors (APDs) as shown in Figure 2.10.

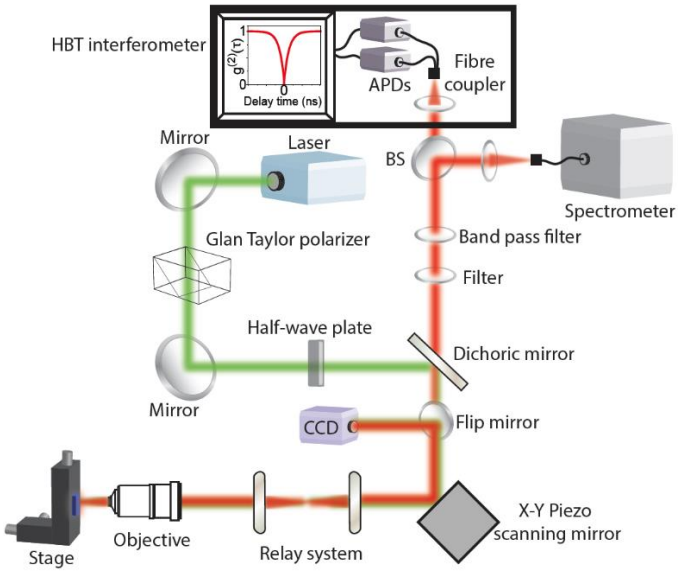

Figure 2.10. Schematic diagram of a confocal microscope with a spectrometer and HBT interferometer to measure the second order autocorrelation function.

Ensemble emission from SPE will not produce the $g^{(2)}(\tau)$ characteristic of single photon emission and the emission is directly proportional to the number of emitters forming a collective state.

2.5 Color centers in diamonds

Pure diamonds are colorless, excellent insulators and their wide transparency window, from the visible to the ultraviolet spectral range, is a consequence of their large bandgap energy of 5.5 eV. However, natural diamond can be found in a variety of different colors and the imperfections in the crystal structure are very common.

These point-defects in diamond correspond to some combination of extrinsic substitution of the native carbon atoms within the matrix or interstitial impurities, dislocations or lattice irregularities introduced during or after the diamond growth. In sufficient concentration these impurities can be visible giving colorization to diamond crystals, and therefore are named as color centers (e.g. nitrogen gives yellow to brown color, blue is attributed to boron impurity). The modifications within the crystal lattice can affect not only the diamond color, but influences other features such as electrical conductivity, creating localized, energetically separated ground and excited states within the bandgap of the diamond.

The investigation of diamond defects is of a primary importance for investigation and characterization of devices, and can be performed using optical, electrical or nuclear techniques. In general, a combination of different methods is used to properly identify the optically active emitters. The absorption spectrum is used to study the defects and to estimate their concentration, and can be detected with different spectroscopy methods including luminescence induced by light (photoluminescence PL) or electron beam (cathodoluminescence CL), electron paramagnetic resonance (EPR), and absorption of light in the infrared (IR) visible and UV parts of the spectrum. Some of the characterization methods are described in more detail in Chapter 3.

More than 150 vibrational and more than 500 electronic optical centres have been documented in natural and synthetic diamonds within the UV-IR spectral range [2, 80], but only a handful (more than 10) have been demonstrated to exist as single photon emitters (SPE) [102] operating at room temperature and producing stable emission. This is due to the high Debye temperature with low phonon-induced dephasing and phonon-assisted emission.

The simplest defects in diamond, so called intrinsic point defects, include a self-interstitial carbon, not related to an atomic site, a vacancy (an empty carbon position) and structural defects such as dislocations. Impurity-related defects consist of a foreign atom, called a substitutional impurity atom if it occupies a regular carbon position, or if it is not related to an atomic site, it is called interstitial. Figure 2.11 illustrates the intrinsic and extrinsic point defects in diamonds.

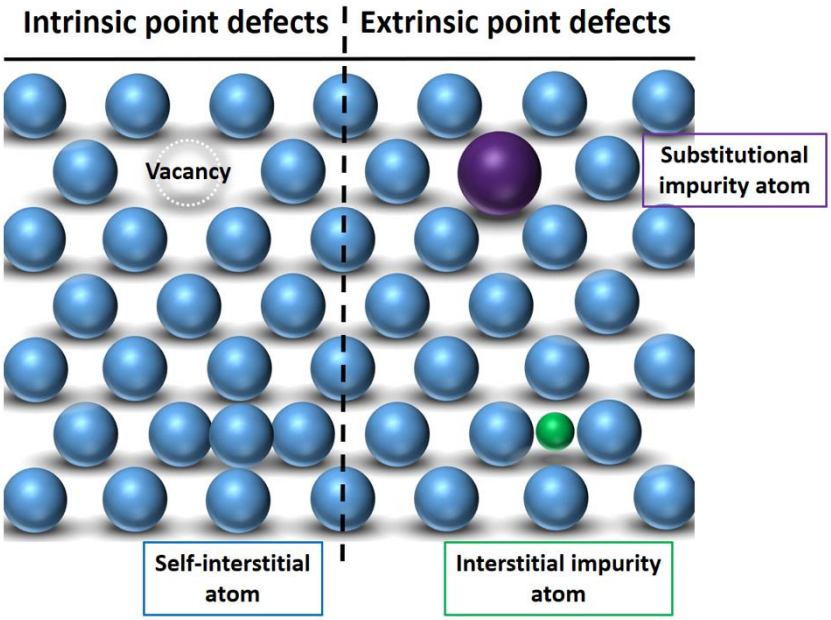

Figure 2.11. Point defects present in diamond lattice. Intrinsic point defects including a vacancy (missing carbon atom) or self-interstitial carbon. Extrinsic point defects are based on foreign atom impurity in the lattice that can occupy a substitutional or interstitial position.

Diamond lattice, because of its high rigidity, small atomic radius of carbon, short interatomic distances and strong bonds, allows the formation of only a small number of simple types of defects in nature (such as vacancies and substitutional and interstitial impurities, which represent atoms with a small atomic radius) making the doping with bigger atoms a real challenge.

Beside the compact diamond structure, another difficulty relies on the fact that when atomic radius increases the bonding energy with carbon decreases. This makes chances of capturing atoms of bigger radius very low if the traditional bottom up growth methods are considered. From the comparison of the bonding energies for different atoms such as C-C (346), C-N (305), C-Si (318), C-Ge (238), C-Sn (192) and C-H (413 kJ/mol), we can clearly see the difference and explain the low probability of capturing heavier atoms at the surface of a growing crystal in a medium containing small atoms such as hydrogen [103]. Despite the aforementioned difficulty, several heavy elements have been successfully introduced in the diamond lattice through ion implantation [104, 105]. Figure 2.12 shows a spectral map of various single photon

emitters found in diamonds [80]. The most common foreign impurities found in diamonds are nitrogen and boron. Larger impurities (such as group IV elements illustrated schematically in Figure 2.13 comparing atomic radius with that of carbon) cannot fit into the lattice without introducing a significant stress and local lattice expansion. Therefore, more complex structural deformations occur in the diamond matrix to incorporate larger elements, consisting of one or several impurity atoms (even with a relatively large atomic radius compared to carbon) and of adjacent one or more vacancies in a stable configuration.

Vacancies play a very important role in generation of the optically active emitters in diamond, and the annealing step is fundamental especially after the ion implantation, as high temperature enable the vacancies to migrate and recombine with impurity atoms leading to the stabilization and activation of optical defects.

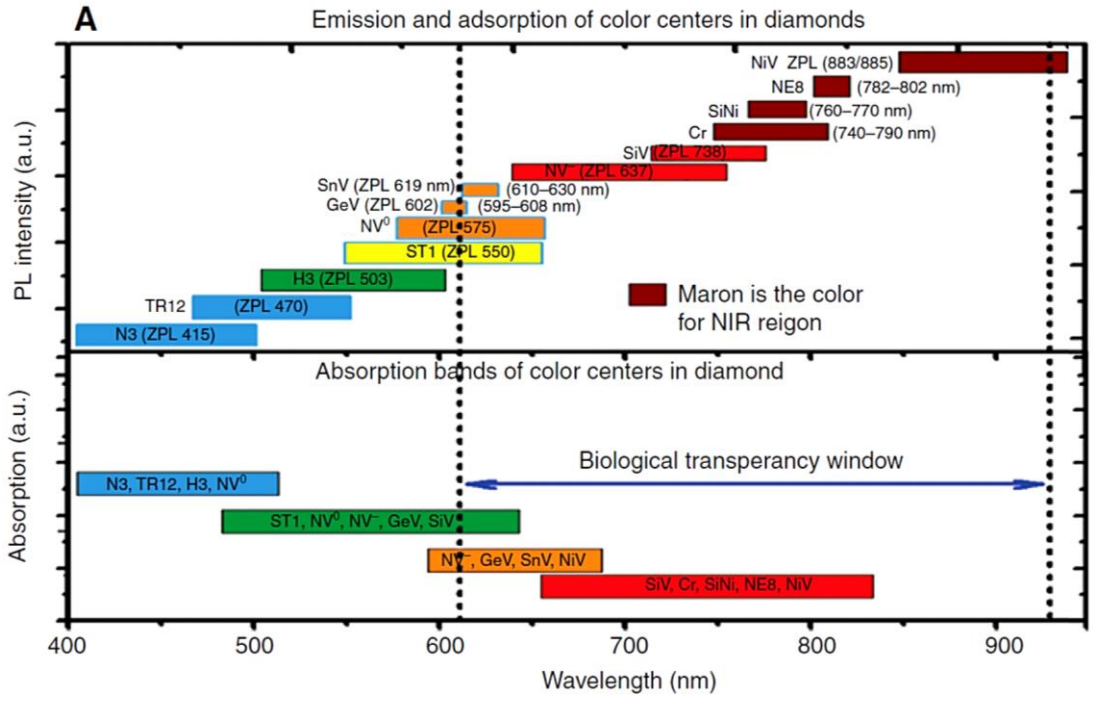

Figure 2.12. A spectral map of various single photon emitters found in diamond. The length of the bar indicates all emission for the centre, including phonon side bands. The value noted is the ZPL. The intrinsic carbon interstitials (TR12) has a ZPL of ~470 nm while the H3 consists of two nitrogen atoms with a vacancy with emission at 503 nm. An unidentified defect from the diamond, so-called ST1 centre is consists of a ZPL of ~550 nm and allows optical

manipulation of its spin. The NiSi is a nickel-silicon complex with emission 760-770 nm. While this map is not a full representation of the all discovered photon emitters in diamond, it is an indication of the variation of known centres [80].

Figure 2.13. An illustration of group IV element for visual comparison of empirical covalent atomic radii: carbon 70 pm (1 picometer = 1 x 10^{-12} m), silicon 110 pm, germanium 125 pm, tin 145 and lead 180 pm [106].

2.5.1 Nitrogen vacancy defect

Nitrogen makes up 78% of the air by volume, and as a result NV color centers are the most common and most studied defects found in diamonds [30, 88, 107]. Nitrogen may be present during the diamond growth [108] or later implanted to create NV centers [54, 57]. NV defect centres are generated upon the incorporation of a substitutional nitrogen atom with an adjacent carbon vacancy [109] in a C_{v3} configuration. Nitrogen can be present in two charge states: neutral NV^0 with zero-phonon line (ZPL) at 575 nm (with broad phonon sideband ranging from 580 nm to 650 nm) and negatively charged NV^- (or nitrogen vacancy) with ZPL at 637 nm and a phonon side band up to ~800 nm [110]. The nitrogen defect is schematically represented in Figure 2.14 with its crystallographic model, RT PL spectra and electronic structure of the negatively charged state.

Nitrogen atoms are easy to incorporate by ion implantation techniques or synthesised using CVD as they possess an atomic size comparable to carbon and can easily occupy a substitutional position. The NV^0 complex has five unpaired electrons, one from the intrinsic nitrogen atom and 4 electrons from neighbouring carbon

atoms. Since possessing five outer shell electrons, this color center is able to donate an extra electron to generate a donor energy state in the band-gap [111, 112]. Whereas NV^- (negatively charged state emitter) has six unpaired electrons, five of which neighbour the carbon atom while the intrinsic nitrogen possesses an additional unpaired electron in the defect site [113].

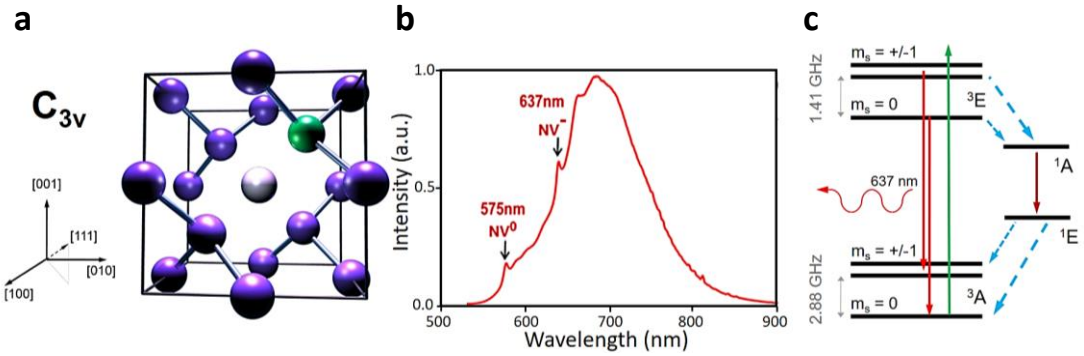

Figure 2.14. a) Crystallographic model of NV center in diamond, b) RT PL spectrum of neutral NV^0 and negatively charged NV^- nitrogen color centers. c) Electronic structure of the negatively charged NV center.

NV^- has a long electron-spin coherence time of 1.8 ms and spin dependent fluorescence. It's important to note that NV^- is the only diamond colour centre with coherent optical effects demonstrated to date which can be used in quantum optical applications [42] such as coherent population trapping [114, 115] and electromagnetically induced transparency [116, 117]. The NV centre also presents an electronic dipole moment different from zero which makes it sensitive to environmental field fluctuations. It has also been used for magnetic [36] and current sensing [118] with nanometre spatial resolution, as been proven to keep quantum information for more than 1 second [119] at RT, and has been used to establish quantum entanglement between distant electron spins [120]. Following all these successful applications, research continues in the integration of NV emitters, and the establishment of robust diamond integrated photonics platforms.

Despite the fact it possesses a high quantum efficiency estimated of ~ 0.7 (70%), NV^- color center has a weak emission into ZPL (only 4% at RT) with a large phonon side

band, which make it not an ideal candidate for quantum photonic devices which require stronger and sharper emission spectra.

2.5.2 Group IV color centers in diamonds

Group IV color centers in diamonds consist of impurities from group four of periodic table (silicon, germanium, tin and lead) that form in diamond lattice a so called split-vacancy configuration where group IV atom is placed in between two adjacent carbon vacancies in a position that would correspond to a bond-centered (BC) site in an unperturbed lattice. D_{3d} symmetry can only be realized if the impurity is in ideal BC position [121], which means exactly centered within the divacancy. Even a small concentration of such complexes allows the fabrication of optically active centers in nanodimensional diamonds, and are advantageous for a number of specific applications. D_{3d} split vacancy configuration was first proposed for silicon by Goss et al. in 1996 [56, 122, 123], by ab initio local density calculations and later by theory extended to other group IV elements. Crystallographic model of group IV emitters in diamond and room-temperature PL spectra for all group IV emitters are shown in Figure 2.15.

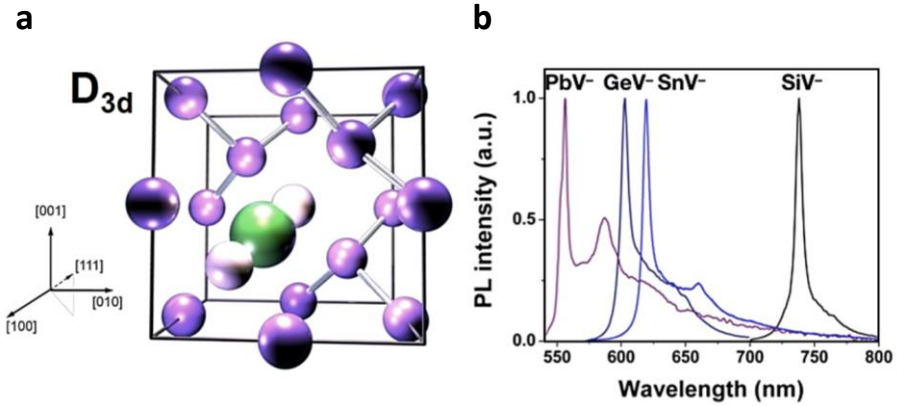

Figure 2.15. a) Crystallographic model of group IV color centers in diamond. b) A room-temperature PL spectrum for all group IV emitters [124].

The silicon vacancy defect (SiV^-) [125-129] was the first group IV emitter to be discovered in 1980s and consists in silicon atom in a diamond lattice surrounded by two vacancies in a D_{3d} configuration. Its inversion symmetry makes this SPS less susceptible to local and electric field fluctuations [130] which enable the creation of identical emitters [131, 132]. Silicon, located between two vacancies along <111> direction, possesses four outer shell electrons and may donate extra electrons to create a donor energy state in the band-gap with an overall acquisition of a negative charge. This colour centre exhibits some of very interesting proprieties such as emission in near infrared at 738 nm with narrow (only a few nm) bandwidth at room temperature with almost 70% of total emission concentrated in the ZPL, a very short lifetime (~1 ns), and full linear polarization.

Its near infrared (NIR) emission makes this color center useful for biological applications allowing the excitation of the photon by a red laser light which diminishes the cell and tissue auto-fluorescence, with many potential in-vitro, and in-vivo biological applications [133-135].

The disadvantages that limits the employment of SiV^- are its low quantum efficiency (only ~ 10%, that can be enhanced by mean of coupling), a low radiative quantum yield (~ 0.05) [136, 137], low single photon emission rates (~ few kcounts/s), and less than µs coherence times at cryogenic temperature [129, 138]. The ZPL line splits into four components at cryogenic temperatures, making the energy diagram of the SiV centre complex [126].

The research for an ideal diamond emitter continued and the discovery of another group IV color center, the germanium vacancy [139-141] GeV^- was confirmed in 2015 intensifying the effort in identifying other group IV-related defects such as tin [105, 142] (SnV) and lead [22, 143] (PbV). These color centers possess the same D_{3d} inversion symmetry configuration and similar properties offering the advantages of higher energy splitting between the ground and exited state due to a higher atomic mass. The main features of these color centers are illustrated in Table 2.4. [124].

	ZPL	FWHM	Excited state lifetime	Ground state splitting	Spin-lattice relaxation T1	Transverse relaxation time T2
SiV-	738 nm	0.7 - 5 nm	1.0 – 2.4 ns	~ 50 GHz	> 1 s at 100 mK	T2 ~13 ms at 100 mK
GeV-	602 nm	~ 5 nm	1.4 – 5.5 ns	~ 170 GHz	25 µs at 2 K	T2* ~ 20 ns
SnV-	620 nm	~ 6 nm	~ 6 ns	~ 850 GHz	~ 60 µs	Unknown
PbV-	520 nm, 552 nm	~ 7 nm	> 3 ns	5.7 THz at 520 nm 4.2 THz at 552 nm	Unknown	Unknown

Table 2.4. Group IV color centers and their photophysical properties [22, 105, 125, 139, 142-147].

GeV^- fabricated in diamond has a strong and sharp luminescence band with ZPL at ~ 602 nm, lifetime on the order of 1.4 – 5.5 ns, and can be used as a SPS at room temperature. Also GeV and SnV possess larger energy band gap compared to silicon which reduces the phonon split mixing and increases the spin coherence time. The SnV colour centre exhibits a strong and sharp ZPL at ~ 620 nm with a full width at half maximum (FWHM) of ∼6.2 nm along with a phonon sideband (PSB). The emitters possess a short excited state lifetime of ~ 6ns, and provide another option in the visible range with several interesting properties for the fabrication of quantum devices. The generation of these color centers can be accomplished by their incorporation during the growth process or more commonly by ion implantation. The incorporation of GeV^- centres in diamond has been successfully accomplished during HPHT and CVD synthesis [140, 148-150] utilizing suitable precursors while fabrication of SnV^- has been done via HPHT synthesis and ion implantation [95, 103]. The preferable way to fabricate these emitters would be during synthesis, as ion implantation, as explained previously, introduces damage in the diamond lattice which degraded the photo-physical properties.

The lead-related vacancy to date has been only successfully fabricated by ion implantation due to the difficulty to incorporate such a large atom (Pb atomic radius = 180 pm) within the highly compacted diamond lattice [22, 143]. It has a two ZPL lines at ~ 520 and 552 nm. The emission is sharp with FWHM of ~ 7 nm and it displays an excited state lifetime of ~3 ns. Figure 2.16a shows energy structure of group IV color centers without and with the application of external magnetic field B, while figure 2.16b illustrates the predicted energies of ground and excited states for all group IV emitters.

The formation and activation of optically active defects after the implantation occurs via high temperature annealing (800 - 1200°C) that lead to the migration of vacancies forming vacancy-ion complexes. The formation yields are substantially low for all the group elements (except for Si that can be incorporated easily with ~ 25% yields) with 4% for Ge [151], 5% for Sn [105] and 2% for Pb [143] in the range of 15 – 50 keV of implantation energies.

Despite being only recently discovered, the group IV color centers have been already employed in a multitude of devices and applications. Spin manipulation with microwave fields has been proven for SiV^- and GeV^- [147], and other group IV defects may be less susceptible to dephasing due to the larger intrinsic orbital splitting, making promising candidates for quantum networks.

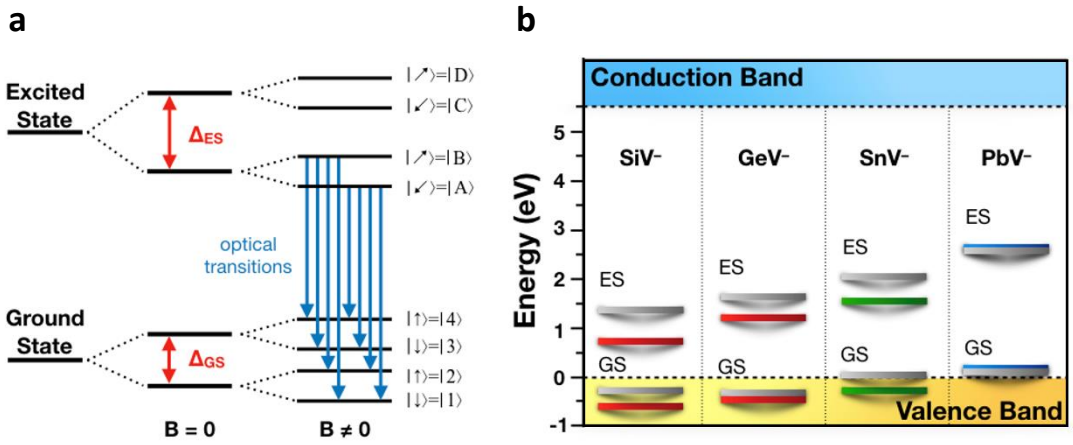

Figure 2.16. a) Energy structure of group IV color centers without and with the application of external magnetic field B. b) Predicted energies of the ground and excited states for all group IV emitters.

Group IV emitters all demonstrate a strong emission into the ZPL, low spectral diffusion, and their optical transitions are protected by their split-vacancy configuration which make them suitable candidates for integrated nanophotonic devices [152-157]. Their optical properties, such as the robust and stable emission, high photon coherence, high emission efficiency, and small inhomogeneous spectral distribution are all crucial aspects for solid state quantum applications [158]. Other configurations for integration into photonic devices have been explored, such as fibre-based microcavities [159, 160], microdisks resonators [161] and nanopillars [20-22]. The group IV emitters have also been employed in temperature sensing [63, 162-164] and as biomarkers given they are non-toxic, nanosized, and easily functionalized to a specific target. There are many other potential applications to explore which can employ group IV defects in diamond and this work offers a new way to engineer high these emitters in high quality diamond membranes and NDs by MPCVD, expanding and simplifying available methods.

Chapter 3 Fabrication and characterization methods

This chapter provides details about the fabrication techniques of nanoscale diamond membranes and NDs, including the equipment and setup description. The fabrication requires a combination of two main processes involving the use of microwave plasma chemical vapor deposition and inductively coupled plasma reactive ion etching (ICP-RIE).

High quality thin diamond membranes which can host bright, photo-stable, and RT optically active emitters, as described in the previous chapter, are necessary for a variety of advanced nanophotonics, nanoelectronics, and optomechanics applications. The thickness of the fabricated single crystal diamond membranes is of a high importance for the light confinement. The thickness of the membranes is suitable for the realization of nanodevices to satisfy the single mode condition in the vertical direction, necessary in cavity fabrication, and for the group IV emitters this should be of the order of ~200 - 300 nm [165]. The required thickness is determined by ratio between the operational vacuum wavelength and the refractive index of the diamond (n = 2.4). For a SiV centre, with a ZPL of 737 nm, and refractive index of diamond as 2.4, the required thickness is ~300 nm.

The first important step consisted in generation of nanoscale SCD membranes since the sub-micron thick membranes are not yet commercially available. So far different approaches to realize free-standing diamond membranes have been employed such as focused ion beam (FIB) milling to etch suspended diamond membranes or high energy and high dose ion implantation (MeV, 10^{17} ions/cm^2) to create a subsurface damaged layer followed by the annealing and lift-off. Both these techniques unfortunately degrade the photo-physical proprieties of corresponding color centers, damaging the created membranes by introduction of a built-in-strain field which causes bowing and bending of the membranes. To overcome these problems and improve the membranes' quality several further processes are necessary, such as

MPCVD homoepitaxial overgrowth, flipping and successive uniform removal of damaged material trough ICP-RIE etching [16, 32, 166].

To make diamond membranes suitable for fabrication of devices, the improvement of their optical proprieties is necessary. The CVD homoepitaxial overgrowth of diamond membranes generates a new pristine layer with features comparable to bulk diamond [166], but with superior physical, optical, and spin proprieties.

In this project a bulk single crystal diamond (IIa type electronic grade from Element 6) was overgrown by MPCVD and subsequently implanted with high dose of high energy He^+ ions (5 x 10^{16} ions/cm^2, 1 MeV). This process creates a thin amorphous layer ~1.7 µm beneath the surface of the diamond (calculated with Stopping and Range of Ions in Matter SRIM simulations [167]) and is followed by thermal annealing in high vacuum at 900°C for 1 hour to convert the implanted diamond sub-surface to a graphite-like amorphous carbon layer that can be successively etched. The electrochemical etching is used to selectively remove the damaged layer and was performed using two tungsten probe tips immersed in MilliQ water. The positively biased tip was in contact with the damaged surface and the negatively biased tip was positioned slightly above the diamond substrate. The constant voltage of 60 V was applied for one month (up to three months) for the lift-off resulting in floating diamond membranes. The membrane fabrication process from bulk SCD crystal is schematically shown in Figure 3.1.

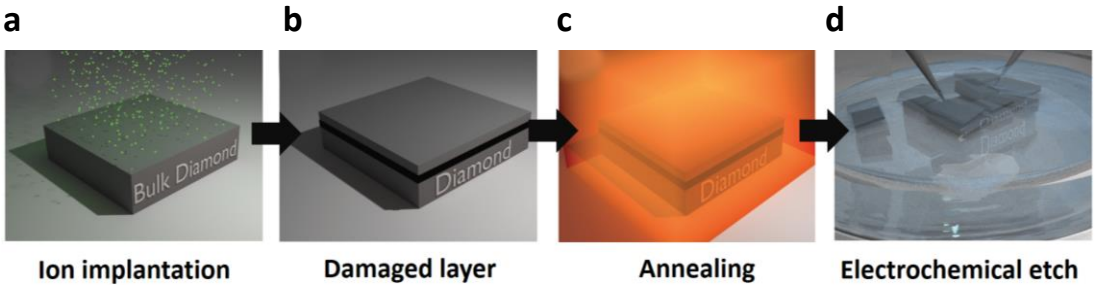

Figure 3.1. A schematic illustration that shows the main processes in diamond membrane fabrication: a) a high dose and high energy He^+ ions implantation (5 x 10^{16} ions/cm^2, 1 MeV) of the bulk diamond that creates the damaged layer 1.7 µm beneath the diamond surface

shown in b). c) A high temperature vacuum annealing (at 900°C for 1 hour). d) Electrochemical etching to detach the formed membranes from the bulk diamond [168].

At this point the membranes can be transferred onto a sapphire substrate with the damaged layer on the bottom using a titanium probe or by mean of a droplet of MilliQ water. The experimental setup for diamond electrochemical etching to detach diamond membranes from the bulk is shown in Figure 3.2.

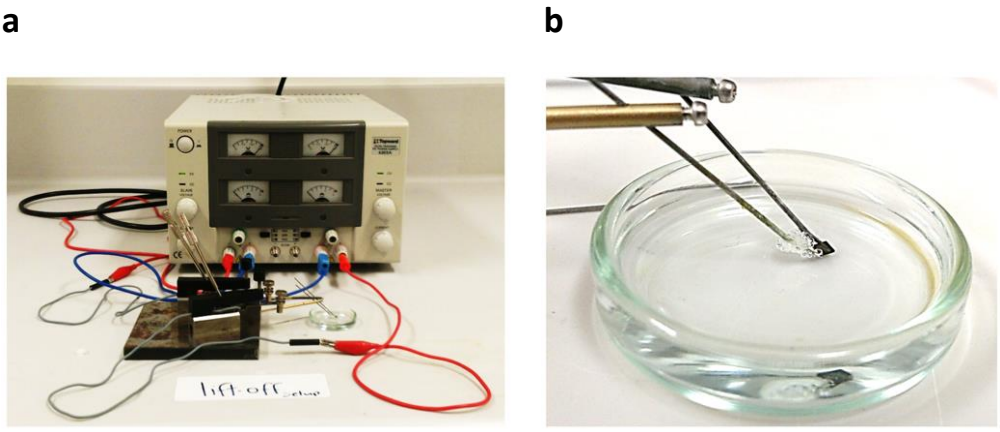

Figure 3.2. a) Photo of the experimental setup employed for the liftoff. The electro- chemical etching was carried out using a constant forward bias of 60 V. b) Zoom image of the probes. During the etching, a positively biased tip in the contact with the top surface of the diamond while the negatively biased tip positioned above in close proximity.

3.1 Microwave Plasma Chemical Vapor Deposition

MPCVD is a chemical vapor deposition method that uses microwave induced plasma (a partially ionised gas) to grow high quality diamond. During the synthesis, the diamond substrate is exposed to volatile precursors and growth proceeds by the pyrolization of carbon containing gases such as methane, carbon monoxide, or others. The typical precursor is a mixture of gases methane and hydrogen. A picture of the experimental reactor used in the experiments as well as a schematic illustration of MPCVD chamber are shown in Figure 3.3.

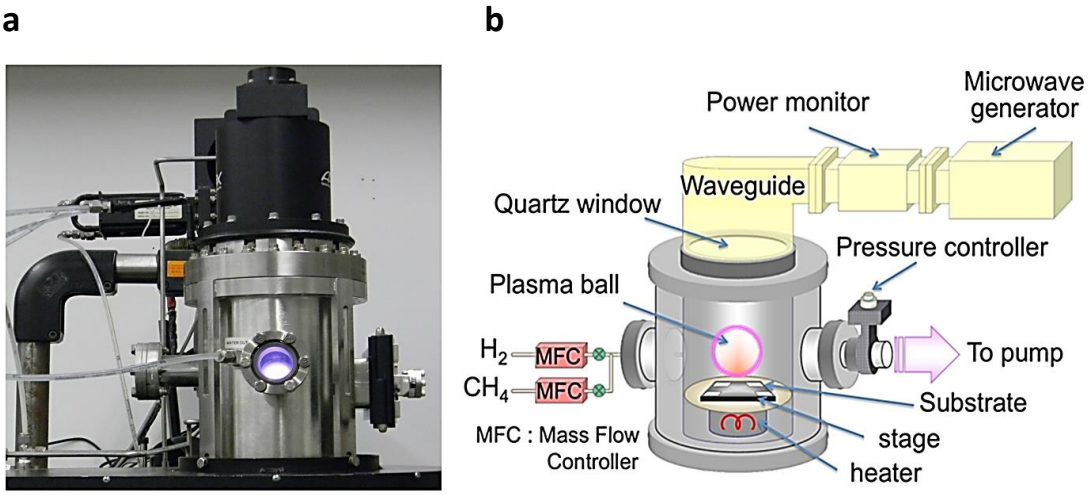

Figure 3.3. a) MPCVD experimental setup ASTeX. b) Schematic of the CVD system [169].

The system available in our laboratory is a MPCVD ASTeX (Applied Science and Technology, Inc.) reactor that is commonly used for high quality diamond growth (type IIa or better). Its main components consist of a deposition chamber, gas supply with pressure and mass flow controllers, vacuum and exhaustion lines, a heating/cooling system, and power energy supply.

The gas supply line, consisting of cylinders of various reactant gases (such as hydrogen, methane, and argon in our case), stainless pipelines, digital mass flow controllers, and several valves. This system provides gases necessary for the chemical reaction at an established flow rate in order to achieve desired composition of reactants at desired flow and pressure. As mentioned previously, methane is the main carbon source while hydrogen is the plasma precursor. Sometimes argon can be added to adjust the pressure in the chamber. Nitrogen was often unintentionally present as impurity in our samples after a MPCVD overgrowth since the gas used for venting was nitrogen. To obviate this problem a new line was added supplying argon to vent the chamber. Several mass flow controllers (MFC) regulate the gas flow rate supplied during the growth in a unit of sccm (standard cubic centimeters per minute).

The part of the MPCVD system, that distinguishes it from other CVD systems, is the energy supply, mainly an RF generator necessary to produce plasma (a highly ionized

gas or a mixture of several gases composed of ions, electrons and neutral particles) by microwave radiation.

The S-1500 series ASTeX system employed can deliver up to maximum of 1.5 kW CW of 2.45 GHz of MW power coupled from a waveguide (which is normally a rectangular pipe made of metals or dielectric materials that functions as a transportation tunnel) into the cavity, regulated to 0.5% of output power with less than 1% ripple. A triple-stub impedance helps tuning the source to the cylindrical cavity and to confine the plasma to the region just above the substrate mounted on a variable-height stage. A quartz plate on top of the chamber forms a window for the MW and provides a vacuum seal to the chamber.

The plasma ball is created by microwave discharge above the substrate sitting on a carbon puck (sample holder) which can act as an additional source of carbon and is necessary to confine the plasma. The plasma generates the heat and a typical MPCVD requires temperatures between 800 - 1100°C for a high quality diamond growth. However, the plasma coupled with high MW energy, becomes spatially inhomogeneous and the core of the plasma is at a much higher temperature compared to the surrounding region. The temperature drastically decreases moving from the center to the edge of the plasma, therefore the sample to overgrow needs to be carefully positioned in the center of the carbon puck, and exactly in the middle of the chamber otherwise the shape of the plasma can be distorted influencing the temperature gradient on the carbon puck and the quality of the growth (Figure 3.4.).

The temperature of the sample can also be controlled and stabilized by an additional heater. The variable-height stage is made of graphite, a material with high thermal conductivity, high thermal stability, and exceptional chemical and mechanical resistance. A thermocouple is fixed on the bottom of the stage to monitor the substrate temperature during the growth. In our case the temperature in the CVD chamber is determined solely by the plasma density since no heating stage has been used during the overgrowth process. To avoid overheating, the chamber is cooled down by water that runs through pipelines wound inside the stainless steel wall of the CVD chamber.

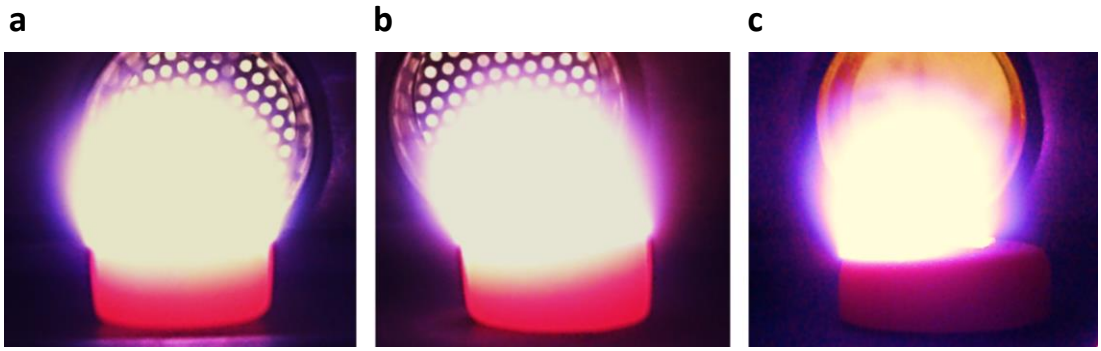

Figure 3.4. Picture of the puck with plasma ball during the overgrowth: a) symmetrical, centered on the substrate b) slightly moved on the side c) covering only part of the puck with sample partially uncovered underlying the importance of correct positioning of the puck inside the chamber.

Our lab utilizes centralized tap water cooling system which is sufficient also for the CVD because of its relatively low working temperatures and low power of the microwave generator. The growth process is controlled and run by a PC Labview interface, enabling simple, reliable, and safe operation of the system and the software interface for MPCVD ASTeX reactor is shown in Figure 3.5.

In the plasma, complex reactions occur, including chemical reactions, adsorption, diffusion, or desorption resulting in a thin film formation on the substrate surface. The composition and structure of the deposited diamond film depend on many parameters involved in the process, such as substrate temperature, pressure, plasma power, gas composition, gas flow rate, the substrate position within the chamber, as well as puck size and chamber geometry.

The use of MPCVD system presents many advantages such as good control over the crystal quality (especially SCD, type IIa diamond or better), single crystal diamond synthesis process with a high MW power coupling efficiency, a flexible design enabling improvements in plasma homogeneity, higher growth rate (> tens of microns per hour), and large area deposition (few to hundreds of mm).

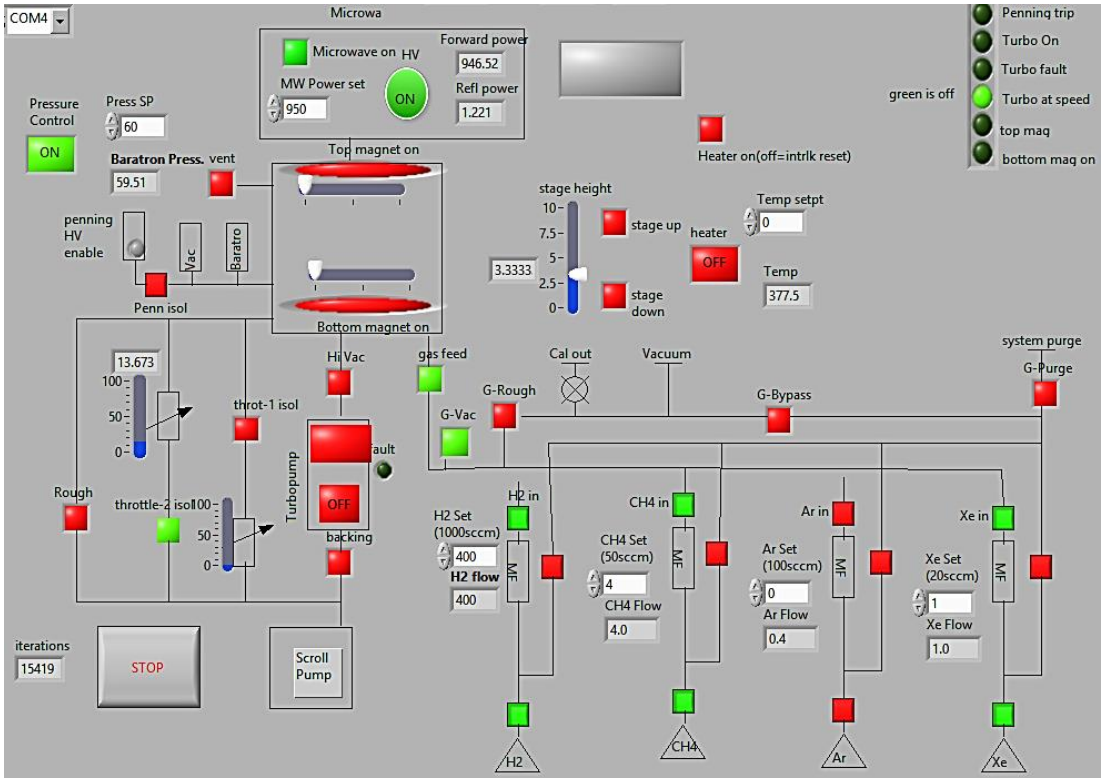

Figure 3.5. LabView software interface for MPCVD ASTeX reactor.

3.1.1 Surface chemistry during the diamond growth by MPCVD

Diamond, at the temperatures and pressures commonly used in diamond CVD growth, is in a metastable region. These nonequilibrium conditions make it thermodynamically unstable and graphite with its sp^2 bonds is a more stable phase of carbon under normal conditions. The surface chemistry during the diamond growth is a complex process involving several reactions and has been the subject of investigation since the 1950's. In the initial studies, a graphitic component was simultaneously formed along with the diamond phase. Therefore, suppressing the deposition of graphite through preferential etching by atomic hydrogen was necessary to improve the diamond quality and successive experiments were performed in hydrogen-rich atmosphere. These complicated processes have been simulated since the 1990's thanks to the development of modelling software and computational chemistry [170-173].

As previously mentioned, the common gas used in CVD growth of diamond is a mixture of hydrogen and methane and their radicals generated by MW discharge [174, 175], which generate the high temperature necessary for thermal dissociation of H_2 into atomic hydrogen (hydrogen radicals generated by electron impact in plasma), a process which is necessary to trigger the growth process. Hydrogen prevents the reconstruction of graphitic sp^2 bonds by selectively etching graphite from the growing surface and increasing the diamond growth rate.

The major reactants in MPCVD process are atomic and molecular hydrogen and hydrogenated carbon radicals, and the complex process can be simplified into several central chemical reactions [170-173, 176-181] as follow: abstraction and adsorption of hydrogen atoms, adsorption of hydrocarbon radicals followed by growth paths such as thermal desorption and species integration. MW energy discharge into the plasma promotes hydrogen dissociation and the electron dissociation process is dominant at lower pressures and temperatures (few tens of Torr) producing hydrogen radicals via:

$$H_2 + e^- \rightarrow 2H + e^- \tag{3.1}$$

Therefore, hydrogen is important to both initiate the growth, and to terminate the substrate surface, promoting the growth of diamond while suppressing graphite formation. A schematic growth process is illustrated in Figure 3.6.

As a source of carbon we use methane which can form activated species through the abstraction of hydrogen (CH_x with x = 1, 2, 3) following the reaction:

$$H + CH_4 \rightarrow CH_3 + H_2 \tag{3.2}$$

Then the carbon containing activated spices such as C_2H_y (where y = 0, 1, 2, 3, 4, 5, 6) are formed by recombination of methyl radicals:

$$CH_3 + CH_3 + M \rightarrow C_2H_6 + M \tag{3.3}$$

$$C_2H_y + H + M \leftrightarrow C_2H_{y-1} + H_2 + M, \tag{3.4}$$

where M represents heavier molecules and CH_x and C_2H_y act as precursors for diamond growth during the MPCVD process. The surface of diamond is bombarded

with hydrogen radicals and when the whole surface is hydrogen terminated, it cannot react further with carbon precursors thus the abstraction of hydrogen atoms from the surface by hydrogen radicals takes place forming active sites to initialize the growth of diamond layer following the reaction:

(hydrogen abstraction) $$C_dH + H \rightarrow C_d^* + H_2 \quad (3.5)$$

where C_dH is a hydrogenated site on the diamond surface while C_d^* is a radical site with removed hydrogen.

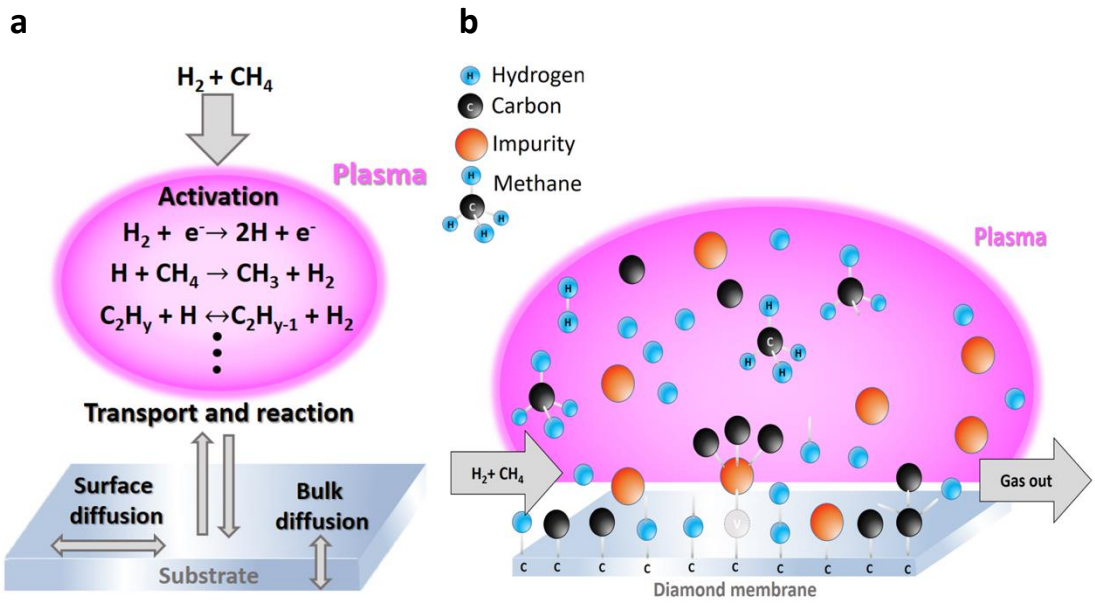

Figure 3.6. a) Schematic processes and chemical reactions involved in the diamond growth. b) Chemical reactions involved during the MPCVD diamond process. The radicals are formed by gas ionization and transported to the surface to generate a pristine diamond layer.

The actual diamond growth is based on the careful balance between the abstraction, adsorption, anisotropic etching, and chemisorption of carbon precursors. The atomic hydrogen etches graphite much faster than diamond and the etching rates depend on the structure of the diamond surface and crystal orientation. The fastest etching rate is for trihydride radicals (CH_3) followed by dihydride (CH_2) and monohydide (CH) [182].

(hydrogen adsorption) $$C_d^* + H \rightarrow C_d H. \quad (3.6)$$

Chemisorption is the reaction that occurs at active sites (not on hydrogen terminated but on hydrogen abstracted sites) and the structure chemisorbed is a trihydride (CH_3), which is then etched by hydrogen radicals:

(CH_3 chemisorption) $$C_d^* + CH_3 \rightarrow C_d CH_3 \quad (3.7)$$

With the continuous process of hydrogen absorption and abstraction the diamond growth takes place forming a new pristine diamond layer. Under the constant conditions the growth rate is directly proportional to the concentrations of the hydrocarbon radicals [CH_3] and hydrogen [H], and can be calculated for different crystal orientation at fixed temperature with different reaction rate constants [170].

The best quality, smoothest, and lowest defect densities during diamond growth were grown on the (100) surface orientation in comparison to other substrates crystallographic orientation such as (111) or (110) [183-185].

This whole process is based on surface reactions and kinetics of the vapor phase components, and not by thermodynamic considerations. The research continues to further understand both vapor-phase and surface chemistry as the exact growth mechanism remains unclear due to the challenges associated with in-situ observations [186].

For any reactor design, the growth rates and quality of SCD or nanodiamonds dependents on several factors such as: pressure, MW power, [H_2]/[CH_4] ratio in the total gas flow, substrate holder design, temperature distribution, electric field intensity, and absorbed microwave power density over the substrate holder.

To obtain homoepitaxial SCD growth, the typical temperature in MPCVD chamber is between 700 - 1200 °C, where in this range diamond growth is controlled by chemical kinetics rather than by surface diffusion processes. Previous work has shown that the growth rate below 1000 °C obeys an Arrhenius relation [185, 187, 188]. Below 700 °C the growth is slow [189], resulting in highly rough or non-epitaxial diamond formation. Only

for a small range of growth parameters it is possible to obtain a high quality homoepitaxial diamonds.

The growth parameters optimized for our ASTeX reactor are employed to overgrow thin diamond membranes or nanodiamonds are: 900 W of MW power at 60-70 Torr with the hydrogen/methane ratio = 100 (400 sccm of H_2 and 4 sccm CH_4) with the temperature requested between 800 – 1100°C. The growth time may vary according to the desired thickness of the membrane or nanodiamond size required for the specific application. In general, our samples were grown between 8 and 15 minutes.

NV^- color center was initially present as undesirable contaminant in our samples after MPCVD overgrowth since the nitrogen was used as a venting gas in our setup. To overcome this issue a new line has been added supplying argon to vent the chamber and grow high purity diamonds suitable for incorporation of other color centers such as group IV defects and despite no intentional introduction of silicon during the growth in the CVD chamber, silicon was present in small amounts in almost all our samples due to the quartz windows as the contaminant components of the reactor.

3.2 Inductively Coupled Plasma Reactive Ion Etching

Reactive ion Etching (RIE) is a vapor phase dry etching process, where the sample is physically bombarded by ions and/or chemically by reactions through reactive species at the surface, providing an overall even and highly directional etching. There are several dry etching systems that vary in their selectivity and etching mechanism, for example physical or chemical, anisotropic or isotropic. The selectivity towards different materials is achieved by using different gas mixtures. These gases can be fluorinated, chlorinated, or involve compounds in combination with oxygen and argon.

RIE uses chemically reactive plasma generated by a radio frequency (typically 13.56 MHz) to remove material from the surface. The power of hundreds of volts along

with the oscillation of the electric field strips the electrons from the gas molecules, forming a plasma phase.

In this work the reactive ion etching (RIE) has been used to etch the diamond membranes and to clean their surface with oxygen plasma at every step of fabrication.

The physical etching of the RIE is provided by the bombardment of the surface with argon ions, damaging the unreactive substrate, while the chemical etching can be achieved by the introduction of chlorinated and fluorinated species such as CF_4 or SF_6. A schematic diagram of the RIE process and a picture of the ICP-RIE Trion system employed in these experiments are shown in Figure 3.7.

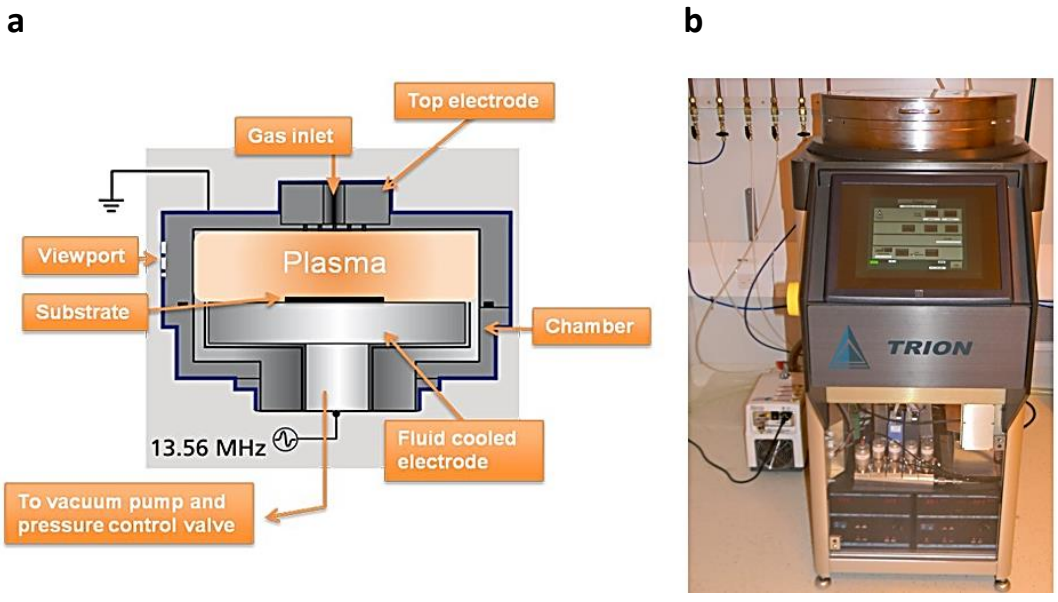

Figure 3.7. a) Diagram of Reactive Ion Etching System (Oxford Instruments). b) ICP-RIE system used for etching and cleaning of the diamond surface.

Usually, the membranes require a cleaning step to remove any kind of impurities that can act as a hard mask during the thinning process. To clean the membrane surface the O_2 plasma cleaning step with ICP-RIE is performed first.

The conditions are:

- O_2 plasma cleaning (45 mTorr, ICP 200, RIE 0, O_2 35 sccm, 30 min)
- SF_6 etching (45 mTorr, ICP 500, RIE 100, Ar 10 sccm, O_2 15 sccm, SF_6 5 sccm, 18 min)
- O_2 plasma cleaning 10 min

The SF_6 etching time may vary and depends on the targeted final thickness of the membranes. Before and after the etching step the thickness of the membranes is measured by analysis with the Scanning Electron Microscope (SEM). The thickness of the membranes is critical to control for the subsequent fabrication of optical waveguides and cavities, needing to be between the operational vacuum wavelength and the refractive index of the diamond [60,61]. Figure 3.8. shows the SEM images of the diamond membrane as transferred, after 10 minutes CVD overgrowth (thickness ~ 2.7 µm) and after RIE etching to thin the membrane (~ 300 nm).

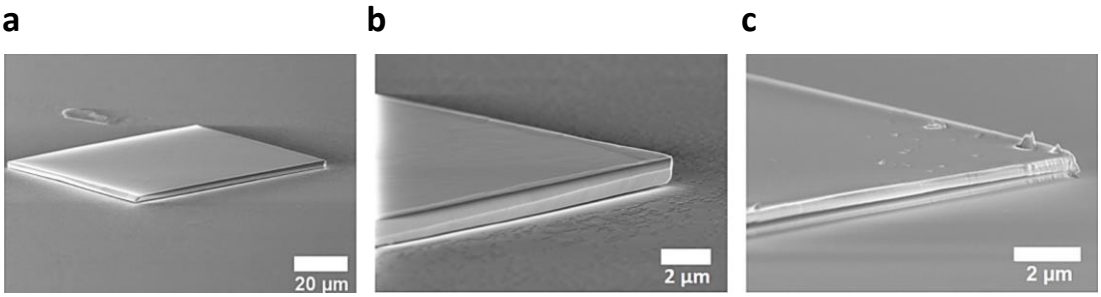

Figure 3.8. SEM images of the diamond membrane at different steps of the fabrication process: a) as transferred, b) after 10 minutes of MPCVD overgrowth and c) after flipping and etching step (~ 300 nm thick).

The required thickness of the membranes suitable for the realization of nanodevices in cases of SiV^-, GeV^- and SnV is around 300 nm to satisfy the single mode condition in the vertical direction necessary in cavity fabrication for our projects. Usually, to obtain the thickness of 300 nm, ~ 18 minutes of ICP-RIE etching is required.

3.3 Devices patterning and fabrication

3.3.1 Electron Beam Lithography

Electron Beam Lithography (EBL) is a lithography technique that allows patterning with resolutions down to ~10 nm, utilizing the scanning electron beam to expose a resist. In this work EBL was performed on the Zeiss Supra 55VP SEM (described in detail in § 3.5) using a Hydrogen Silsesquioxane (HSQ) thin layer, which acts as a negative resist. It is an inorganic compound recently used in EBL for high resolution patterns (achievable resolution ~ 10 nm). HSQ selectively forms silicon dioxide only in the areas of electron beam exposure and after development in an NaOH/NaCl (1%/4%) solution.

On the SCD membrane, thinned to ~300 nm, a layer of HSQ resist was spincoated onto the sample. The thickness of the resist plays an important role in the resulting resolution of the patterning. In our case after a spincoating at 6000 rpm (rotations per minute) for 1 minute the thickness of HSQ obtained was around 100 nm. To remove the excess solvent a pre-baking step is performed on a hot plate at 90°C for 4 minutes directly before placing it in vacuum to prepare the HSQ surface for e-beam exposure. The dosage required is calculated as a function of beam current and beam speed, and then translated to the programmed patterns on the substrate. In general, high energy (20 keV) and high dosage (1500 $\mu C/cm^2$) electron beam exposure is necessary for HSQ patterning. The beam pattern is programmed and driven using the Elphy+ software. Many different devices were successfully patterned with this technique and are described in more detail in the following experimental sections. The development of HSQ is performed by immersion in an aqueous solution containing 1% of NaOH and 4% of NaCl for 4 minutes, and followed by rinsing with MilliQ water to remove the traces of developer and resist, leaving behind the desired structure. The structure is subsequently etched into the diamond membrane by ICP-RIE. The etching receipt for microdevices consists in ICP-RIE O_2 plasma cut with

following conditions: 10 mTorr, ICP 500, RIE 100, Ar 5 sccm, O_2 45 sccm. The hard mask can then be removed by ICP-RIE following the recipe: 100% SF_6 etch at 35 mTorr for 2 minutes to remove 100 nm of silicon dioxide layer without damaging the diamond layer.

In the following section, I discuss the methods employed to investigate the emission from color centers in diamond, the quality of the growth, as well as thickness and surface roughness of the grown diamond membranes.

3.4 Confocal Microscope Spectroscopy

In 1955 the first basic concept of confocal microscopy was developed by Marvin Minsky consisting in the light collection from one point while rejecting the background light from any other points in the imaging plane (considered as a noise) by introduction of a spatial pinhole. The light is then focus through a small aperture which blocks out-of-focus light in image formation considerably improving the contrast and resolution of images. Confocal microscopy is based on the same components as a normal optical microscope, with the difference that in conventional microscope the light travels through the sample as far as it can penetrate and the confocal microscopy only focuses on a small beam of light that can pass through a pin hole with a narrow depth level at a time. From the 2D images acquired and different depths a 3D images can be reconstructed.

The base components for optical microscopy are the source of light, the objective lens and components to collect the observed emission. A detector to collect the light is used in the characterization of low intensity emissions such as single photon emissions from diamond defects. The resolution limit is defined as the minimum distances by which two structures can be separated but still appearing distinct. This limit is empirically described by Abbe's equation, and depends on the wavelength of

the light source, where in the case when the resolution exceeds this limit, the images blurs.

In reality a point of light cannot be considered a perfect dot due to the diffraction and interference phenomena, appearing instead as a disk with concentric circles with diminishing intensity called an airy disk.

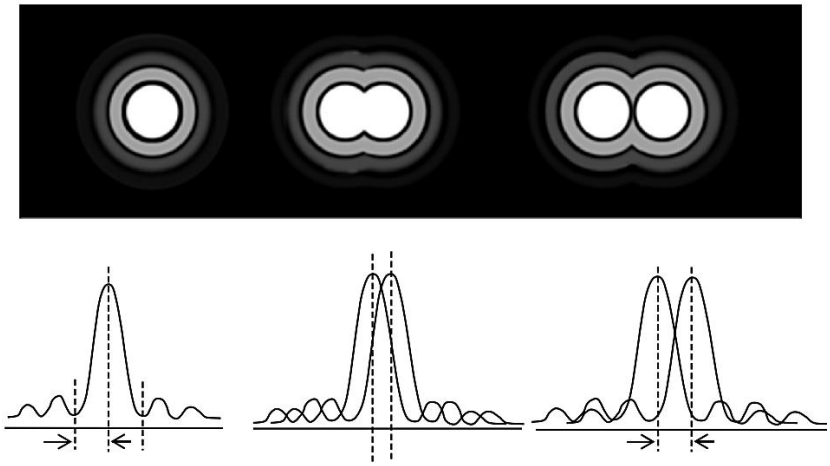

Figure 3.9. Illustration of resolution limit with airy disk and corresponding wave front [190]

Two objects can be distinguished from each other if the center of two primary peaks (containing ~ 84% of the light) are separated by a distance which is equal to the radius of Airy disk and is given by Abby's equation [191]:

$$d = \frac{0.612 * \lambda}{n * \sin(\alpha)} \tag{3.8}$$

where d = resolution, λ = wavelength of imaging light, n = refractive index of material relative to free space with α = half aperture angle in radians (corresponding to the half of the angle of the cone of light from specimen plane accepted by the objective). The main property of the objective, that focuses and collects the light from the sample under investigation, is the Numerical Aperture (NA) that determines the efficiency in collecting the photons. The NA is given by:

$$NA = n * \sin(\alpha) \tag{3.9}$$

where the NA is directly proportional to the collection efficiency.

To investigate the characteristics of the fabricated emitters in diamond, photoluminescence measurements (PL) at room temperature were performed using a standard scanning confocal microscope. To excite the sample a continuous 532 nm laser (Gem 532, Laser Quantuum) was used focusing on the sample trough a high numerical aperture objective (NA = 0.7 or 0.9). A 532 nm dichroic mirror (532 nm laser BrightLine, Semrock) was employed along with a long-pass filter (Semrock) to collect the light followed by a graded index fibre onto a spectrometer (Princeton Instruments).

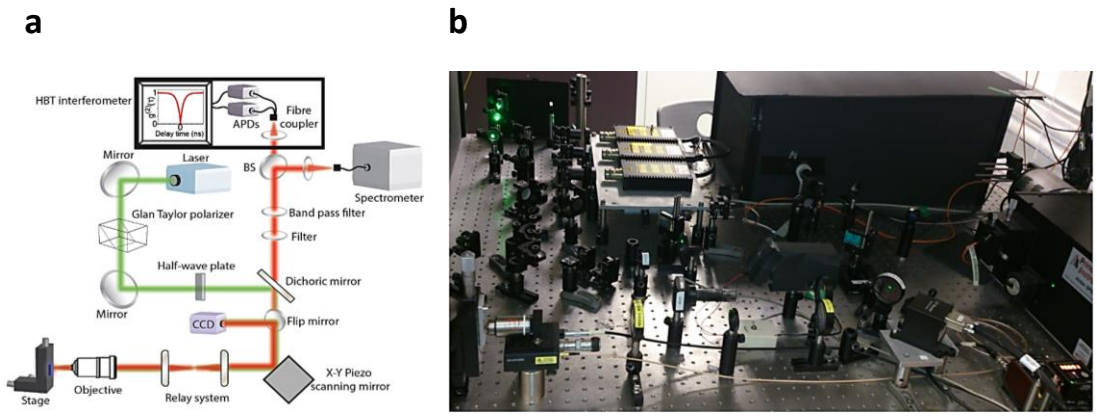

Figure 3.10. a) Schematic diagram of the scanning confocal microscope. b) Picture of the confocal setup employed in the experiments.

3.5 Scanning Electron Microscopy

Electron microscopes are versatile instruments that employ a highly focused electron beam for imaging instead of light to achieve much higher resolution images beyond the diffraction limit of light due to the shorter wavelength of the electrons. Different signals are generated between the interaction of electrons and matter giving rise to several phenomena and different types of emissions, such as secondary electrons, backscattered electrons, Auger electrons, and X-ray emissions, each of which carry useful information about the sample and can provide a wide range of information

according to the user's needs. The scanning electron microscope (SEM) [190, 192] permits the identification of a structural, morphological and elemental composition of the material using an electron beam (typically 1 nm to 10 nm in width and with an energy of 0.1 – 30 keV) generated by an electron gun. This system requires a high vacuum (~ 10^{-6} – 10^{-7} Torr) in order to prevent beam interactions with residual gas molecules in the chamber and allows image resolution down to a nanometer scale. In the case of SEM, two types of electrons are typically detected: secondary electrons (SEs) and backscattered electrons (BSEs). Secondary electrons originate from the surface or the near-surface regions of the sample and are a result of inelastic interactions between the primary electron beam and the sample. They possess lower energy than the backscattered electrons and are very useful for the inspection of the topography and provide more detailed information about the surface of the sample. A schematic illustration of signals generated in SEM by electron beam-sample interactions, and the regions from which the different signals can be detected is shown in Figure 3.11a.

The Everhart-Thornley detector is the most frequently used device for the detection of SEs, and consists of a scintillator inside a Faraday cage, which is positively charged and attracts the SEs. The scintillator is used to accelerate the electrons and convert them into light before reaching a photomultiplier for amplification. To increase the efficiency of detecting secondary electrons the SE detector is usually placed at the side of the chamber and at an angle to the sample.

Backscattered electrons come from deeper regions of the sample and are reflected back after elastic interactions between the beam and the sample. They originate from a broad region within the interaction volume as a result of elastic collisions of electrons with atoms, which change in the electrons' trajectories. The number of the backscattered electrons reaching the detector is proportional to their atomic number providing images that carries information on the sample's composition. BSE images can also provide valuable information on crystallography, topography, and the magnetic field of the sample.

Typically the preparation of an SEM samples does not involve too sophisticated a procedure, however, when sample is an insulator like diamond then imaging becomes more challenging due to electrostatic charging. In this case, a conductive piece of

copper tape is often placed under the sample, or the sample can be coated with a thin film of conductive layer (usually gold or carbon), or the sample can be investigated using a low voltage electron beam. Usually, lower voltages use secondary and backscattered electron regimes and enable the imaging of fine scale morphological features of the sample with low penetration depth into the material.

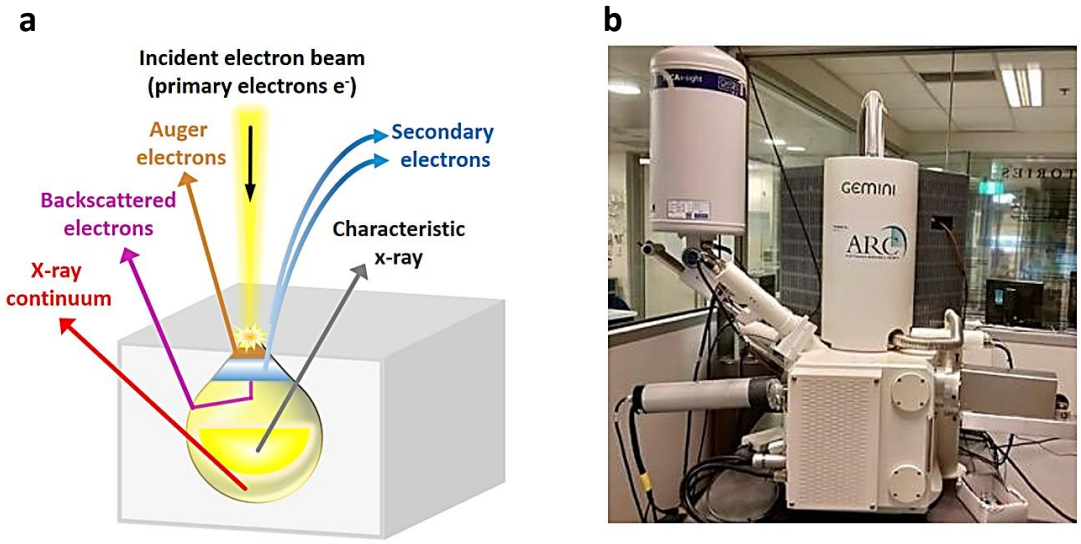

Figure 3.11. a) Schematic illustration of signals generated in a SEM by electron beam-sample interactions, and regions from which the different signals can be detected. b) The Zeiss Supra 55VP SEM used to investigate the structural features, morphology, and quality of the fabricated samples.

In this work the images were taken on the Zeiss Supra 55VP Scanning electron microscope for all stages of the project. The instrument is shown in Figure 3.11b. The Zeiss Supra 55VP SEM is a high-resolution Field Emission Scanning Electron Microscope (FESEM) with a Shottky source with RAITH E-beam Lithography System. Its high-efficiency in-lens detector produces exceptional quality images down to 0.1 kV for backscattered electrons BSE, and an Everhart-Thornley secondary electron detector and variable pressure secondary detector (VPSE) may also be used for imaging. An Oxford EDS system is available for elemental characterisation as is an Oxford Electron Backscatter Diffraction (EBSD) system for crystal orientation analysis and mapping.

Images of membranes and NDs were taken after attachment to flat metal stubs, while features such as microdisks were taken using a 45-degree inclined stage to see the height of structures. In the case of the thickness calibration images, samples were imaged using 90-degree stubs.

3.6 Atomic Force Microscopy

An atomic force microscope is a high-resolution scanning probe microscopy technique, with vertical resolution on the order of 0.1 nm, which is mainly employed to map surface topography. Instead of using light (optical microscope) or a focused electron beam (SEM), the probe is a sharp tip, with radius of ~10 nm, attached to one end of a cantilever with a spring constant of order 1N/m. The area of the scanning depends on the instrument design and typically reaches a few 100 nm to a few 10 µm. The imaging modes of AFM can be classified as: contact, tapping, and non-contact modes according to the tip motion. In this work Park XE7 AFM scanning probe microscope was used, and during the measurements the tiny needle scans the sample surface, while the changes in topography cause damping of its oscillations.

Figure 3.12. Park XE7 AFM scanning probe microscope. The inset shows a zoomed image of the scanning probe.

A photodetector captures the reflected light from a laser focused on the back side of the cantilever tracking the tip movement. The amplitude of cantilever oscillation is held constant by a feedback loop in the system. Consequently, the surface topography is interpreted as a change of feedback signal amplitude. And converted to an image. Figure 3.12. shows a schematic of the AFM system.

3.7 Raman Spectroscopy

Raman spectroscopy is a fast, non-destructive technique used to characterize materials and evaluate their quality and providing useful information concerning the phase purity and crystalline perfection of the diamond material.

Pure diamond has a simple Raman spectrum with a single sharp peak at 1332 cm^{-1} corresponding to the vibration of the sp^3 diamond lattice while graphitic hybridized sp^2 carbon gives rise to two peaks, each attributed to ring vibrations (Figure 3.13). The relative intensities of these vibrations may vary depending on the crystallinity. The “D” peak occurs at 1350 cm^{-1} and corresponds to atoms moving in radial directions in the plane of the graphitic sheet and appears as a result of dislocations in the lattice named “disorder-induced modes”. The intensity of this peak relative to the “G” peak can be used to determine the degree of disorder in the diamond sample. The “G” peak occurs at 1575 cm^{-1} which corresponds to neighbouring atoms moving in opposite directions perpendicular to the plane of the graphitic sheet. Raman from polycrystalline includes contributions from both sp^3 and sp^2 carbon. The ratio of the intensity of the diamond peak to the intensity of the “G” peak can be used to estimate the crystallite size and help to optimize the growth conditions.

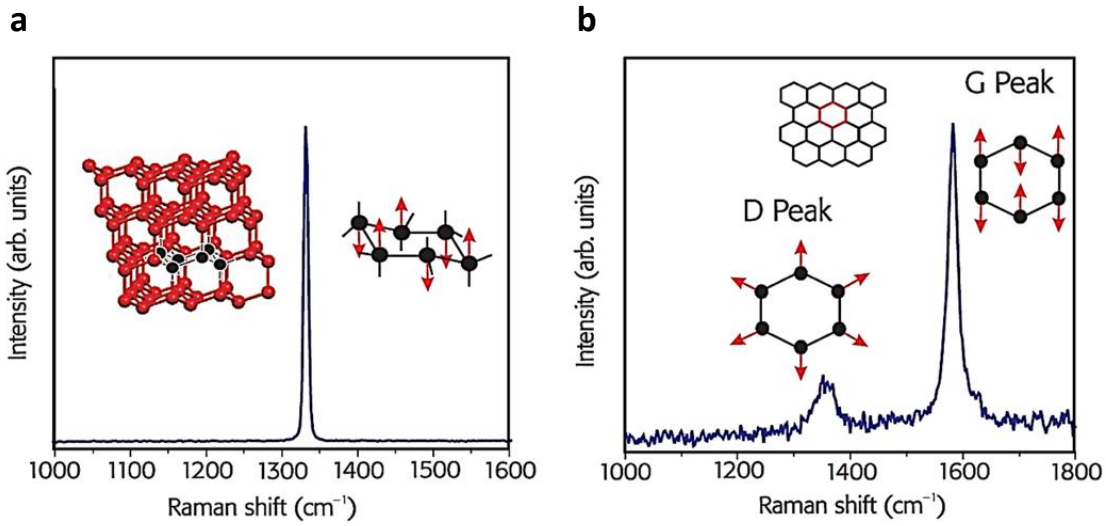

Figure 3.13. Raman spectra and corresponding lattice vibration for a) a single crystal diamond and b) graphite [193].

Raman spectroscopy can also be used to characterize the different types of defects present in diamond lattice. The introduction of specific dopants into a diamond can also have a strong impact on the strain of the lattice.

Chapter 4 Growth and doping of NDs by MPCVD

This chapter briefly describes the generation of optically active group IV emitters in nanosized diamond crystals. The generation of emitters in ND has been a useful and necessary step to test several doping recipes before applying them to the more precious SCD membranes.

4.1 Introduction

There have been consistent efforts devoted over the past decades, to fabricate NDs hosting optically active defects into devices for many technological applications. NDs can be safely used for bio-labelling [194] to analyze biological processes, for drug delivery, and to track or localize small molecules, proteins etc. [195-197]. However, of particular interest is the use of individual NDs that host single photon emitters for applications in quantum information technologies, quantum communication, and quantum sensing. [89, 108, 135, 198-202].

The most studied color centers in NDs are NV^- and SiV^- and their generation in mainly based on ion implantation and HPHT synthesis. In this work all the recipes available in the existing literature were tested before the development of our own protocols for generation of other group IV color centers such as germanium and tin by MPCVD.

4.2 Growth and characterisation

The features that an ideal fluorescent ND should possess are high sensitivity, high spatial resolution, high fluorescence quantum yield, high photo-stability (with no bleaching or blinking), and robustness.

The size of NDs for quantum application influences its optical properties and should be smaller than λ /n (where λ = wavelength of emitted light, n = 2.4 refractive index of diamond). Preferable crystals for NIR applications should be smaller than 300 nm.

In this work the objectives were to obtain well-dispersed, high quality, and well faceted NDs hosting the desired color centers.

The seeding of the sapphire substrates (chosen to minimize silicon incorporation during the growth) was based on the spraying method. NDs suspensions (4 - 6nm detonation NDs seeds in methanol with 0.01 mg/mL concentration) were sprayed onto the substrates and left to dry for 10 minutes at 40°C on a hotplate. Several growths were performed at different pressures. These results are presented in more detail in Chapter 7. Figure 4.1 shows the spraying equipment used for the seeding of the substrates as well as diamond distribution and individual, well faceted high quality NDs.

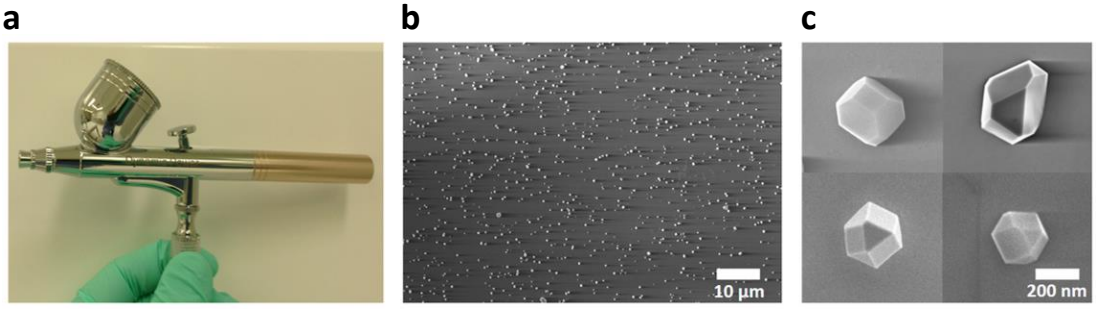

Figure 4.1. a) Spray gun used for seeding of the sapphire substrates with ND suspension. b) A sapphire substrate showing well dispersed individual NDs after 10 min MPCVD growth. c) Examples of individual NDs zoomed to evidence the well faceted growth and good morphology (samples grown at 60 Torr, 1% CH_4, 900 W for 10 minutes).

The spraying distance had to be optimized to avoid the formation of larger droplets and to obtain homogeneous distribution of NDs in order to grow individual nanoparticles (Figure 4.1c). The MPCVD growth was performed at the pressures of 50, 60, 70 and 80 Torr, in a hydrogen/methane atmosphere of 100:1 ratio, a

microwave power of 900 W was used, and growth was performed for 10 min on the sapphire substrates already coated with the doping solution.

Chapter 5 Bottom up doping of single crystal diamond membranes with germanium vacancy color centers

This chapter gives details about the development of a reliable method for incorporation of germanium color centers in thin single crystal diamond membranes by employing solid precursors during MPCVD overgrowth. This method consists of a combination of precursors such as metallic germanium and germanium dioxide powder together to achieve incorporation and a homogeneous distribution of emitters. I performed the fabrication of the membranes, doping, experimental data analysis and designed the figures. Kerem Bray performed the PL measurements; Igor Aharonovich and Milos Toth were involved in planning and supervised the work. Blake Regan fabricated the photonic devices and performed the measurements. Mehran Kianinia aided in interpreting the results and worked on the manuscript. All authors discussed the results and wrote the manuscript.

5.1 Abstract

Color centers in diamonds have garnered significant attention for applications in integrated quantum photonics. The availability of thin (~ hundred of nanometers) diamond membranes is paramount to achieve this goal. This chapter describes a robust, reproducible, and cost-effective method that enables engineering of high-quality thin diamond membranes with uniform distribution of germanium vacancies by employing microwave plasma chemical vapor deposition (MPCVD). The combination of different solid precursors for doping of the membranes increases the probability of germanium incorporation into the diamond lattice. This fabrication methodology can be further extended to implementation of other color centers in thin diamond membranes and be used for engineering quantum photonic devices.

5.2 Introduction

The recent improvements in the growth techniques and availability of synthetic diamonds enabled the development of new engineering materials for advanced, electronic, thermal, and quantum applications [48, 85, 154, 156]. The latter is particularly motivated by the availability of color centers in diamonds that act as single photon sources [80]. In particular, the recent focus on group IV - vacancy defects (e.g., silicon, germanium, tin, or lead vacancies) has spurred a new wave of research into generation of these color centers [124]. One of the key goals is to integrate these color centers with photonic resonators such as microdisks and photonic crystal cavities [203-205]. The fabrication of the resonators requires large scale, thin diamond membranes that are used as the building block for the resonators.

Whilst the fabrication processes of diamond membranes have been significantly refined over the last several years resulting in robust and mature technology [153, 160, 161, 166, 168, 206-208], the homogeneous in-situ doping of diamond membranes with new color centers presents still a major challenge. While doping of some of the elements (e.g. Ge or Si) [209, 210] is possible during high pressure high temperature growth (HPHT), this method is not applicable to membranes, as they would shatter under the severe conditions. Another avenue that has been explored is ion implantation [20, 104, 139, 142, 144]. However, this often results in non-ideal emission lines (broadened and enhanced spectral diffusion), due to residual strain that cannot be fully recovered using standard high temperature annealing. HPHT annealing has been shown to brighten some of the group IV defects and make the luminescence lines narrower (e.g. SnV^-) [20], but it cannot be used for diamond membranes due to their small thickness.

Alternatively, bottom up doping during growth is a promising avenue to incorporate fluorescent color centers [150]. This method has been explored widely to incorporate the SiV^- color center into growing diamond, primarily due to similar atomic properties and relatively comparable atomic size. Due to the presence of silicon in most chemical vapor deposition (CVD) chambers, either due to the use of silicon as a

substrate or due to the quartz walls, silicon is often incorporated into the growing diamond.

In this work we investigated the possibility of homogeneous incorporation of germanium vacancies (GeV^-) color centers into diamond membranes using microwave plasma CVD (MPCVD) process. GeV^- color centers possess a similar defect configuration to the SiV^- as explained in Chapter 3, but have a larger energy splitting in ground state compared to SiV^- (~ 170 GHz). The zero phonon line (ZPL) of the GeV^- is around 602 nm, and it is envisioned to possess a higher fluorescence quantum yield. All above-mentioned characteristics make this color center appealing for quantum information processing applications [124].

5.3 Experimental section

The overgrowth of diamond using MPCVD process involves volatile chemicals and many surface reactions of a vapor phase and dissociation of H_2 and CH_4 to produce gaseous precursors necessary for the diamond growth. As schematically illustrated in Figure 5.1a. and described in detail in Chapter 3, diamond layer forms from an activated mixture of hydrocarbon gases and hydrogen. Incorporation of impurities during growth can also happen at the same time.

The diamond membranes were generated using ion implantation and lift-off technique. Briefly, a bulk type IIa (100) single-crystal diamond (Element six) was implanted with helium ions at 1 MeV with 5 x 10^{16} ions/cm^2 followed by 900°C high vacuum annealing for 1 hour. The sample was then immersed in deionized water and a constant voltage of 60 V to lift-off of the membranes was applied. An SEM image of a 1.7 µm thick diamond membrane is shown in Figure 5.1b. After each growth, the membrane was flipped and thinned to ~ 300 - 500 nm using Inductively Coupled - Plasma Reactive Ion Etching (ICP-RIE) to remove the original damaged membrane. The etching takes place in the presence of argon, oxygen and SF_6 at 45 mTorr with

ICP power of 500 W and RIE of 100 W for 18 minutes to reach the required thickness. An SEM image of a thinned diamond membrane of ~ 300 nm is shown in Figure 5.1c.

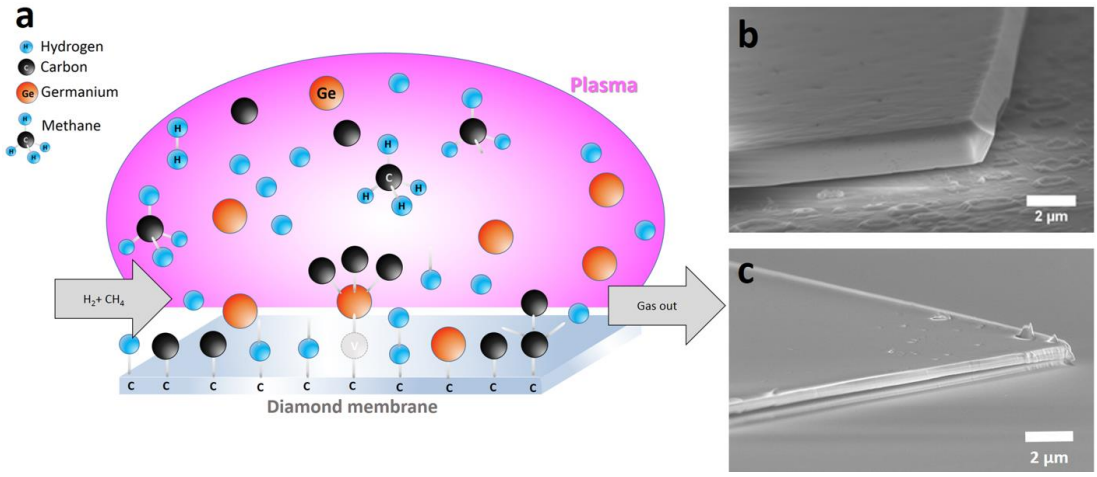

Figure 5.1. a) Incorporation of Germanium during MPCVD growth of diamond. The precursors are dissociated in the plasma region, creating active species which will eventually incorporate into the growing diamond. b) Representative SEM image of a thick 1.7 µm and c) a thin diamond membrane ~ 300 nm.

To incorporate germanium into diamond membrane, three different approaches using pure metallic germanium, germanium oxide (GeO_2) or the combination of the metallic and oxide precursors were investigated as shown in Figure 5.2. The germanium sources were positioned in close proximity to the membranes during the growth, as explained below.

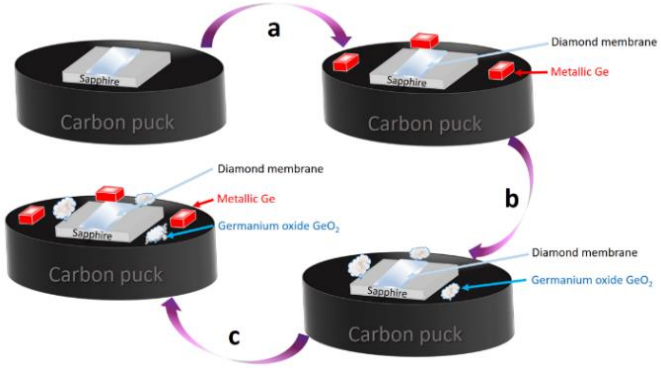

Figure 5.2. Schematic illustration of three approaches for germanium incorporation into diamond membranes by MPCVD using solid precursors: a) metallic germanium, b) germanium dioxide, and c) a combination of both metallic and oxide sources.

5.3.1 Metallic germanium as a precursor

In the first approach to generate GeVs, three pieces of metallic germanium with the size of ~1 mm^3 each, were placed on a carbon puck (of diameter ~ 2.5 cm) about one cm away from the diamond membrane sitting on a sapphire substrate as illustrated schematically in Figure 5.3a. The diamond membrane is located approximately in the middle of the sapphire sample that is used as a carrier. Sapphire is chosen intentionally as it does not result in silicon contamination. The sample was then overgrown for 8 minutes at 60 Torr with 900 W of microwave power in hydrogen/methane (with the ratio of 400/4 sccm) atmosphere. An optical image of the overgrown membrane is shown in Figure 5.3b. The surface of the membrane is rough after the growth, with many secondary nucleation spots. Metallic germanium has a relatively low melting point of ~ 937°C, that caused excessive sputtering of germanium during the growth. While on the one hand it should have been advantageous for incorporation of germanium into the growing diamond, it resulted in micromasking and induced secondary nucleation. As a result, a square pattern appeared on the diamond, as shown optically in Figure 5.3b and in a scanning electron microscope (SEM) image in Figure 5.3c.

The incorporation of GeV was examined using a confocal photoluminescence (PL) setup. A 532nm laser excitation with high numerical objective (NA = 0.9) was used as excitation source. In this batch of diamond membranes that were overgrown with only a metallic germanium source, we could not observe any emission from GeV centers, as shown in Figure 5.3d. This could be due to vaporizing of the germanium during high temperature growth before it is embedded into the diamond structure. Also, increasing the distance of the metallic source from the membrane did not lead to any germanium incorporation.

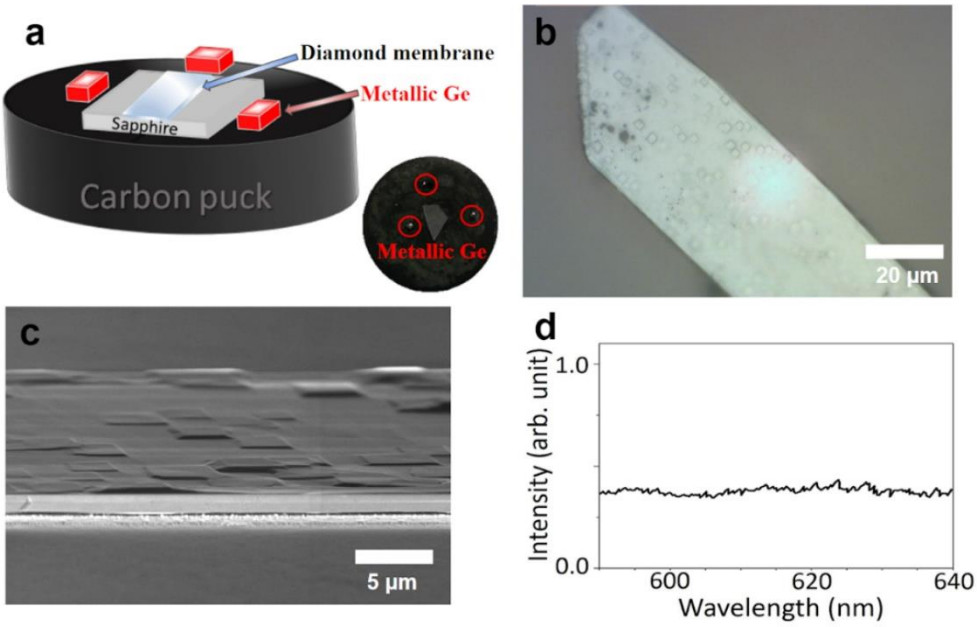

Figure 5.3. Incorporation of GeV using metallic source. a) Schematic of the growth geometry of the diamond membrane and metallic sources. Inset, is the actual photograph of the puck with diameter of ~ 1 inch. b) Optical and c) SEM images of the membrane after overgrowth process in MPCVD. Visible square areas in SEM image is the result of secondary nucleation from micromasking with sputtered germanium during the growth. d) PL spectrum from the membrane after overgrowth did not show any peak at ~602 nm from GeV centers.

5.3.2 Germanium dioxide as a precursor

In the second approach, a germanium oxide, which has higher melting temperature (~ 1,115°C), was used to resolve the issue with the sputtering of metallic germanium. Three pressed germanium dioxide (GeO_2) powder pieces of 1 mm^3 were placed about 1 cm away from the diamond membrane on a carbon puck, which had undergone the same overgrowth process. This is schematically shown in Figure 5.4a. An optical image shown in Figure 5.4b indicates the smooth growth of diamond membrane which is also evident in the SEM images of the membrane in Figure 5.4c.

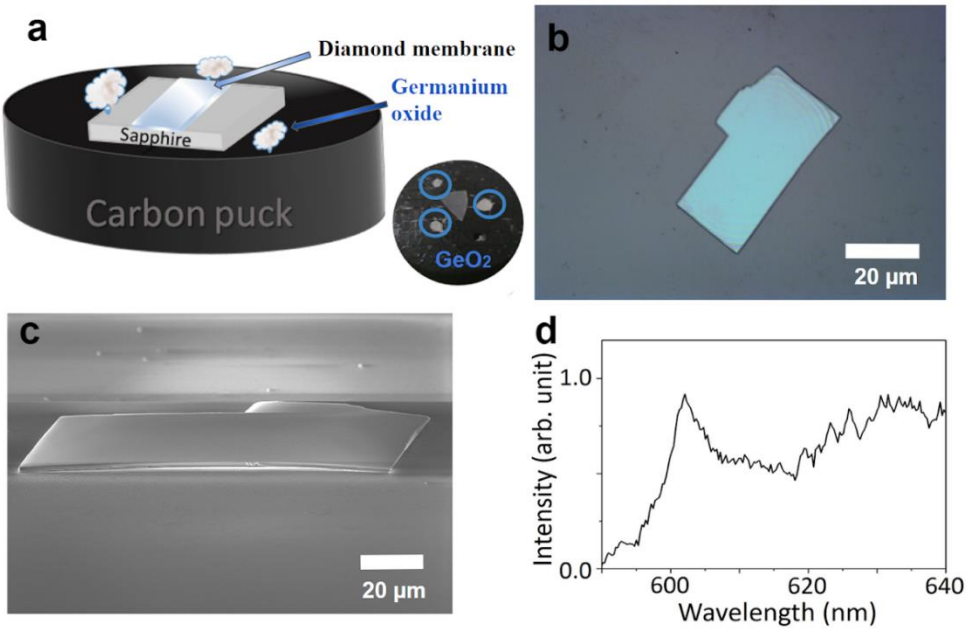

Figure 5.4. Incorporation of GeV using a germanium oxide source. a) Schematic of the growth geometry of the diamond membrane and oxide sources. Inset, is the actual photograph of the puck with diameter of ~ 1 inch. b) Optical and c) SEM images of the membrane after the overgrowth, resulting in smooth surface after the growth. d) Room temperature PL spectrum of the membrane, with the peak centered at ~ 602 nm confirms the successful incorporation of GeV into the diamond membrane.

The smooth appearance of the membrane without secondary nucleation, confirms that the sputtering process which happened in the first approach, has been eliminated. In addition, the PL characterization of the membrane showed the emission from GeV^- centers at ~ 602 nm confirming the incorporation of germanium into the membrane during the growth (Figure 5.4d). However, the amount of incorporation is relatively low (as indicated by the low intensity of GeV^- emission) most likely due to the slow release of the Ge atoms from the oxide during the growth. Such a method could be explored in the future to incorporate single GeV defects.

5.3.3 Metallic germanium and germanium dioxide combination

In the third approach, both sources were used to incorporate more germanium into the diamond lattice. To increase the amount of germanium during the growth, three metallic germanium pieces of ~1 mm^3 were placed on a carbon puck along with three pressed GeO_2 powder pieces with similar sizes all around the sapphire substrate, which is schematically shown in Figure 5.5a. The distance of germanium sources from the membrane was chosen to be around 1.5 cm to avoid the resputtering of metallic germanium on top of the diamond surface. An optical and SEM images of the diamond membrane after the same overgrowth process are shown in Figure 5.5b and Figure 5.5c, respectively. The membranes are mostly smooth without square patterns of nucleation. The PL spectrum recorded at room temperature from the overgrown membranes shows a bright characteristic GeV peak shown in Figure 5.5d.

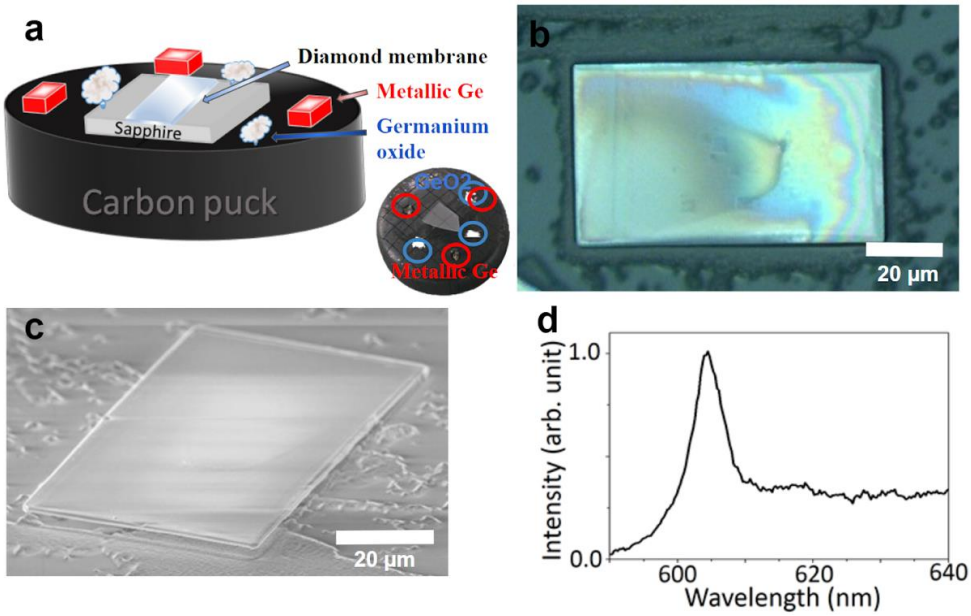

Figure 5.5. Incorporation of GeV using both metallic and oxide sources. a) Schematic of the growth geometry of the diamond membrane and metallic and oxide sources with larger distance compared to the previous approaches. Inset, is the actual photograph of the puck with diameter of 1 inch. The locations of both metallic and oxide germanium sources are marked. b) Optical and c) SEM images of the membrane after overgrowth process in MPCVD indicating the smooth surface after the growth. d) The pronounced peak at ~ 602 nm confirms the successful incorporation of GeV into the diamond membrane.

The plasma chemistry changes when adding metallic germanium to the oxide resulting in a higher concentration of Ge ions in the plasma and successful incorporation of germanium into the diamond lattice. During the growth with only metallic germanium source, the material causes sputtering, which has two effects. Firstly, resputtering on the diamond surface unintentionally masks the growth and therefore causes roughness in the membrane and non-uniform crystal structure. However, secondly, the metallic germanium at energy to ionise into the plasma is largely lost due to the physical sputtering away from the plasma center. This loss in energy and material is likely dramatically affecting the probability of incorporation. The oxide growth is there to address the issue of liquifying the metal, thus preventing sputtering. However, the dissociation rate of ions from the oxide into the chamber is lower than pure germanium due to the increased energy required to break the germanium-oxygen bond before an ion can be injected into the plasma and incorporate during growth.

The combination growth was designed with the notion that the oxide could passivate the metallic germanium sputtering during growth, causing a longer and more consistent release of germanium ions into the plasma. Therefore, the best results for the germanium incorporation were obtained by the combination of both the oxide and the metallic sources.

Germanium source	Growth conditions	Result
Metallic Ge	60 Torr, 900 W, 400/4 sccm H_2/CH_4 for 8 min	Micromasking and no incorporation of GeV
GeO_2 pressed powder	Same as above	Smooth surface and minimal GeV peaks
Metallic Ge, GeO_2 pressed powder around the sample	Same as above	Smooth surface with uniform distribution of GeV across the membrane

Table 5.1. Summary of the conditions used to achieve GeV color centres in thin diamond membranes.

The higher incorporation of GeV in the membrane is confirmed in our experiments and was the main goal for the current study; however, the detailed mechanisms can be further studied in the future. Table 5.1 summarizes the results of the three different approaches undertaken to create GeV color centers in the diamond membranes.

Given the promising result of the GeV doping using a combination of the oxide and metallic sources, these membranes can be used to fabricate photonic resonators. For the proof of principle, we first recorded PL spectra at random locations across the membrane to show that the incorporation is homogeneous.

Figure 5.6a shows three spectra that demonstrate the presence of GeV color centers. An intensity confocal map from the membrane grown with the third method is shown in Figure 5.6b.

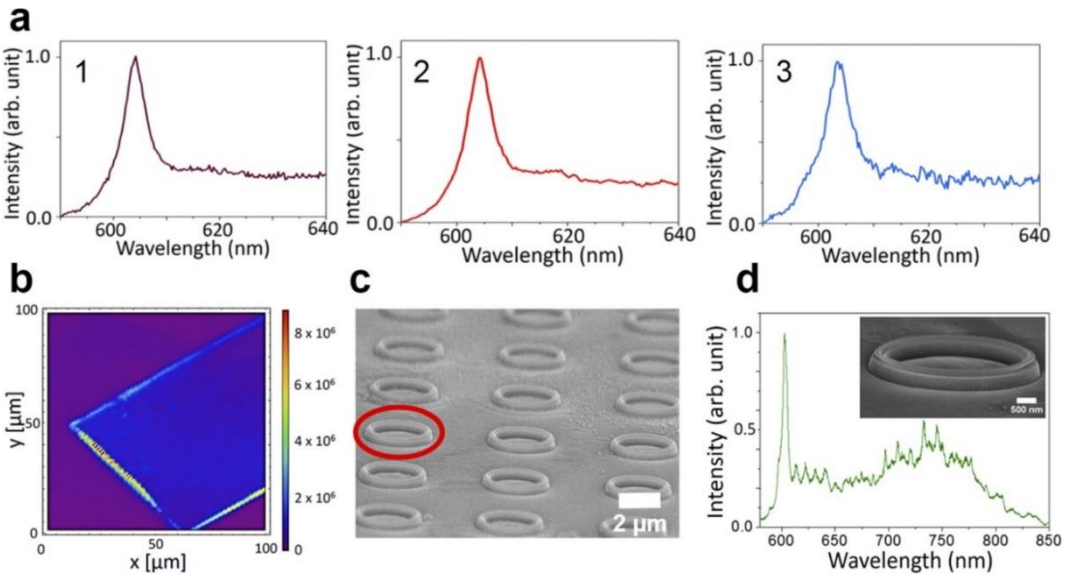

Figure 5.6. a) Room temperature PL spectra collected from three random position on the diamond membrane confirming the homogeneous incorporation of GeV into the diamond. b) An intensity confocal map from the membrane grown with the third method showing uniform distribution of GeV^- in all measured points across the membrane. c) Low magnification SEM image of the fabricated microring from diamond membrane containing GeV^- centers. d) PL spectrum from the diamond showing whispering gallery modes as well as GeV^- peak. Inset shows a zoomed image of one diamond ring.

The PL counts across the membrane are similar, indicating the homogeneous distribution of GeV in the membrane. Next, the same membrane was patterned to fabricate microring resonators. Figure 5.6c shows the patterned ring array with a 2.5 µm outer radius and 400 nm width rings. Although the membrane still rests on a substrate, whispering gallery modes were found in most of the rings. A representative of the PL spectrum obtained from the one of the ring cavities indicated with the red circle in Figure 5.6c, is shown in Figure 5.6d. The smaller periodic peaks correspond to fundamental modes with an average quality factor of Q ~ 500. The narrow bright peak at 602 nm in Figure 5.6d is GeV^- zero phonon line coupled to whispering gallery modes (WGMs). The linewidth of the narrowed GeV^- peak is reduced in the photonic resonator to 2.8 nm and the average linewidth of supported modes is ~ 1.2 nm.

5.4 Conclusions

The details on best avenues to incorporate germanium into diamond using solid sources to generate GeV^- color centers, while maintaining high quality growth and smooth diamond membranes, were presented. The most promising condition for doping is the combination of metallic and oxide germanium sources. Our work can be extended by optimising the growth conditions to incorporate single GeV^- centers (e.g., reducing the amount of oxide in the chamber) or by employing the same technique to incorporate other group IV defects, such as tin or lead vacancies. Overall, the bottom up doping of diamond is a promising avenue as it avoids ion implantation and enables direct incorporation of color centers into a diamond membrane without damage, that can be immediately processed for photonic resonators.

Chapter 6 Single crystal diamond membranes and photonic resonators containing germanium vacancy color centers

In this chapter, a robust method to engineer microdisk and microring resonators containing the GeV^- color centers is presented. The resonators are fabricated from single crystal diamond membranes (~300 nm) that were overgrown in a presence of germanium to achieve smooth diamond crystal that contains ensemble of bright GeV^- emitters. The doping approach consists in a combination of a direct dropcast of solution of germanium dioxide on top of the membrane combined with the use of metallic germanium as additional doping source.

Aleksandra Trycz, Kerem Bray, Blake Regan, Rodoflo Previdi and Gediminas Seniutinas were involved in fabrication, doping, and growth of diamond membranes. Kerem Bray, Blake Regan and Aleksandra Trycz performed the photoluminescence measurements; Kerem Bray analysed the data. Kumaravelu Ganesan carried out the ion implantation. Mehran Kianinia performed the cryogenics measurements. Sejeong Kim performed the simulations. Igor Aharonovich and Sejeong Kim supervised the project. All the authors discussed and wrote the manuscript.

6.1 Abstract

Single crystal diamond membranes that host optically active emitters are highly attractive components for integrated quantum nanophotonics. This chapter describes another route towards the bottom-up synthesis of single crystal diamond membranes containing germanium vacancy (GeV^-) color centers. The lift-off technique was employed to generate the membranes and the chemical vapour deposition was performed in a presence of a germanium source to realize the in-situ doping. Finally, I show that these membranes are suitable for engineering of photonic

resonators such as microdisk cavities with quality factors of ~ 1500. The robust and scalable approach to engineer single crystal diamond membranes containing emerging color centers is a promising pathway for realization of diamond integrated quantum nanophotonic circuits on a chip.

6.2 Introduction

Color centers in diamond are attractive building blocks for solid state integrated quantum photonics [211, 212]. So far, significant effort has been devoted to study the nitrogen vacancy (NV^-) center due to its long electron spin coherence time and, hence, its applicability as a spin qubit and a sensor [43, 213]. However, its optical properties are not ideal as it has a large phonon sideband with only ~ 4% of the fluorescence being emitted into the zero phonon line (ZPL). The NV^- center also has a permanent dipole moment which makes it highly susceptible to surrounding electrostatic fields. These fields result in spectral diffusion of its optical transitions, and reduce the generation rate of indistinguishable photons [214, 215].

To overcome these shortfalls, new color centers with inversion symmetry based on group IV elements in diamond has been recently explored. Following on detailed investigations of the negatively charged silicon vacancy (SiV^-) [216-223], other color centers including germanium vacancy (GeV^-) [140, 224-228] and more recently tin vacancy (SnV^-) [142, 229] have been identified. The defects have an inversion symmetry and therefore are less vulnerable to electrostatic field variations. Indeed, recent reports showed that generation of Fourier Transform limited photons is possible employing SiV^- centers in both nanodiamonds and bulk, and fabricated nanostructures using a reactive ion etching process [221, 230, 231] and their optical and spin transition frequencies can be efficiently tuned using engineered strain environment [232]. On the other hand, the advantage of the GeV^- and the SnV^- is their larger energy splitting in the ground state that reduces the phonon mediated spin mixing, to achieve better coherent spin manipulation [146, 233]. In addition, the GeV^- color center is believed to

have a much higher quantum efficiency [224] compared to the SiV^-, due to negligible multiphonon relaxation pathways [224], therefore being advantageous for applications in quantum optics and nanophotonics. To employ these color centers in integrated nanophotonic devices, an interface between the spin and the emitted photons is needed. Towards this goal, a promising avenue is an integration of these color centers with photonic resonators [211, 220, 234-237].

6.3 Experimental section

6.3.1 Direct drop cast of germanium dioxide solution and metallic germanium source

The diamond membranes (from bulk type IIa (100) faceted SCD, Element six) were generated using ion implantation and liftoff, as described in details previously [153, 238, 239]. To generate the GeV^- color centers, the membranes were transferred onto a sapphire substrate using a liquid droplet of germanium dioxide (GeO_2) powder (SigmaAldrich) – as shown in Figure 6.1a. The droplet contains a 0.5 mg/mL solution of GeO_2 powder in ethanol. The sapphire substrate with the GeO_2 covered membrane was then placed in a MPCVD chamber, along with a ~1 mm^3 piece of metallic germanium positioned approximately ~ 1 cm away from the diamond membrane (Figure 6.1b). The CVD growth conditions were a hydrogen/methane ratio of 100:1 at 60 Torr, a microwave power of 900W for 10 minutes to fabricate a ~ 400 nm intrinsic diamond layer that contains ensemble of GeV^- color centers. The incorporation of the germanium into the diamond occurs via the plasma phase. Upon the microwave plasma, the oxide and the metallic source melt, producing germanium vapour that is then incorporated into the growing diamond. To remove the original diamond that did not contain the GeV^- color centers, the membranes were flipped and thinned by ICP-RIE in the presence of oxygen, argon and SF_6 at a pressure of 45

mTorr for 18 minutes (Figure 6.1c). The gas flow ratio during RIE is SF6:Ar:O_2 (5:10:15 sccm). This fabrication process results in a single crystal diamond membrane with a thickness of 300 nm (Figure6.1d).

6.3.2 Characterization of the membranes

Representative side view scanning electron microscope (SEM) images of the overgrown and the final (thinned) membrane are shown in Figure 6.1e and Figure 6.1f, respectively. The surface roughness of the original, overgrown and thinned membrane was determined by an atomic force microscope (AFM), after each fabrication step. The slight curve observed in Figure 6.1f is likely due to residual strain within the diamond membrane. The AFM measured surface profiles are shown in Figure 6.1g, and reveal minimal surface roughness of ~ 1 nm. Therefore, the overgrowth method in the presence of germanium does not hinder the smoothness nor reduces the quality of the final single crystal diamond membrane.

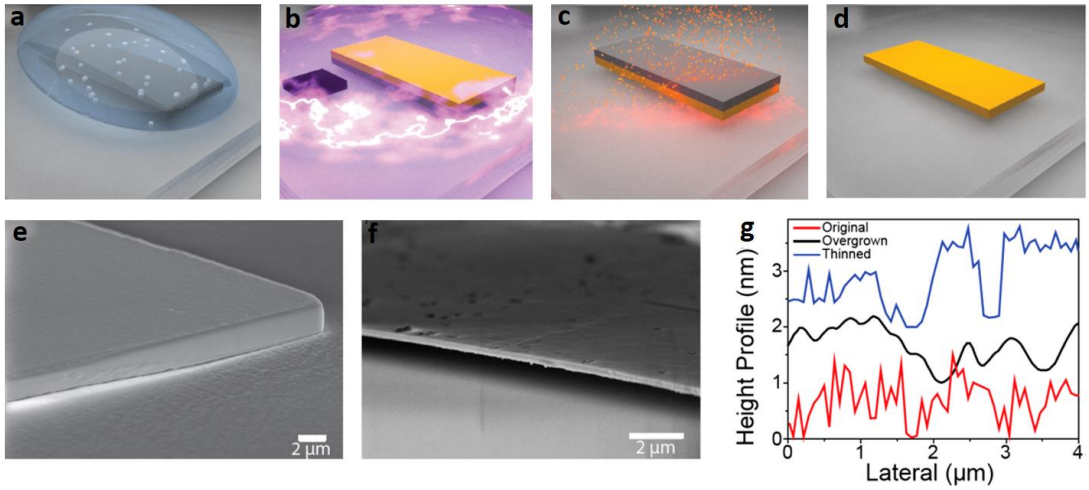

Figure 6.1. Schematic illustration of the fabrication process to engineer single crystal diamond membranes containing GeV^- color centers. a) An electrochemically etched single crystal diamond membrane (dark grey) is transferred to a sapphire substrate using a 0.5 mg/mL GeO_2 solution in ethanol. b) Subsequent MPCVD overgrowth with an additional

metallic germanium source nearby. c) The sample is flipped and thinned by ICP-RIE, to remove the original material to generate d) a diamond membrane with GeV^- centers (yellow). e), f) Representative SEM images of the overgrown and the final (thinned) diamond membrane, respectively. The thicknesses of the original and the thinned membrane are ~ 2.10 µm and ~ 0.3 µm, respectively. g) AFM scans of the surface roughness of the original (red curve), overgrown (black curve) and thinned (dark blue curve) diamond membranes. The surface roughness of these membranes is ~1 nm. The curves are off-set in 1 nm intervals for clarity.

Doping growing diamond with germanium requires substantially different conditions than these needed for incorporation of silicon. Silicon is naturally present in most of the diamond chambers (quartz windows, or residual contamination), and is efficiently incorporated into the growing diamond as SiV^- without sacrificing the diamond growth. However, the incorporation of germanium requires an additional germanium source. In addition, melting point of metallic germanium is significantly lower than silicon (~ 940˚C vs 1400˚C) and so one cannot utilize germanium as a growth substrate. In addition, this process should not introduce growth artefacts such as secondary nucleation [238](as described in Chapter 5). When growing on a bulk diamond, this task is easier, since the external doping source is often smaller in size compared to the large diamond crystal and power densities can be much higher [189]. In the case of a thin diamond membrane, it is different and requires tuning of the growth conditions. In addition, the growth should result in a uniform distribution of the germanium. To the best of our knowledge, such a growth was not demonstrated yet, as majority of GeV^- doping is done only via high pressure high temperature growth [226]. The uniformity in our case, was achieved by using an additional Ge containing layer – namely a GeO_2. In this experiment we found that when the metallic germanium is the only source during growth, the GeV^- color centres appeared along the edges of the membrane, while there is no GeV^- present in the middle, top surface of the membrane. The small amount of metallic germanium employed didn't lead to the secondary nucleation and resputtering of the material on the diamond surface, but neither led to the creation of emitters in the membrane lattice. Figure 6.2a shows

the confocal map of a membrane grown with only one metallic germanium. GeV^- color centers are formed only at the edges, with no visible lines in the middle.

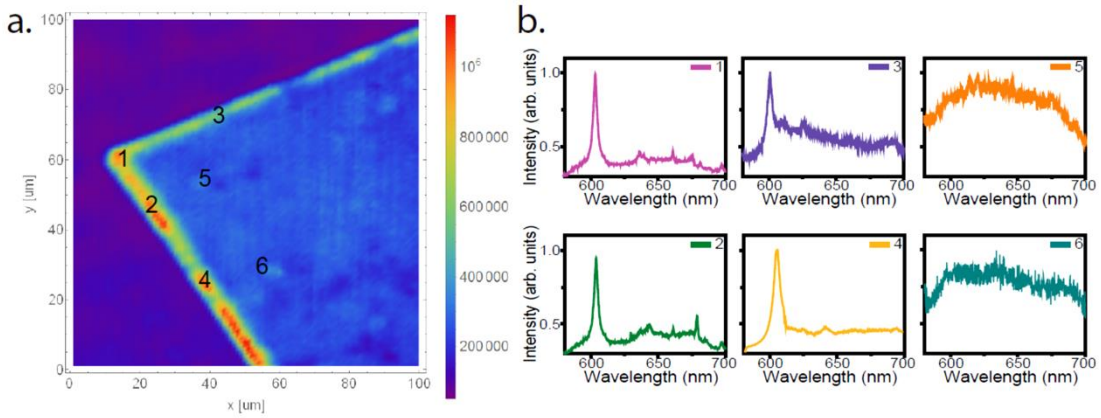

Figure 6.2. GeV^- incorporation into the membrane when only one metallic source is used. a) A confocal map of the membrane. b) Six typical spectra from points 1 – 6 in a). GeV^- is incorporated only at the edges.

On the other hand, the addition of the GeO_2 increases the incorporation of Ge into the top surface of the growing diamond, resulting in a uniform GeV^- distribution.

6.3.3 PL measurements at room and cryogenic temperatures

To study the optical properties of the diamond membranes, photoluminescence (PL) measurements were recorded under a continuous-wave 532 nm laser (Gem 532, Laser Quantum) excitation at room and cryogenic temperatures using a standard confocal microscope. Figure 6.3a shows a RT PL spectrum of the thin (~ 300 nm) diamond membrane with the bright GeV^- ZPL at 602 nm and a full width at half maximum (FWHM of ~ 0.8 nm). Inset, is the schematic illustration of the GeV^- defect, that consists of an interstitial Ge atom splitting two vacancies in a diamond lattice. In some locations along the membrane, an additional peak around ~ 641 nm was also observed. This luminescence signal can potentially be attributed to phononic replica

(vibronic band) of the GeV^- center. Furthermore, the ~ 641 nm peak was not observed in overgrown membranes without a germanium source, and likewise, this peak was never observed without the ZPL at 602 nm. At this point we do not have a concrete evidence for the unambiguous identification of this peak.

The PL spectrum from the same membrane recorded at 15 K is shown in Figure 6.3b. At cryogenic temperature, the PL spectrum from the GeV^- emitters in low strain material splits into four lines corresponding to the transitions from the low (high) branch of the ground state to the low (high) branch of the excited state [224, 227]. The four distinct PL lines are clearly visible in Figure 6.3b, corresponding to the optical transitions of the ZPL. Inset, is the schematic electronic level structure of the GeV^-, with the splitting in the ground and excited states. The ground state splitting ($\Delta E_{1\rightarrow2}$ ~ 165 GHz) while the excited state splitting is ($\Delta E_{3\rightarrow4}$ ~ 1159 GHz) in accord with the reported literature [224, 227].

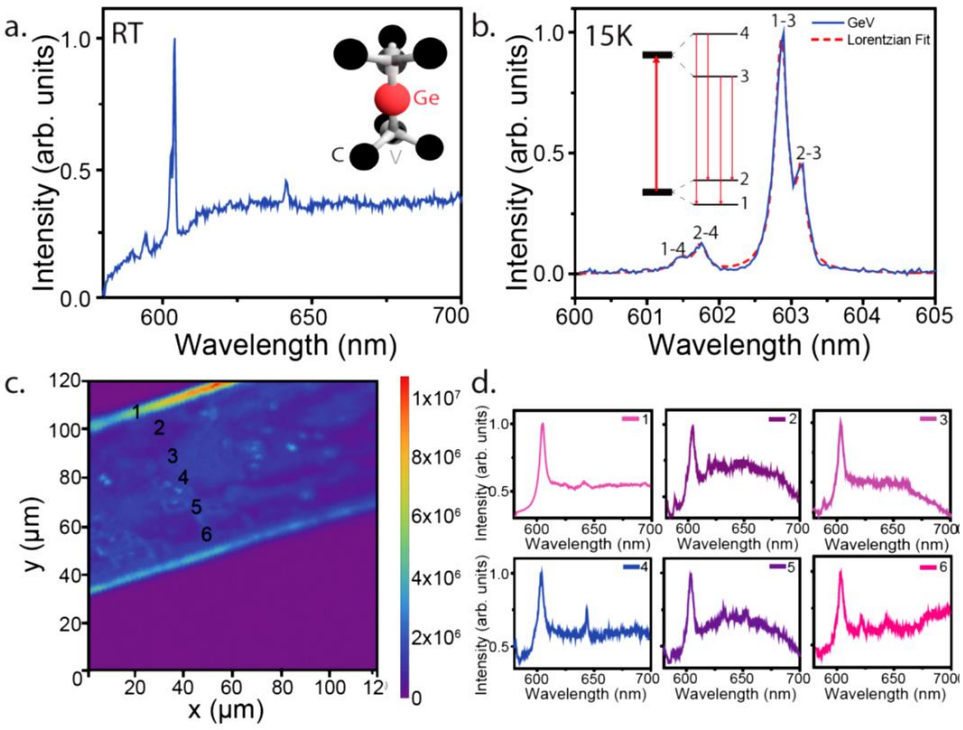

Figure 6.3. Spectra of the diamond membranes doped with ensemble of GeV^- centers. a) A RT spectrum showing a characteristic peak at 602 nm. Inset, schematic structure of the GeV^- color center. b) A spectrum of the GeV^- ensemble taken at 15K (blue curve), with the characteristic splitting corresponding to the transitions from the excited to the ground state

manifolds. The red dashed line is a double Lorentzian fit. Inset, is the schematic of the electronic level structure of the GeV^-. c) A confocal map of the overgrown diamond membrane where each number corresponds to a spectrum in d) showing the uniform distribution of the GeV^- emitters. d) Six representative RT spectra of the GeV emitters in the diamond membrane, showing a uniform distribution of the GeV^- emission.

An important prerequisite for scalable devices is a uniform distribution of the color centers. This is important for various applications such as ensemble magnetometry or cavity cooperativity schemes [240, 241], as well as for practical aims to enable patterning of multiple devices on a single membrane. Figure 6.3c shows a confocal scan of the diamond membrane containing the GeV^- emitters. The RT spectra in Figure 6.3d were recorded at ~ 10 μm intervals across the membrane, from the locations marked with numbers 1 – 6. Each point shows the typical GeV^- peak at ~ 602 nm (Figure 6.3d), confirming a uniform distribution of the emitters. Note that point 1 is at the edge of the membrane and hence appears brighter. For the other spots on top surface of the membrane, the variability in the emission spectra is less than 10%.

Finally, we utilize the diamond membranes to fabricate microdisk and micro-ring cavities which are commonly used as photonic resonators [242, 243]. A hydrogen silsesquioxane (HSQ) hard mask was deposited on top of the overgrown and thinned membrane and an array of microdisk cavities were patterned using Electron Beam Lithography (EBL). The HSQ mask was transferred into the diamond membrane through an Oxygen/argon etch: O_2/Ar 45:5 sccm, under 10 mTorr chamber pressure, 500 W ICP and 100 W RIE power. Figure 6.4a shows a low magnification SEM image of the patterned devices. The microdisks have a 5 μm diameter and 5 μm spacing (edge to edge) between each disk (Figure 6.4a), while the micro-rings have a 5 μm outer diameter and a width of 400 nm. The diamond membrane is outlined for clarity with a blue dashed line. Figure 6.4b shows a false color SEM image of the diamond microdisk with a thickness of ~300 nm, resting on the SiO_2 substrate, while Figure 6.4c shows a false color SEM image of the diamond microring cavity.

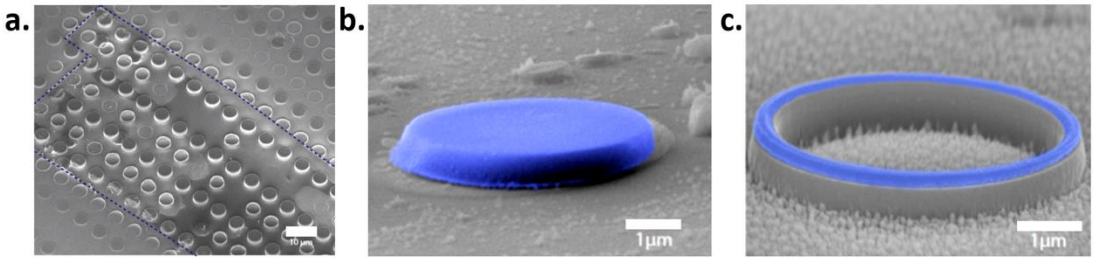

Figure 6.4. Diamond microdisk and microring cavities fabricated from the overgrown diamond membranes containing GeV^- color ceters. a) Low magnification SEM image of microring and microdisk resonators with a diameter of 5 µm etched into the diamond membrane (blue dashed line). b), c) False color SEM images of a diamond microdisk and a diamond microring, respectively. The diamond are false colored blue for clarity.

Figure 6.5a shows a PL spectrum recorded from a typical diamond microring. Both the microdisks and the microrings support propagation of whispering gallery modes (WGMs) that are manifested as periodic peaks within the spectrum. For the current microring size, the spacing between adjacent modes should be ~ 14 nm. The PL emission is decorated by narrow lines, which are the modes of the optical cavity, while a GeV^- ZPL is visible at 602 nm. Quality factors *Q* as high as 1500 were observed from these devices. A particular mode that is in a close proximity to the GeV^- ZPL at 596 nm exhibits a Q ~ 750. A high resolution spectrum from two modes at ~ 750 nm (Figure 6.5b) show Q ~ 1500. The losses occur due to an increased roughness from the imperfect HSQ mask removal and from the leakage to the underlying SiO_2 substrate.

Figure 6.5c shows the modelling result of the diamond microring (n = 2.4) of the same geometry resting on a silicon dioxide substrate (n = 1.5) using a finite-difference time-domain (FDTD) method (Lumerical Inc.). The structure support 1st order radial Transverse electric (TE) modes as indicated in the spectrum. As an example, electric field profile of $TE_{1,74}$ mode is shown in inset. Other peaks in the spectrum are higher order radial modes including 2nd and 3rd radial modes. $TE_{2,62}$ is shown in the inset. A very good matching between the measured the simulated spectra is observed. The dominant presence of the 1st order modes at the longer wavelength range while the

lower wavelength range also supports higher order modes as evidenced by closed spacing of the peaks.

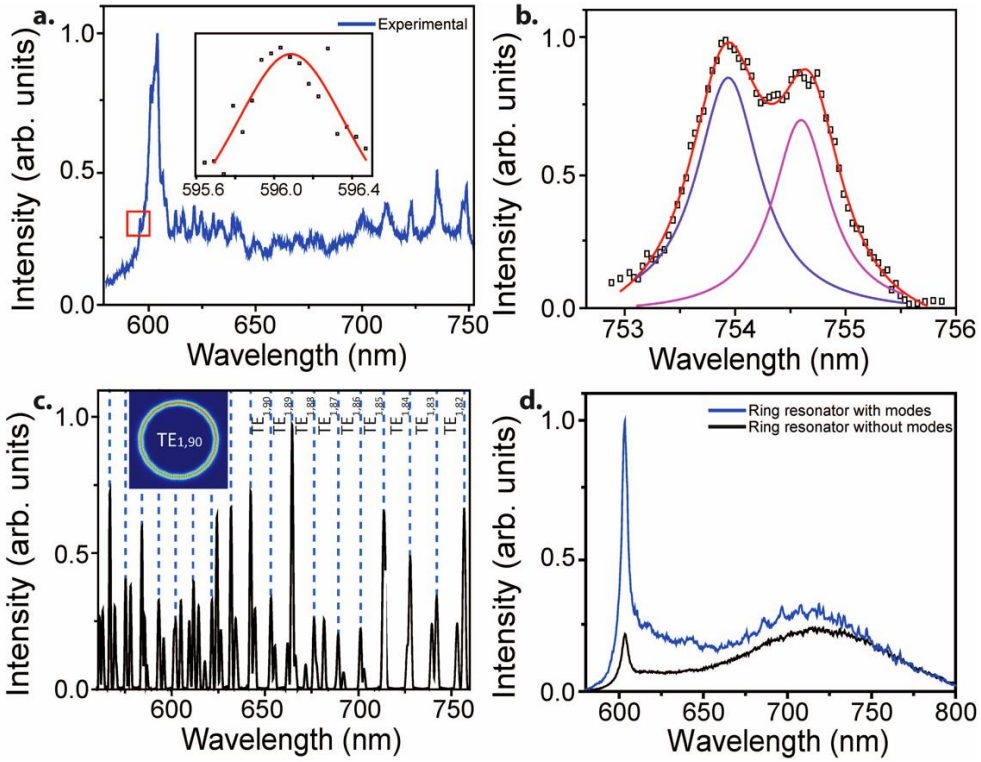

Figure 6.5. a) PL spectrum recorded from the diamond microring cavity under 532 nm excitation at room temperature. WGMs are clearly visible. The ZPL of the GeV^- center is observed at 602 nm. Inset, a zoom in spectrum of the mode at 596 nm. The red line is a Lorentzian fit. b) a spectrum of a WGM at ~ 755 nm, showing a Q ~ 1500. c) Simulation data of the microring sample. Inset, FDTD field profile of the 1st order mode. d) Comparison of emission from ensemble of GeV color centers recorded from a working microring where the GeV^- ensemble is coupled to the WGMs (blue curve), compared to a microring that does not show WGMs fabricated from the same membrane (black curve).

The fabricated devices enable higher collection of the emitted photons from the GeV^- color center. Figure 6.5d shows an emission enhancement from an ensemble of GeV^- centers coupled to WGMs compared to a microring that does not show any WGMs (most likely due to nanofabrication imperfections). Both devices were fabricated from the same diamond membrane. An enhancement of more than 4 is observed, which predominantly is due to the cavity effect. The coupled GeV ensemble also

exhibits lifetime reduction, as shown in Figure 6.6. Figure 6.6a shows lifetime of the GeV ensemble in a microring compared to GeV ensemble in a membrane. A lifetime reduction from ~ 6.6 ns to 2.8 ns is measured. The measurements were done at room temperature with a Fianium laser (532nm). A narrow filter was used to filter only the 602 nm GeV ZPL line. System response was measured to be 0.36 ns.

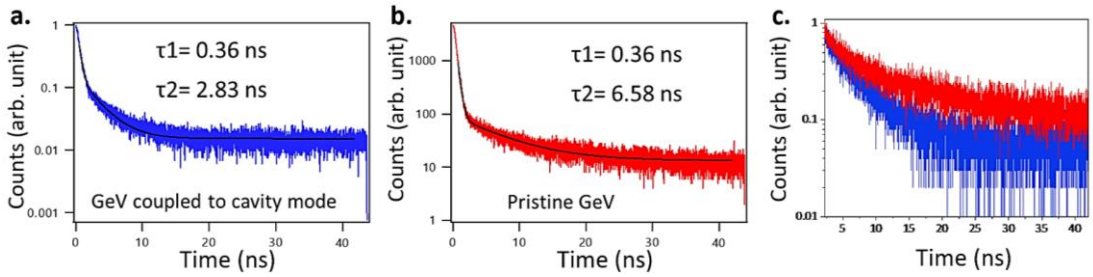

Figure 6.6. Lifetime of GeV ensembles in a) a coupled microring, b) membrane and c) comparison of the $Ge^{-}V$ signal only. The red curve is the pristine GeV^{-} while the blue one is the coupled ensemble.

6.4 Conclusion

In conclusion, I have described a robust method to engineer optically-active, single crystal diamond membranes containing ensembles of GeV^{-} emitters and further employed these membranes to produce microdisk and microring cavities containing GeV^{-} emitters with *Q* values of ~ 1500 that show enhanced emission from the GeV^{-} centers. Resonant excitation measurements would be needed to fully unveil the optical linewidths of the CVD GeV^{-} color centers. The presented method of doping the diamond membranes is advantageous and can also be applied for bulk crystals or NDs, without degrading the overgrown crystal quality. Furthermore, similar technique can be explored to achieve doping of diamond membranes with other emerging colour centres such as tin related emitters [142, 229] and other narrow band emitters [244]. Our results will accelerate the integration of new colour centres in

diamond with scalable photonic devices to achieve on-chip quantum nanophotonic circuitry.

Chapter 7 Controlled doping of GeV^- and SnV^- color centers in diamond using chemical vapor deposition

In this chapter I further extend the fabrication methods to include metallic oxide and chloride suspensions of germanium and tin to create desired color centers. An important factor to be considered for a successful incorporation of precursors in NDs and nanoscale SCD membranes consists in the correct matching of the melting temperature of the dopants to the temperature reached by plasma during the diamond growth in MPCVD chamber. A detailed process for generation of GeV^- and SnV^- emitters is described, obtaining a high quality diamond growth despite the utilization of inorganic precursors.

Aleksandra Trycz and Mika T. Westerhausen conceived the idea, performed the experiments and drafted the figures. Connor Stewart performed the PL measurements. Milad Nonahal aided in design of the figures. Blake Regan worked on the manuscript and performed the measurements. Igor Aharonovich and Mehran Kianinia were involved in planning and supervised the work. All the authors discussed the results and wrote the manuscript. Carlo Bradac and Kerem Bray contributed to this work with fruitful discussions. Chi Li and Johannes Fröch assisted with Raman spectroscopy.

7.1 Abstract

Group IV color centers in diamond (Si, Ge, Sn and Pb) have recently emerged as promising candidates for realisation of scalable quantum photonics. However, their synthesis in nanoscale diamond is still in its infancy. In this chapter the controlled synthesis of selected group IV defects (Ge and Sn) into nanodiamonds and nanoscale single crystal diamond membranes is demonstrated. We take advantage of inorganic

salts to prepare the chemical precursors that contain the required ions that are then incorporated into the growing diamond. Photoluminescence measurements confirm that the selected group IV emitters are present in the diamond without degrading its structural quality. Our results are important to expand the versatile synthesis of color centers in diamond by microwave plasma chemical vapour deposition.

7.2 Introduction

Color centers in diamond have become a working horse for exploration of light matter interactions at the nanoscale and demonstration of solid state quantum photonics experiments [72, 124, 205, 245-248]. Specifically, the group IV element complexes (namely the SiV^-, GeV^-, SnV^-, PbV^-, where V is a neighbouring vacancy) form narrowband, bright emitters and offer optical spin readout at cryogenic temperatures [20, 22, 104, 105, 125, 139, 142, 147, 150, 233, 249, 250]. So far the effort was predominantly focused on the SiV^- due to ease of fabrication of this color center [125, 233, 247]. Specifically, it was employed to realise basic quantum optics circuitry, explore photon - photon interactions and show two photon interference [1, 247].

The GeV and SnV have several advantages over the SiV. These color centers often exhibit improved photostability under resonant excitation [20, 145, 147, 251] and possess larger splitting in its ground state that is important for efficient spin manipulation [124]. The quantum efficiency of these emitters is also believed to be higher. Therefore there is an increasing need to controllably engineer these defects.

Several approaches have been recently explored to generate these emitters including ion implantation [22, 151, 229, 252] and doping during high pressure high temperature (HPHT) growth [141, 209, 210]. Both these methods present disadvantages and there is therefore an urgent demand to develop chemical vapor deposition (CVD) techniques that can be used to dope both single crystal diamond and nanodiamonds insitu during growth. In this work we realise a bottom up method to deterministically introduce both SnV^- and GeV^- color centers into diamond via microwave plasma

(MPCVD). We use inorganic compounds to introduce a layer of oxides and chlorides that serves two roles: first, it acts as a substrate onto which we place the nanodiamond seeds and single crystal diamond membranes. Second, it acts as a source for the doping. The minute amount of dopant used makes this both a safer and greener method for colour center incorporation compared to the previous gas phase MPCVD methods. Using this technique we are able to controllably introduce both SnV^- and GeV^- into the growing diamond without sacrificing the diamond quality. This facile and scalable method allows for substrate specific growth of germanium and tin related vacancies in diamond by MPCVD.

7.3 Results and discussion

The process is schematically depicted in Figure 7.1a-e. First, analytical grade (99.99%) germanium (IV) oxide (GeO_2), tin II oxide (SnO_2) and tin (II) chloride ($SnCl_2$) were diluted in ultrapure Milli-Q water to prepare the dopant coating. The concentration of all doping compounds was 10mg/mL in solution and were vigorously agitated before pipetting. Eight µL of doping suspension ($SnCl_2$/SnO_2 or GeO_2) was dropcast on a sapphire substrate of area ~ 5 x 5 cm^2 and left to dry into a film for 10 minutes at 40°C using a hotplate shown in Figure 7.1b. The use of sapphire substrates was chosen to minimise silicon contamination during the MPCVD growth. Then, either nanodiamonds (4-6 detonation nanodiamond seeds) or diamond membranes (see refs [161, 238, 253] for membrane fabrication) were placed on top of the dopant coating to grow either nanodiamonds or single crystal diamond, respectively (Figure 7.1c). For the nanodiamond growth, the seed suspension was sprayed onto the sapphire substrate at the distance of 30 cm to avoid the formation of larger droplets and maintaining the control on the density and distribution of nanodiamonds to grow individual nanoparticles. The diamond membranes were transferred to the substrate using liquid droplet transfer. The substrates were then left to dry for 10 minutes at 40°C on a hotplate. The growth was performed using a MPCVD process with a

hydrogen/methane ratio of 100:1 at 50, 60, 70 or 80 Torr, a microwave power of 900 W for 10 min (Figure 7.1d).

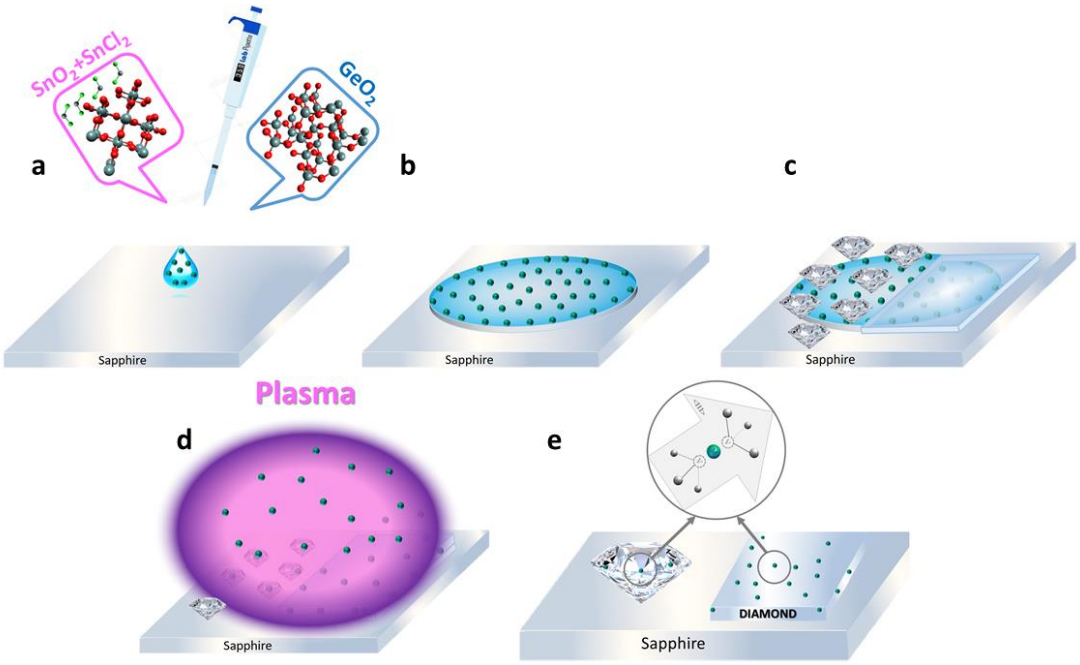

Figure 7.1. Schematic diagram of dropcast dopant for the incorporation of group IV color centers in CVD diamond growth. a) Dopant solution diluted in ultrapure Milli-Q water and dropcast on sapphire substrate at 40°C and left to dry for 10 minutes to prepare the dopant coating shown in b). c) Diamond membranes or nanodiamonds are transferred to dopant coating. d) CVD overgrowth of diamond platform. The plasma conditions slowly release dopant ions into plasma for incorporation. e) Resultant overgrown diamond with incorporated group IV defects in diamond lattice.

We start by optimizing the growth conditions of the nanodiamonds to achieve simultaneously good emission properties as well as well faceted nanodiamond crystals. Figure 7.2 shows the growth of nanodiamonds on the GeO_2 dopant coating. Growth under 50 Torr (Figure 7.2a) results in a low quality nanodiamonds with dopant residue. Both 60 and 70 Torr (Figure 7.2b, c) growths on the other hand show single crystal nanodiamonds. The higher pressure results in more nanodiamonds being etched as evidenced by the lower density of the remaining crystals. Finally, 80

Torr growth (Figure 7.2d) results in a very low concentration of the nanodiamonds due to large anisotropically etched sapphire substrates.

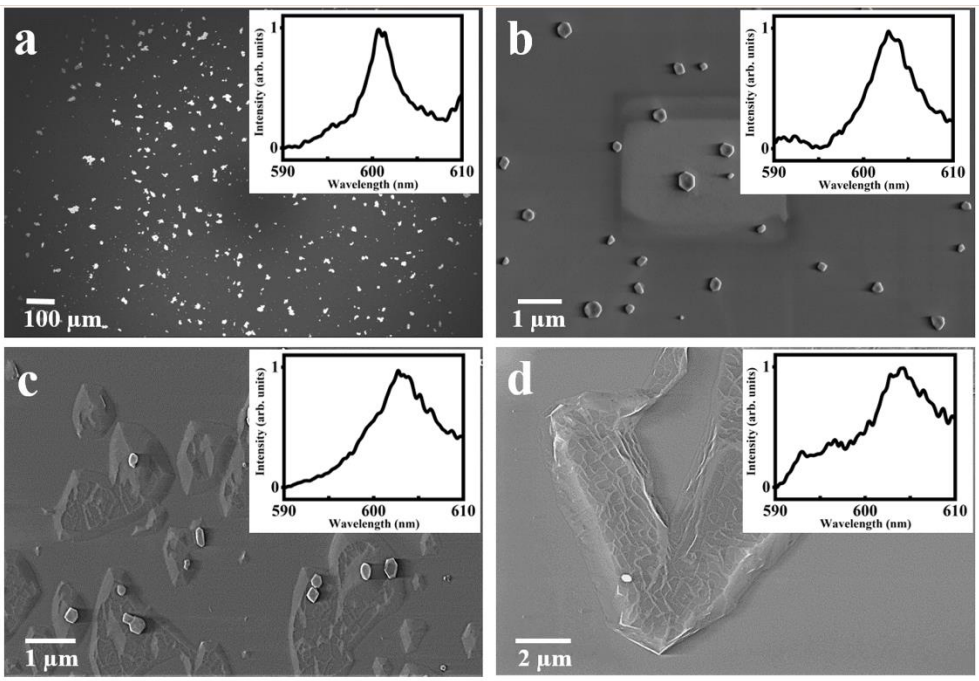

Figure 7.2. Diamond growth quality for germanium doped nanodiamonds grown at 50 (a ,scale bar 100 µm), 60 (b ,scale bar 1 µm) , 70 (c ,scale bar 1 µm) and 80 Torr (d ,scale bar 1 µm). Inset, corresponding PL spectra with clear ZPL at ~ 601.0 nm a), 603.1 nm b), 603.1 nm c), and 603.9 nm d) corresponding to GeV^- color center.

Photoluminescence (PL) spectra were collected using a continuous wave 532 nm laser (Gem 532, Laser Quantum Ltd.) for excitation and scanning directed through a Glan-Taylor polarizer (Thorlabs Inc.) and a half waveplate. The focus on the sample was achieved through a high numerical aperture (NA = 0.9) objective lens and the scanning was performed using an X–Ypiezo scanning mirror (FSM-300). Photoluminescence (PL) spectra from each sample are shown as an inset of each growth round. In all samples, there is clear evidence of the GeV^- signal as shown by the zero phonon lines (ZPL) at 601.0 nm, 603.1 nm, 603.1 nm and 603.9 nm in each inset respectively. The nanodiamonds grown under the lowest pressure (50 Torr) exhibit high background luminescence, presumably due to polycrystalline diamond

and dopant related noise. The other growths show a comparably little background, with the nanodiamonds grown at 70 Torr showing the sharpest GeV related emission. Given these results, subsequent growths with tin and germanium dopant coatings were performed at 60 and 70 Torr pressures pressures to maximise diamond quality while also maintaining spectral clarity. The quality of nanodiamonds after the growth has been determined by Raman spectroscopy to indicate the sp^3 orientation of diamond using 633 nm HeNe laser obtaining the Raman peak at ~1333.7 cm^{-1} with FWHM of 12.9 nm. We observed the difference in diamond growth quality at higher pressures, the typical diamond Raman peak at 1333 cm^{-1} is clearly present in the 70 Torr growth. The growth condition at 50 Torr does not allow for an ideal single crystal growth, the induced polycrystalline growth limits the diamond quality.

Next, we overgrow a single crystal diamond membrane. After the growth, membranes were all flipped and thinned to remove the original template, leaving behind a pristine, un-implanted diamond membrane doped with the color center of choice. The fabrication of high quality diamond membranes is important for further fabrication of scalable photonic devices such as optical cavities [161, 254]. The quality of the membrane was determined by Raman spectroscopy showing a peak at ~1331.6 cm^{-1} with FWHM of 3.7 nm (Figure 7.3 a). To solidify this claim, Raman spectroscopy was performed using a Renishaw inVia Raman spectrometer system and a 17 mW at 633 nm laser.

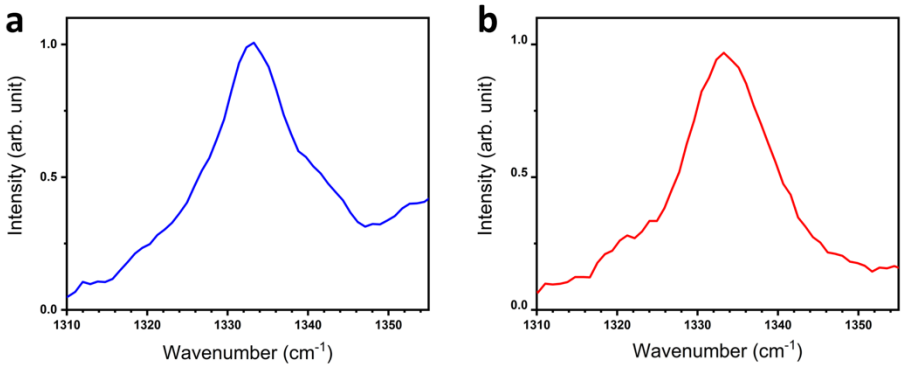

Figure 7.3. Raman spectra of nanodiamonds grown at 70 Torr with germanium a) and tin precursors b). Raman peaks at ~1333 cm^{-1} with FWHM of ~ 12 nm are measured.

The Raman data was collected from nanodiamonds grown at 70 Torr as shown in figure S1, as well as membranes grown in the presence of Germanium and Tin precursors as shown in Figure 7.3b. The quality of diamond growth is represented by the emission peak at wavenumber ~ 1333 cm^{-1} for NDs and ~ 1332 cm^{-1} for diamond membranes.

After the promising results obtained with GeO_2, a similar approach was implemented with Sn related oxide. Note, however, that the melting point of the SnO_2 is 1630°C, higher than the typical temperature of ~1000°C in the vicinity of the growing diamond within the MPCVD reactor. To circumvent this issue, we added $SnCl_2$ to the original dopant coating. The melting point of the $SnCl_2$ is much lower, ~ 250°C. The mixing of the tin chloride and tin oxide seems to modify the melting temperature of the combined layer closer to 1000°C, but the detailed mechanism should be explored in further studies.

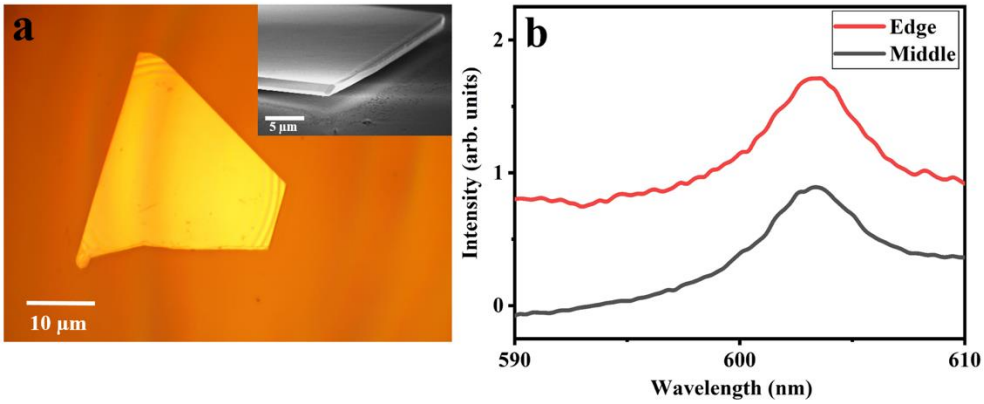

Figure 7.4. a) Optical image of the membrane after 10 min growth showing a smooth, high quality surface. Inset shows an SEM image of the membrane. b) Room temperature PL spectra comparison between edge and center of membrane (offset for clarity), with the ZPL centered at ~ 603.2 nm corresponding to the GeV^- emitters.

The successful fabrication of nanodiamonds and membranes containing SnV^- emitters is shown in Figure 7.4 and Figure 7.5, respectively. A typical emission of the SnV^- with a ZPL at ~ 620 nm is observed for both nanodiamonds and the single crystal

diamond membrane. Figure 7.5a and b highlights the highly dispersed growth of the nanodiamonds. Note that despite the growth occurring on a $SnO_2/SnCl_2$ film, the final distribution of the nanodiamonds and their high crystallinity (evident by the clearly visible facets) is maintained. Figure 7.5c shows the confocal map recorded with a 532 nm excitation source that shows most nanodiamonds host optically active defects and Figure 7.5d shows an example of three spectra with a strong emission at 620 nm, corresponding to SnV^-. Note that the confocal map area does not correspond to the SEM area in Figure 7.5a.

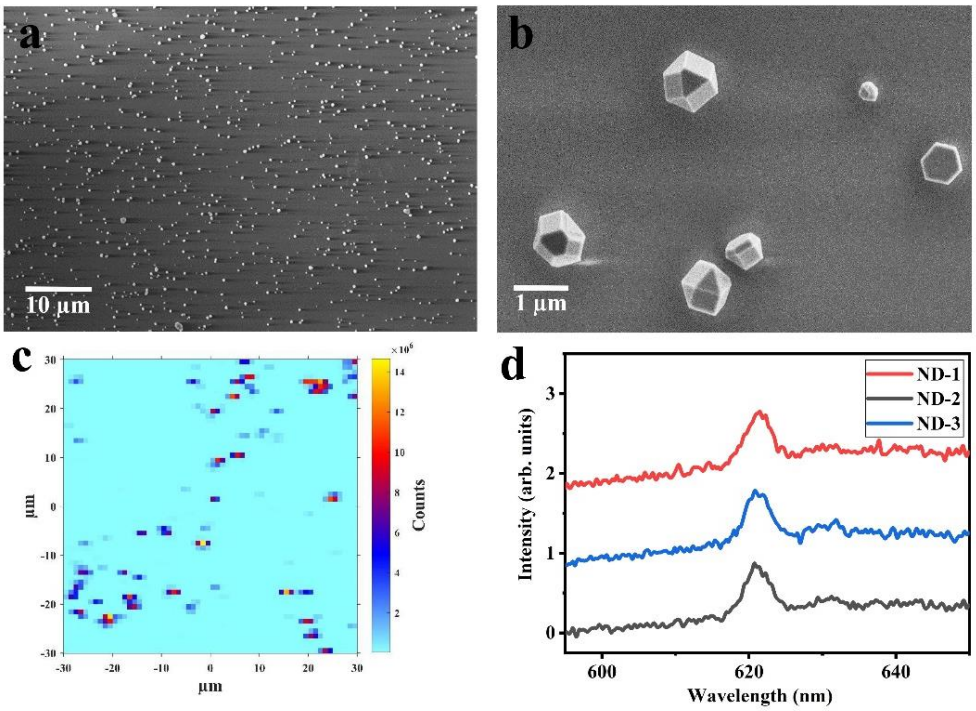

Figure 7.5. a) SEM images of the nanodiamonds after 10 min growth showing uniform distribution on the sapphire substrate. b) SEM image with high magnification shows the high quality diamond growth. c) Confocal PL map of the diamonds. d) Room temperature PL spectra of the NDs (offset for clarity), with peaks of ND-1,2 and 3 centered at 621.1 nm, 621.2 nm and 621.1 nm respectively corresponding to the ZPL of the SnV^-.

Given the ability to grow high quality nanodiamonds with visible crystal planes, we employed the same conditions to grow over a large single crystal diamond

membrane. The results are summarized in Figure 7.6. Similarly to the process used to generate the GeV^- color centers, the membranes were first overgrown, then flipped and thinned to remove the original material, leaving behind a pristine membrane with the desired dopant (SnV^- in this particular case).

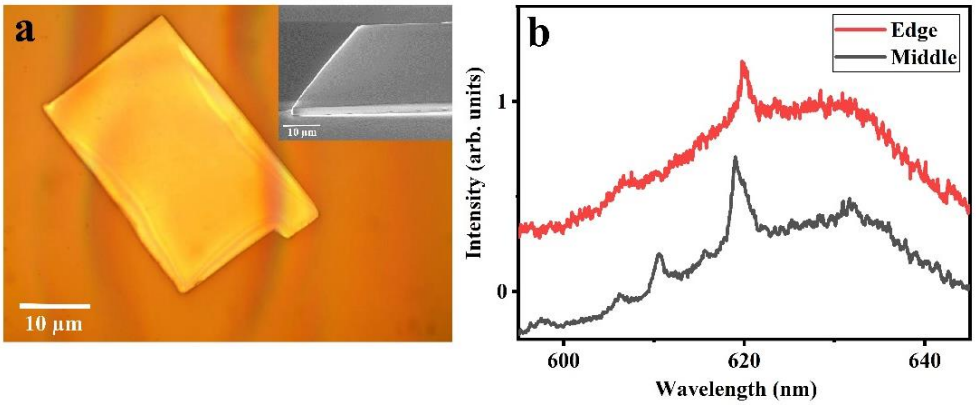

Figure 7.6. a) Optical images of the membrane after 10 min growth. Inset shows SEM image of the membrane with a smooth, high quality surface. The scale bar is 10 µm. b) Room temperature PL spectra comparison between edge and center of membrane (offset for clarity), with the peak centered at ~ 620 nm (emitter on the edge of the membrane) and ~ 619.4 nm nm (emitter in the middle of the membrane) confirms the successful incorporation of SnV^- into the membrane.

The optical image of the membrane is shown in Figure 7.6a and the representative spectra recorded from the middle and the side of the membrane are shown in Figure 7.6b. A 620 nm emission peak on the edge and a 619 nm emission peak in the middle are clear signatures of the SnV^- center. Overall, this comparison demonstrates a similar incorporation throughout the membrane, emphasising the continuous optical profile of the overgrown color centers throughout the membrane. The overgrown material shown in the inset of Figure 7.6a, to demonstrate a smooth single crystal surface without the presence of crystal boundaries through the bulk material. In some locations, other peaks appeared (e.g., ~610 nm) but their origin is unknown and is unlikely to be related to Sn.

The Raman spectroscopy evidenced a peak at 1332.5 cm^{-1} with FWHM of 3.8 nm indicating the high quality of the membrane. Figure 7.7. shows the Raman spectroscopy on CVD overgrown diamond samples. These samples have undergone the thinning process, removing all damaged material, therefore the Raman data is collected from only overgrown material. The typical 1332 cm^{-1} emission peak associated with diamond is strongly present in both samples at ~1331.6 cm^{-1} with FWHM of ~ 3.7 nm (Figure 7.7 a and b).

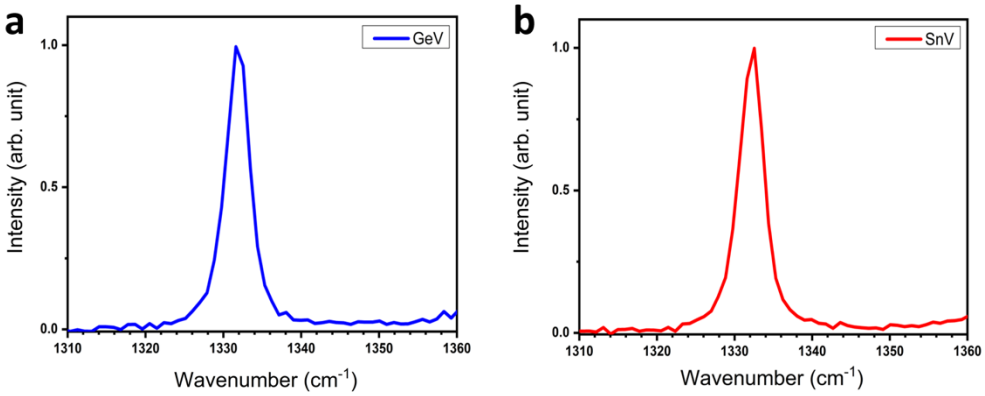

Figure 7.7. Raman data from diamond membranes grown with a) germanium and b) tin precursors. Both membranes show a strong Raman peak at ~1332 cm^{-1} indicating a high quality diamond growth.

7.4 Conclusion

In summary, diamond doping by means of MPCVD techniques was performed to fabricate selected group IV color centers, namely the GeV^- and the SnV^- in both nanodiamonds and single crystal diamond membranes. Our experimental investigation of the existing methods to fabricate GeV^- and SnV^- into diamond using metallic oxide and chloride suspensions lead to the development of a reliable doping procedure by matching the melting temperature of the precursors to the temperature reached during the diamond growth using MPCVD. We ascertained that

despite the introduction of inorganic precursors, adequate conditions for high quality diamond growth is feasible. Our results pave the way for broad adaptation of this method, extending it to dope diamond with other color centers beyond the group IV elements.

Chapter 8 Plasmonic enhanced photoluminescence from SiV^- and GeV^- emitters embedded in single crystal diamond membranes

This chapter reports the results of the weak coupling of SiV^- and GeV^- emitters embedded in nanoscale single crystal diamond membranes and silver nanodisk plasmonic arrays on fused silica. The project was conceived by Igor Aharonovich and Teri Odom. The plasmonic arrays were fabricated by Teri Odom. Fabrication of diamond membranes and doping were performed by Aleksandra T. Trycz. Characterization of devices were performed by Kerem Bray and Blake Regan. Coupling experiments and analysis were performed by Aleksandra T. Trycz. The manuscript was written by Aleksandra T. Trycz and Sejeong C. Kim with contribution of all the authors.

8.1 Abstract

High quality nanoscale SCD membranes hosting stable, optically active defects are emerging as an important building block for scalable quantum photonics. The recent improvements in deterministic doping of thin diamond membranes and development of robust and mature nanofabrication protocols led to the availability of cost effective methods of engineering high quality color centers possessing a wide range of emission properties. Nevertheless, the realization of integrated nanophotonic devices requires further processing of photoluminescent emission and coupling of these emitters to resonators and optical cavities for signal enhancement. Here, we describe for the first time an efficient coupling of two high quality, 300 nm thick single crystal diamond membranes containing SiV^- and GeV^- respectively to silver nanodisk arrays on fused silica to enhance the photoluminescence emission

from these color centers. The coupling is achieved by bringing the emitters very close to the plasmonic structures assuring a controllable emitter-mode distance in z-direction.

Our results prove that the resonant coupling of emitted light with plasmonic lattices can be achieved enabling a wide range of future applications for flat hybrid photonic-plasmonic systems based on solid state emitters.

8.2 Introduction

Colour centers in diamonds are an established platform for solid-state quantum photonics [72, 124, 205, 245, 246, 248] as RT stable, single photon emitters, therefore are valued candidates for studies of light-matter interaction at the nanoscale. In recent years, a particular scrutiny has been put on the group IV elemental complexes, including the SiV^-, GeV^-, SnV^- and PbV^-, in order to exploit their typical narrowband, bright, and photostable emission with optical spin readout at cryogenic temperatures [20, 104, 105, 139, 142, 233].

Among these group IV colour centers, SiV^- attracted great attention for its relative ease of fabrication [125, 233, 247], and has demonstrated its capabilities in optical circuitry, for enabling photon-photon interactions, and for two photon interference experiments [1, 247]. Meanwhile, GeV^- has recently demonstrated unique advantages over SiV-, including improved photostability [147, 251], high quantum efficiency, and a large splitting in the ground state which enables superior spin manipulation [124]. To further enhance the brightness of group IV emitters, we adopted an approach which consisted in coupling the selected emitters to the plasmonic resonators combining desirable plasmonic and photonic attributes. Thanks to recent and rapid discoveries in nanofabrication technologies there is a wide range of noble-metal structures with exceptional optical properties to choose from according to the specific requirements [255-258].

Recent improvements in engineering techniques of plasmonic structures offer a practical and scalable approach to fabricate large scale arrays of plasmonic nanostructures [255, 259]. A localized surface plasmon is created in a metal nanostructure which enables confining light in a small mode volume, hence increasing light-matter interaction. The plasmonic resonance can be further tuned and enhanced by using an array of nanostructures [258]. Silver nanostructures are typically chosen for the applications in the visible wavelength for their relatively low loss in this wavelength range compared to other novel metals [257].

Here, we demonstrate photoluminescence enhancement of colour centers in diamond membranes by silver plasmonic nanodisk array. Diamond membranes that contain either SiV^- or GeV^- are transferred onto a plasmonic substrate which contains Ag nanodisks on fused silica substrates. Two plasmonic samples are used in the experiment: one has 500 nm spacing with plasmonic lattice resonance at 740 nm and the other lattice is a 400 nm spaced Ag nanodisks with plasmonic resonance at 590 nm. This study shows the coupling of colour centers with silver plasmonic resonators and an open way to explore a resonant behavior of other emitters beyond the group IV. Our method of using thin diamond membranes and scalable plasmonic nanostructures is fully compatible with scalable photonic devices.

8.3 Results and Discussion

A schematic of the system consisting of a silver nanodisk array with diamond membrane transferred on top is shown in Figure 8.1a. The thin, diamond membrane enables transfer onto any substrate, as well as coupling to plasmonic nanostructures by placing emitters in the close vicinity of plasmonic resonances. Figure 8.1b shows the scanning electron microscopy (SEM) image of the plasmonic lattice with silver nanodisks arrays fabricated by electron beam lithography (EBL) on a fused silica substrate. The inset in Figure 8.1b is a picture of the plasmonic device employed in

the experiment. Two plasmonic array samples are prepared having a spacing of 400 nm and 500 nm to match the emission wavelength from GeV^- and SiV^-, respectively.

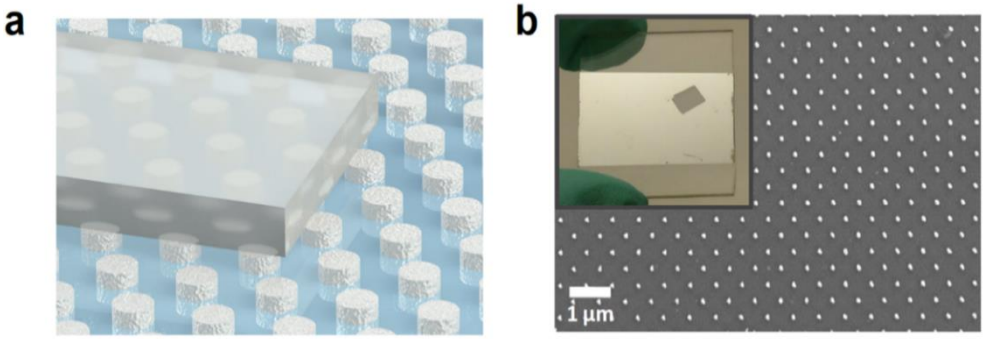

Figure 8.1. a) Schematic illustration of metal nanodisk array on fused silica with a thin single crystal diamond membrane on top. b) SEM image of the plasmonic lattice consisting of Ag nanodisks spaced 500 nm on fused silica. The inset shows the photograph of the plasmonic device employed in the experiment.

Next, 300 nm thick, high quality single crystal diamond (SCD) membranes containing either SiV^- or GeV^- emitters are fabricated. Creating these optically active color centers without degrading the diamond structure and photophysical properties is a challenging task using conventional methods. So far, various methods to embed color centers in diamonds have been explored including ion implantation [22, 104, 105, 151, 252], high pressure high temperature (HPHT) [141, 209, 210] methods, and chemical vapor deposition (CVD) growth. However, the implantation and HPHT methods induce a built-in strain in diamond lattice resulting in degradation of optical and photophysical properties, and HPHT is limited to the applications that only use bulk and nanoparticles. In this work, we circumvent these issues by using a bottom-up overgrowth method by means of MPCVD chamber to create SiV^- and GeV^- color centers in thin diamond membranes. The technique offers a simple method to grow high quality, homoepitaxial diamond layers with flexibility in controlling dopant precursors [161, 166, 260].

Figure 8.2a shows a high quality, CVD overgrown SCD membrane ~ 2.7 µm thick after the MPCVD overgrowth, while the inset shows a zoomed SEM image of the plasmonic device with nanodisk array spacing of 500 nm. Diamond membranes are deployed in this experiment as they embody optically isolated, standalone, nanoscalable high quality devices that can host myriad of different color centers [166]. Moreover, these membranes can be thinned to desired thickness and transferred and positioned onto a substrate of choice which in our case was a noble-metal nanodisk array. In detail, diamond membranes were fabricated from a type IIa (100) single crystal diamond bulk (Element six) by implantation with He^+ ions followed by high vacuum annealing.

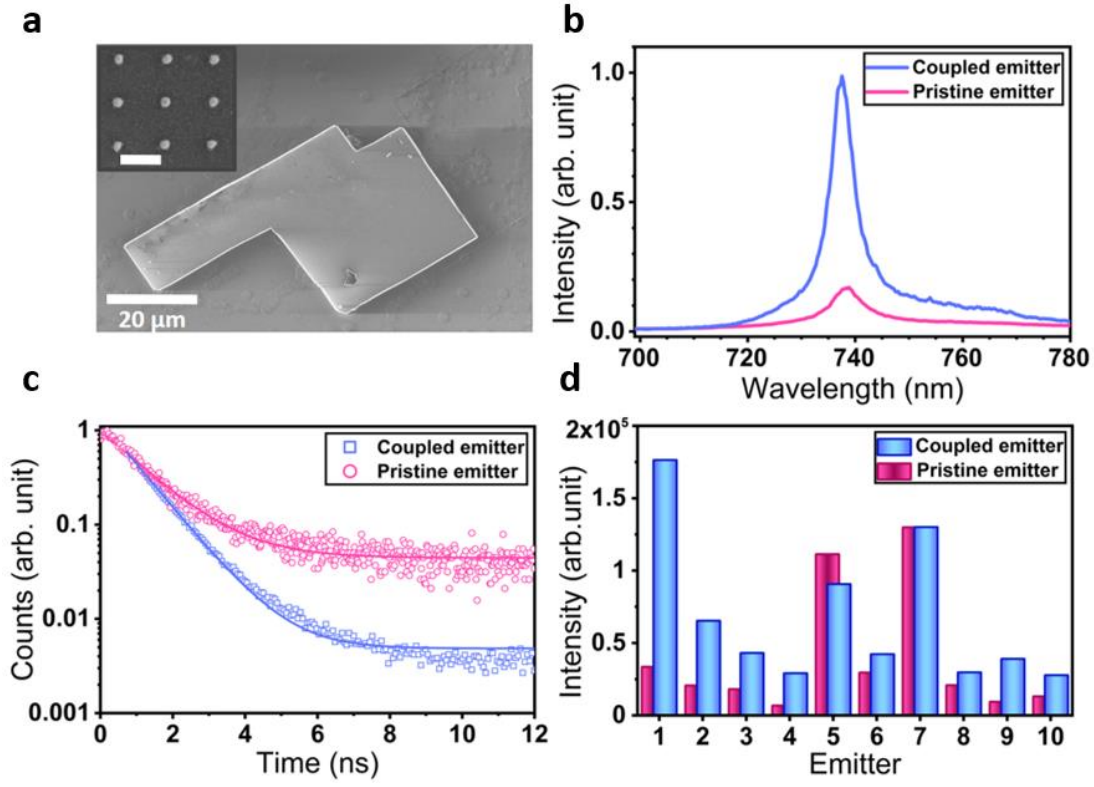

Figure 8.2. Coupling between SiV^- emitter in the diamond membrane and a silver nanodisk array on fused silica with a resonance frequency that lies at ~ 740 nm. a) SEM image of single crystal diamond membrane after 8 min of MPCVD overgrowth on silicon dioxide substrate. The thickness of the membrane after growth is ~ 2.7 µm. The inset shows the SEM image of the plasmonic array with a scale bar of 500 nm. b) PL spectrum of a pristine (pink line) and coupled (blue line) SiV^- emitter. c) Typical time-resolved PL measurement from the pristine (pink circles) and coupled systems (blue squares). Solid lines are exponential fits. The

measured lifetime values are τ_P = 1.18 ns and τ_C = 0.93 ns for the pristine and coupled emitter respectively. d) Comparison of PL intensity for 10 pristine (pink bars) and coupled (blue bars) SiV^- emitters. A 532 nm continuous- wave laser was used for PL measurements.

Electrochemical etching was performed to detach from the bulk 1.7 µm thick membranes followed by piranha cleaning. The transfer was performed using a liquid droplet of ultra pure water (MilliQ) to move the membranes onto the desired substrate. In our case, a silicon substrate with 300 nm thermal oxide layer is used for SiV^- incorporation and a sapphire substrate for GeV^- incorporation. In the next step, the membranes were then overgrown in the MPCVD chamber for 8 minutes using methane and hydrogen gases as the precursors obtaining a smooth, homoepitaxial diamond layer containing the ensemble of desired emitters. Such doping methods were optimized to obtain a homogeneous distribution of embedded emitters in the membranes. After the growth, membranes were flipped and etched down to ~ 300 nm by means of ICP-RIE employing argon, oxygen and SF_6 gases for 18 minutes to reach the required thickness. A flipped membrane brings an additional benefit of placing color centers close to the bottom surface of the membrane, where the plasmonic lattice will be integrated, assuring a controllable emitter-mode distance in z-direction.

To compare the emission from the color centers in the presence of plasmonic resonance, the emitters are characterized both before and after the diamond membrane transfer on to Ag plasmonic arrays. For photoluminescent (PL) characterization, we used a continuous wave 532 nm laser (Gem 532, Laser Quantum) with 0.2 mW. A 100 x objective lens with a numerical aperture of 0.7 is used to focus the excitation laser and to collect the signal from the sample. All experiments are conducted at room temperature in ambient conditions. The experimental results are presented in Figure 8.2b showing a room temperature PL measurement of pristine emitter (pink curve), and the same emitter coupled to the plasmonic nanodisk array (blue curve) of the thin (～300 nm) diamond membrane showing a typical zero phonon line (ZPL) at ~738 nm for SiV^- emitter. Under the same excitation power of 0.2 mW, the PL is enhanced by a factor of ~ 4 when compared

the peak intensity value at 738 nm. For more quantitative analysis of the enhancement, we recorded lifetimes of the emitters before and after the coupling using a 633 nm pulsed laser (0.1 mW) and observed a reduction in the lifetime when the sample is placed on the plasmonic lattice as shown in Figure 8.2c. Lifetime results are fitted using an exponential fitting function and plotted in solid lines respectively. The measured lifetime values are τ_P = 1.18 ns and τ_C = 0.93 ns for the pristine (pink circles) and coupled (blue squares) emitters respectively. To compare the values of PL enhancement and lifetime reduction of SiV- emitters at different positions, we performed a line scan of the membrane starting from the edge towards the center, acquiring the signal approximately every 2 µm and observed a high density and homogeneous distribution of color centers across the membrane. Figure 8.2d shows a comparison data of PL intensity for 10 pristine (pink bars) and coupled (blue bars) SiV- emitters demonstrating the enhancement in photoluminescence intensity where peak intensities of ZPL of pristine (pink bars) and coupled (blue bars) emitters are shown. Overall, nine out of ten emitters were successfully enhanced in intensity by plasmonic coupling increasing their emission intensity between ~1.5 - 4 fold, along with a lifetime reduction for the same 10 emitters shown in Figure 8.3.

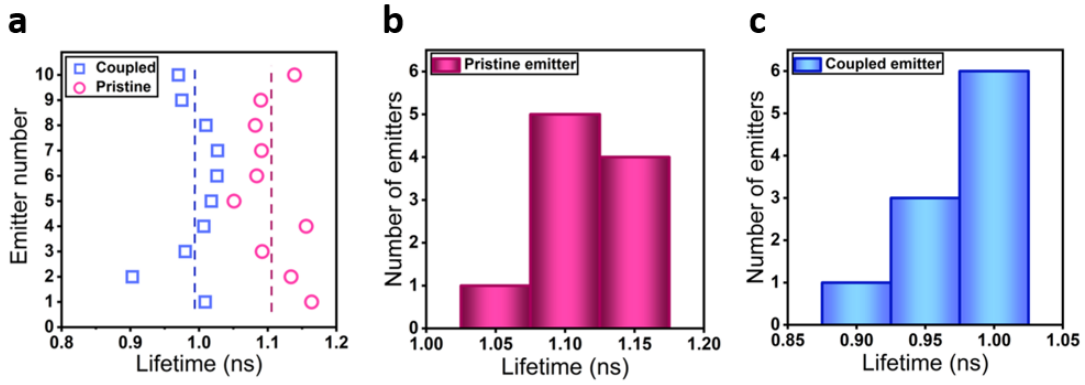

Figure 8.3. a) Comparison of the measured lifetime values for ten pristine (pink circles) and coupled (blue squares) SiV- emitters. We observe a small but consistent reduction in the lifetime when the sample is placed on the plasmonic nanodisk array evidenced by the mean value represented with dashed lines for pristine (pink line with the mean value of ~1.1 ns) and coupled (blue line with mean value of ~ 1 ns) color centers. b) Histogram of the lifetime

measurements for 10 pristine (pink bars) and c) coupled (blue bars) emitters. A 633 nm pulsed laser with a repetition rate of 10 MHz and 100 ps pulse width was used.

Such increased PL intensity is due to the coupling with plasmonic arrays. The lifetime reduction together with PL enhancement shows the increased spontaneous emission rate of emitters induced by the plasmonic resonance. PL enhancement is also attributed to the excitation and collection efficiency enhancement of plasmonic resonator. The variations in lifetime reduction and PL enhancement are due to the distance variation between the emitter and the plasmonic mode.

In the next step, we performed an analogous experiment employing a membrane containing another group IV element - germanium and coupled it with the second plasmonic lattice with resonance at λ = 590 nm. The differences between employing SiV^- and GeV^- are multiple. GeV^- presents a strong and sharp luminescence band with ZPL at ~ 602 nm, lifetime in order of 1.4 – 5.5 ns and can be used as a SPS at room temperature. Furthermore, GeV^- possesses larger energy band gap compared to silicon which reduces the phonon split mixing and increases the spin coherence time [139]. For the excitation of germanium emitters, we used the same confocal setup described previously with 405 nm (CW, 1 mW) laser. Figure 8.4a shows a SEM image of thinned diamond membrane containing GeV^-. In Figure 8.4b, we report a RT PL spectrum of the pristine emitter (pink curve) and the same emitter coupled to the plasmonic nanodisk array (blue curve) of the thin (～300 nm) diamond membrane showing an enhancement ~ 3.3 times of the signal in coupled emitter with ZPL at 603 nm.

For further analysis of the enhancement, we recorded lifetime measurement of the emitters before and after the transfer onto a plasmonic device using 405 nm pulsed laser with a rotated 630 nm band pass filter at 0.5 mW of power and the experimental results of the obtained lifetime are fitted using a double exponential fitting function and plotted in solid lines respectively for pristine (pink line) and coupled emitter (blue line). The lifetime plots are shown in Figure 8.4c.

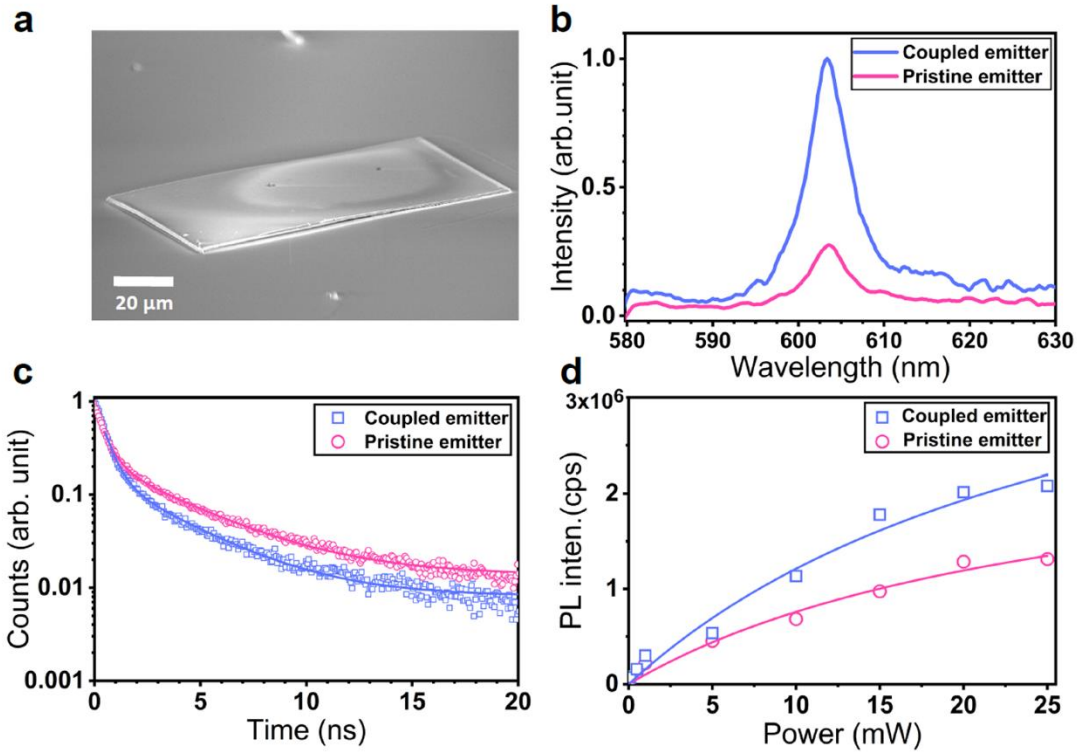

Figure 8.4. Coupling between GeV^- emitter in diamond membrane and a silver nanodisk array on fused silica with resonance frequency that lies at ~590 nm. a) SEM image of single crystal diamond membrane after 18 min of ICP-RIE etching. Thickness of the membrane after thinning is ~ 300 nm. b) PL spectra of a pristine (pink curve) and coupled (blue curve) GeV^- emitter. c) Time-resolved PL measurements from the pristine (pink circles) and coupled systems (blue squares). Solid lines are double exponential fits. The measured lifetime values are τ_P = 3.70 ns and τ_C = 3.27 ns for the pristine and coupled emitter respectively. A 405 nm continuous- wave laser was used in b) and 405 nm pulsed laser (0.5 mW) with a rotated 630 nm band pass filter was used in c). d) Fluorescence saturation curves obtained from the pristine (pink open circles) and coupled (blue open squares) systems. Pink and blue solid lines are fits obtained from the eq. $I_{sat} = I_{max}xP/(P + P_{sat})$ where I_{max} and P_{sat} are the maximum emission rate and excitation power at which saturation is reached, respectively. The value of 25 mW was the maximum for our system and the saturation condition was not reached.

The measured lifetime values are τ_P = 3.70 ns and τ_C = 3.27 ns for the pristine and coupled emitter respectively. Fluorescence saturation curves obtained from the pristine (pink open circles) and coupled (blue open squares) systems are shown in

Figure 8.d. Pink and blue solid lines are fits obtained from the eq. $I_{sat} = I_{max}xP/(P + P_{sat})$ where I_{max} and P_{sat} are the maximum emission rate and excitation power at which saturation is reached, respectively. The value of 25 mW was the maximum for our system and the saturation condition was not reached. In the case of germanium color centers coupled to the plasmonic array, we measured 6 emitters and obtained a considerable enhancement of the PL signal between ~ 1.6 and 4.1 and a reduction in lifetime between 0.4 - 1 ns in the pristine and coupled emitters, respectively.

8.4 Conclusion

In summary, we demonstrated for the first time the feasibility to couple SiV^- and GeV^- color centers embedded in nanoscale, high-quality SCD diamond membranes to plasmonic silver nanodisk arrays and reached a consistent enhancement in PL signal of a factor of ~ 1.5 - 4 associated with a lifetime reduction for both emitters. Our results underline the importance of correct matching of the resonant frequency of plasmonic devices with the wavelength of the emitters to reach the maximum possible of the enhancement. Successful employment of emitters embedded in diamond membranes leaves an open way for future improvements of this method extending it to study the behaviour of other color centers beyond the group IV elements and to combine planar optics with 2D materials and plasmonic resonators into a hybrid plasmonic-photonic nanodevices. We believe our results will accelerate the integration of solid-state emitters embedded in thin diamond membranes with scalable photonic devices to improve the engineering techniques.

Chapter 9 Summary and Outlook

In this chapter, the main conclusions drawn from the thesis are summarized and reviewed, followed by the outlook and future prospects of the project

9.1 Summary and conclusions

This work featured an extensive experimental investigation of various solid precursors for doping of NDs and nanoscale SCD membranes with group IV elements. SiV, GeV, and SnV emitters have been successfully fabricated using a bottom up approach by means of MPCVD homoepitaxial overgrowth. Several procedures that lead to the development of robust and reliable fabrication protocols have been described in detail.

Germanium vacancies have been initially engineered combining metallic and oxide powder and subsequently metallic and oxide suspensions directly drop cast on the sample to grow. Another method for incorporation of germanium and tin consisted of the combination of metallic oxide and chloride suspensions and by matching the melting temperature of the precursors to the growth temperature in MPCVD chamber obtaining high quality, smooth diamond membranes with uniform distribution of desired, bright emitters and highly faceted nanodiamond crystals.

The results presented in this thesis further extend the available procedures to directly dope diamond by means of MPCVD and other color centers beyond the group IV elements might benefit from the adaptation of this method. The relevant findings and fabrication protocols are summarized below followed by main conclusions and outlook for further development and potential future applications.

The first part of this thesis details the importance of diamond as a remarkable material for fabrication of nanodevices and the discovery of stable SPEs operating at

room temperature hosted in diamond paved the way towards its implementation for quantum technological applications.

The experimental section describes the path that led to the development of the protocols for incorporation of group IV emitters.

The first approach was to generate GeVs in diamond membranes and consisted of use of only metallic germanium. After a standard MPCVD overgrowth, the surface of the membrane was roughened with many secondary nucleation spots and no germanium incorporation was observed in confocal PL measurements.

In the second approach, a germanium oxide precursor was used and the overgrowth resulted in smooth diamond membranes. However, the incorporation of germanium was relatively low (indicated by the low intensity of GeV^- emission), due to the slow release of the Ge atoms from the oxide during the growth. This method might be explored in the future to incorporate single GeV defects.

Next the combination of solid Ge precursors was employed to incorporate germanium into the diamond lattice and to increase the amount of germanium available during the growth. Resulting membranes were smooth and with bright characteristic GeV^- peaks at ~ 602 nm. With the combination of the precursors, oxide can passivate the metallic germanium, causing a longer and more consistent release of germanium ions into the plasma. Given the promising result of the GeV doping, characterization by taking PL spectra at random locations across the membrane displayed a homogeneous incorporation of GeV and the membranes were then employed for the fabrication of photonic resonators (microrings array with a 2.5 µm outer radius and 400 nm width rings) using an electron beam lithography patterning technique. Whispering gallery modes were found in most of the rings with average quality factor of Q ~ 500.

The next route towards the bottom up synthesis of single crystal diamond membranes containing GeV^- color centers is described as a combination of a direct dropcast of germanium dioxide solution in ethanol combined with metallic germanium precursors. These membranes resulted in uniform incorporation of

germanium and were further employed for engineering of photonic resonators such as microdisk cavities with quality factors of ~ 1500.

Next, MPCVD doping technique was improved to fabricate GeV^- and the SnV^- in both NDs and SCD membranes. Our experimental investigation using metallic oxide and chloride suspensions lead to the development of a reliable doping procedure. Inorganic salts were used to prepare the chemical precursors in a form of dopant coating that contained the required ions that were then incorporated into the growing diamond. We ascertained that despite inorganic precursors' introduction, adequate conditions for high quality diamond growth are feasible. The minute amount of dopant used (only 8 µL of 10 mg/mL solution) makes this both a safer and greener method for color center incorporation compared to the previous gas phase MPCVD methods without sacrificing the diamond quality.

The last chapter of the thesis describes an efficient coupling of two high quality, ~ 300 nm thick SCD membranes containing SiV^- and GeV^- emitters to their respective silver nanodisk arrays. The coupling is achieved by bringing the emitters very close to the plasmonic structures assuring a controllable emitter-mode distance in z-direction and an enhancement in PL signal of a factor of ~ 1.5 - 4 achieved associated with a lifetime reduction for both emitters. These results demonstrate that the resonant coupling of emitted light with plasmonic lattices is feasible and may be extended to study other color centers' behavior beyond the group IV elements combining planar optics with 2D materials and plasmonic resonators into a hybrid plasmonic-photonic nanodevices. These results will accelerate the integration of solid-state emitters hosted in thin diamond membranes with scalable photonic devices to further improve the engineering techniques.

9.2 Outlook and future directions

The studies presented in this thesis expand the available methods for doping diamond with stable SPEs, highlighting the advantages of a chemical vapor

deposition approach to color center fabrication. These protocols not only result to be simple, cost-effective, and flexible, but they also permit high quality homoepitaxial growth of diamond membranes and NDs. These platforms can be utilized as a source of emitters for a wide range of quantum photonic applications and advance the progress of diamond-based technologies.

Integration of solid-state emitters hosted in diamonds for a multitude of photonic applications is an object of extensive research around the world with more than 200 research groups working on the exploitation and application of its quantum properties. Therefore, diamond has gained a leading position as a material in quantum nanophotonics with a growing number of companies and start-ups projects developing technologies using diamond as a part of so called "4^{th} industrial revolution". For this reason, advancements in the reliable fabrication and deployment of these systems remains of paramount importance.

My work offers a relevant contribution to the scientific community presenting robust methods for the fabrication of essential diamond photonic components such as NDs and SCD diamond membranes to be deployed for a wide variety of potential applications based on color centers. Furthermore, these general methods can be expanded to other color centers of interest.

Despite the substantial improvements offered in this thesis, considerable work remains to be done to optimize the fabrication and quality of devices to enable these technologies to graduate from proof of principle demonstrations in the lab to scalable industrial solutions with future potential applications in everyday life.

At last, to justify the title of this thesis: "Bottom up Engineering of Group IV Color Centers in Nanodiamonds and Nanoscale Diamond Membranes by MPCVD" I would like to mention that a substantial effort has been also devoted to the fabrication of lead-related color centers by MPCVD following a similar procedure. For that purpose, several different lead compounds and their suspensions were employed, including lead (II) acetate $Pb(CH_3COO)_2$, lead (II)chloride $PbCl_2$, lead oxide PbO, Pb(II,IV) and sulphur in 3% HCl, $PbCl_2/Pb_xO_y$ (PbO, Pb_3O_4, Pb_2O_7) in water, most in different combinations. However, all experiments performed testing different conditions did

not produce any relevant lead incorporation reliably, leaving space for more research to be done to understand the exact mechanisms of lead-related color centers formation and activation during MPCVD growth, as PbV defects may have an important role in diamond-based quantum technologies going forward.

Bibliography

1. Sipahigil, A.; Evans, R. E.; Sukachev, D. D.; Burek, M. J.; Borregaard, J.; Bhaskar, M. K.; Nguyen, C. T.; Pacheco, J. L.; Atikian, H. A.; Meuwly, C., An integrated diamond nanophotonics platform for quantum-optical networks. *Science* **2016,** *354* (6314), 847-850.

2. Zaitsev, A. M., *Optical properties of diamond: a data handbook*. Springer Science & Business Media: 2013.

3. Spear, K. E.; Dismukes, J. P., *Synthetic diamond: emerging CVD science and technology*. John Wiley & Sons: 1994; Vol. 25.

4. Mildren, R.; Rabeau, J., *Optical engineering of diamond*. John Wiley & Sons: 2013.

5. Williams, R. J.; Kitzler, O.; Bai, Z.; Sarang, S.; Jasbeer, H.; McKay, A.; Antipov, S.; Sabella, A.; Lux, O.; Spence, D. J., High power diamond Raman lasers. *IEEE Journal of Selected Topics in Quantum Electronics* **2018,** *24* (5), 1-14.

6. Wolter, J.-H.; Voss, A.; Balmer, R.; Ricaud, S.; Antier, M.; Simon-Boisson, C.; Graf, T.; Ahmed, M. A. In *Symmetrically-Cooled Ti: Sapphire Thin-Disk Laser Using Single-Crystal Diamond Heat Spreaders*, Advanced Solid State Lasers, Optical Society of America: 2018; p AM6A. 14.

7. Broda, A.; Kuźmicz, A.; Rychlik, G.; Chmielewski, K.; Wójcik-Jedlińska, A.; Sankowska, I.; Gołaszewska-Malec, K.; Michalak, K.; Muszalski, J., Highly efficient heat extraction by double diamond heat-spreaders applied to a vertical external cavity surface-emitting laser. *Optical and Quantum Electronics* **2017,** *49* (9), 1-7.

8. Hoffmann, M. M.; Addleman, R. S.; Fulton, J. L., Short-pathlength, high-pressure flow cell for static and time-resolved infrared spectroscopy suitable for supercritical fluid solutions including hydrothermal systems. *Review of Scientific instruments* **2000,** *71* (3), 1552-1556.

9. Hirsch, K.; Holzapfel, W., Diamond anvil high-pressure cell for Raman spectroscopy. *Review of Scientific Instruments* **1981,** *52* (1), 52-55.

10. Granados, E.; Spence, D. J.; Mildren, R. P., Deep ultraviolet diamond Raman laser. *Optics express* **2011,** *19* (11), 10857-10863.

11. Latawiec, P.; Venkataraman, V.; Shams-Ansari, A.; Markham, M.; Lončar, M., Integrated diamond Raman laser pumped in the near-visible. *Optics Letters* **2018,** *43* (2), 318-321.

12. Reilly, S.; Savitski, V. G.; Liu, H.; Gu, E.; Dawson, M. D.; Kemp, A. J., Monolithic diamond Raman laser. *Optics Letters* **2015,** *40* (6), 930-933.

13. Sabella, A.; Piper, J. A.; Mildren, R. P., Diamond Raman laser with continuously tunable output from 3.38 to 3.80 µm. *Optics letters* **2014,** *39* (13), 4037-4040.

14. Castelletto, S.; Rosa, L.; Blackledge, J.; Al Abri, M. Z.; Boretti, A., Advances in diamond nanofabrication for ultrasensitive devices. *Microsystems & nanoengineering* **2017,** *3* (1), 1-16.

15. Hausmann, B. J.; Bulu, I.; Deotare, P.; McCutcheon, M.; Venkataraman, V.; Markham, M.; Twitchen, D.; Loncar, M., Integrated high-quality factor optical resonators in diamond. *Nano letters* **2013,** *13* (5), 1898-1902.

16. Lee, J. C.; Magyar, A. P.; Bracher, D. O.; Aharonovich, I.; Hu, E. L., Fabrication of thin diamond membranes for photonic applications. *Diamond and related materials* **2013,** *33*, 45-48.

17. Sovyk, D.; Ralchenko, V.; Tukmakov, K.; Shershulin, V.; Khomich, A.; Vorobyov, V.; Vlasov, I.; Akimov, A., Growth of CVD diamond nanopillars with imbedded silicon-vacancy color centers. *Optical Materials* **2016,** *61*, 25-29.

18. Schmidt, A.; Naydenov, B.; Jelezko, F.; Reithmaier, J. P.; Popov, C., Fabrication of highly dense arrays of nanocrystalline diamond nanopillars with integrated silicon-vacancy color centers during the growth. *Optical Materials Express* **2019,** *9* (12), 4545-4555.

19. Rugar, A. E.; Dory, C.; Sun, S.; Vučković, J. In *Optical Characterization of Single Tin-Vacancy Centers in Diamond Nanopillars*, CLEO: QELS_Fundamental Science, Optical Society of America: 2019; p FM4A. 2.

20. Rugar, A. E.; Dory, C.; Sun, S.; Vučković, J., Characterization of optical and spin properties of single tin-vacancy centers in diamond nanopillars. *Physical Review B* **2019,** *99* (20), 205417.

21. Marseglia, L.; Saha, K.; Ajoy, A.; Schröder, T.; Englund, D.; Jelezko, F.; Walsworth, R.; Pacheco, J. L.; Perry, D. L.; Bielejec, E. S., Bright nanowire single photon source based on SiV centers in diamond. *Optics express* **2018,** *26* (1), 80-89.

22. Trusheim, M. E.; Wan, N. H.; Chen, K. C.; Ciccarino, C. J.; Flick, J.; Sundararaman, R.; Malladi, G.; Bersin, E.; Walsh, M.; Lienhard, B., Lead-related quantum emitters in diamond. *Physical Review B* **2019,** *99* (7), 075430.

23. Huang, T.-Y.; Grote, R. R.; Mann, S. A.; Hopper, D. A.; Exarhos, A. L.; Lopez, G. G.; Kaighn, G. R.; Garnett, E. C.; Bassett, L. C., A monolithic immersion metalens for imaging solid-state quantum emitters. *Nature communications* **2019,** *10* (1), 1-8.

24. Marseglia, L.; Hadden, J.; Stanley-Clarke, A.; Harrison, J.; Patton, B.; Ho, Y.-L.; Naydenov, B.; Jelezko, F.; Meijer, J.; Dolan, P., Nanofabricated solid immersion lenses registered to single emitters in diamond. *Applied Physics Letters* **2011,** *98* (13), 133107.

25. Hadden, J.; Harrison, J.; Stanley-Clarke, A.; Marseglia, L.; Ho, Y.-L.; Patton, B.; O'Brien, J.; Rarity, J., Strongly enhanced photon collection from diamond defect centers under microfabricated integrated solid immersion lenses. *Applied Physics Letters* **2010,** *97* (24), 241901.

26. Purcell, E. M.; Torrey, H. C.; Pound, R. V., Resonance absorption by nuclear magnetic moments in a solid. *Physical review* **1946,** *69* (1-2), 37.

27. Su, C.-H.; Greentree, A. D.; Hollenberg, L. C., Towards a picosecond transform-limited nitrogen-vacancy based single photon source. *Optics Express* **2008,** *16* (9), 6240-6250.

28. Tao, Y.; Boss, J. M.; Moores, B.; Degen, C. L., Single-crystal diamond nanomechanical resonators with quality factors exceeding one million. *Nature communications* **2014,** *5* (1), 1-8.

29. MacQuarrie, E.; Otten, M.; Gray, S.; Fuchs, G., Cooling a mechanical resonator with nitrogen-vacancy centres using a room temperature excited state spin–strain interaction. *Nature communications* **2017,** *8* (1), 1-10.

30. Radtke, M.; Bernardi, E.; Slablab, A.; Nelz, R.; Neu, E., Nanoscale sensing based on nitrogen vacancy centers in single crystal diamond and nanodiamonds: achievements and challenges. *Nano Futures* **2019,** *3* (4), 042004.

31. Nelz, R.; Görlitz, J.; Herrmann, D.; Slablab, A.; Challier, M.; Radtke, M.; Fischer, M.; Gsell, S.; Schreck, M.; Becher, C., Toward wafer-scale diamond nano- and quantum technologies. *APL Materials* **2019,** *7* (1), 011108.

32. Fairchild, B. A.; Olivero, P.; Rubanov, S.; Greentree, A. D.; Waldermann, F.; Taylor, R. A.; Walmsley, I.; Smith, J. M.; Huntington, S.; Gibson, B. C., Fabrication of ultrathin single-crystal diamond membranes. *Advanced Materials* **2008,** *20* (24), 4793-4798.

33. Kurtsiefer, C.; Mayer, S.; Zarda, P.; Weinfurter, H., Stable solid-state source of single photons. *Physical review letters* **2000,** *85* (2), 290.

34. Markham, M.; Stacey, A.; Twitchen, D., Diamond components for quantum imaging, sensing and information processing devices. Google Patents: 2021.

35. Wrachtrup, J.; Jelezko, F.; Grotz, B.; McGuinness, L., Nitrogen-vacancy centers close to surfaces. *MRS bulletin* **2013,** *38* (2), 149.

36. Hong, S.; Grinolds, M. S.; Pham, L. M.; Le Sage, D.; Luan, L.; Walsworth, R. L.; Yacoby, A., Nanoscale magnetometry with NV centers in diamond. *MRS bulletin* **2013,** *38* (2), 155.

37. Rondin, L.; Tetienne, J.-P.; Hingant, T.; Roch, J.-F.; Maletinsky, P.; Jacques, V., Magnetometry with nitrogen-vacancy defects in diamond. *Reports on progress in physics* **2014,** *77* (5), 056503.

38. Schirhagl, R.; Chang, K.; Loretz, M.; Degen, C. L., Nitrogen-vacancy centers in diamond: nanoscale sensors for physics and biology. *Annual review of physical chemistry* **2014,** *65*, 83-105.

39. Casola, F.; van der Sar, T.; Yacoby, A., Probing condensed matter physics with magnetometry based on nitrogen-vacancy centres in diamond. *Nature Reviews Materials* **2018,** *3* (1), 1-13.

40. Sotoma, S.; Epperla, C. P.; Chang, H. C., Diamond nanothermometry. *ChemNanoMat* **2018,** *4* (1), 15-27.

41. Balasubramanian, G.; Chan, I.; Kolesov, R.; Al-Hmoud, M.; Tisler, J.; Shin, C.; Kim, C.; Wojcik, A.; Hemmer, P. R.; Krueger, A., Nanoscale imaging magnetometry with diamond spins under ambient conditions. *Nature* **2008,** *455* (7213), 648-651.

42. Wrachtrup, J.; Jelezko, F., Processing quantum information in diamond. *Journal of Physics: Condensed Matter* **2006,** *18* (21), S807.

43. Childress, L.; Hanson, R., Diamond NV centers for quantum computing and quantum networks. *MRS bulletin* **2013,** *38* (2), 134-138.

44. Nemoto, K.; Trupke, M.; Devitt, S. J.; Stephens, A. M.; Scharfenberger, B.; Buczak, K.; Nöbauer, T.; Everitt, M. S.; Schmiedmayer, J.; Munro, W. J., Photonic architecture for scalable quantum information processing in diamond. *Physical Review X* **2014,** *4* (3), 031022.

45. Prawer, S.; Aharonovich, I., *Quantum information processing with diamond: Principles and applications*. Elsevier: 2014.

46. Bhaskar, M. K.; Riedinger, R.; Machielse, B.; Levonian, D. S.; Nguyen, C. T.; Knall, E. N.; Park, H.; Englund, D.; Lončar, M.; Sukachev, D. D., Experimental demonstration of memory-enhanced quantum communication. *Nature* **2020,** *580* (7801), 60-64.

47. Su, C.-H.; Greentree, A. D.; Hollenberg, L. C., High-performance diamond-based single-photon sources for quantum communication. *Physical Review A* **2009,** *80* (5), 052308.

48. Wehner, S.; Elkouss, D.; Hanson, R., Quantum internet: A vision for the road ahead. *Science* **2018,** *362* (6412), eaam9288.

49. Nguyen, C.; Sukachev, D.; Bhaskar, M.; Machielse, B.; Levonian, D.; Knall, E.; Stroganov, P.; Chia, C.; Burek, M.; Riedinger, R., An integrated nanophotonic quantum register based on silicon-vacancy spins in diamond. *Physical Review B* **2019,** *100* (16), 165428.

50. Moody, G.; Sorger, V. J.; Juodawlkis, P. W.; Loh, W.; Sorace-Agaskar, C.; Davanco, M.; Chang, L.; Bowers, J. E.; Quack, N.; Galland, C., Roadmap on Integrated Quantum Photonics. *arXiv preprint arXiv:2102.03323* **2021**.

51. Pezzagna, S.; Meijer, J., Quantum computer based on color centers in diamond. *Applied Physics Reviews* **2021,** *8* (1), 011308.

52. Wan, N. H.; Lu, T.-J.; Chen, K. C.; Walsh, M. P.; Trusheim, M. E.; De Santis, L.; Bersin, E. A.; Harris, I. B.; Mouradian, S. L.; Christen, I. R., Large-scale integration of artificial atoms in hybrid photonic circuits. *Nature* **2020,** *583* (7815), 226-231.

53. Mi, S.; Kiss, M.; Graziosi, T.; Quack, N., Integrated photonic devices in single crystal diamond. *Journal of Physics: Photonics* **2020,** *2* (4), 042001.

54. Kalish, R., Ion-implantation in diamond and diamond films: doping, damage effects and their applications. *Applied surface science* **1997,** *117*, 558-569.

55. Dresselhaus, M.; Kalish, R.; Wieser, E., Ion Implantation in Diamond, Graphite and Related Materials. Springer-Verlag Berlin, Heidelberg, 1992, 202 Seiten, 108 Abbildungen, 5 Tabellen, Preis: DM 79.00, ISBN 3-540-54956-0—ISBN 0-387-54956-0. *Crystal Research and Technology* **1993,** *28* (3), 316-316.

56. Goss, J.; Briddon, P.; Rayson, M.; Sque, S.; Jones, R., Vacancy-impurity complexes and limitations for implantation doping of diamond. *Physical Review B* **2005,** *72* (3), 035214.

57. Jin-Ming, C.; Xiang-Dong, C.; Le-Le, F.; Zhao-Jun, G.; Chong-Wen, Z.; Fang-Wen, S.; Zheng-Fu, H.; Guang-Can, G., Generation of nitrogen-vacancy centers in diamond with ion implantation. *Chinese Physics Letters* **2012,** *29* (3), 036103.

58. Nshingabigwi, E.; Derry, T.; Naidoo, S.; Neethling, J.; Olivier, E.; O'Connell, J.; Levitt, C., Electron microscopy profiling of ion implantation damage in diamond: Dependence on fluence and annealing. *Diamond and related materials* **2014,** *49*, 1-8.

59. Sumiya, H.; Satoh, S., High-pressure synthesis of high-purity diamond crystal. *Diamond and Related Materials* **1996,** *5* (11), 1359-1365.

60. Sumiya, H.; Tamasaku, K., Large defect-free synthetic type IIa diamond crystals synthesized via high pressure and high temperature. *Japanese journal of applied physics* **2012,** *51* (9R), 090102.

61. Silva, F.; Achard, J.; Brinza, O.; Bonnin, X.; Hassouni, K.; Anthonis, A.; De Corte, K.; Barjon, J., High quality, large surface area, homoepitaxial MPACVD diamond growth. *Diamond and Related Materials* **2009,** *18* (5-8), 683-697.

62. Drumm, V.; Alves, A.; Fairchild, B.; Ganesan, K.; McCallum, J.; Jamieson, D.; Prawer, S.; Rubanov, S.; Kalish, R.; Feldman, L., Surface damage on diamond membranes fabricated by ion implantation and lift-off. *Applied Physics Letters* **2011,** *98* (23), 231904.

63. Fan, J.-W.; Cojocaru, I.; Becker, J.; Fedotov, I. V.; Alkahtani, M. H. A.; Alajlan, A.; Blakley, S.; Rezaee, M.; Lyamkina, A.; Palyanov, Y. N., Germanium-vacancy color center in diamond as a temperature sensor. *ACS Photonics* **2018,** *5* (3), 765-770.

64. Bundy, F.; Hall, H. T.; Strong, H.; Wentorf, R., Man-made diamonds. *nature* **1955,** *176* (4471), 51-55.

65. Applied Diamond Inc. http://usappliеddiamond.com/ (accessed on 17 February 2021).

66. AuDiaTec. https://audiatec.de/en/ (accessed on 17 February 2021).

67. Element 6 https://www.e6.com/ (accessed on 17 February 2021).

68. Pool, R. A new kind of quantum, So far, quantum computing has been ruled by ions and electrons, but does its future lie with photons? https://spie.org/news/photonics-focus/novdec-2020/a-new-kind-of-quantum?utm_id=mpfm1120e&spMailingID=6259114&spUserID=MTI2Mzg2NDQ0NzkwS0&spJobID=1140184218&spReportId=MTE0MDE4NDIxOAS2&SSO=1.

69. Balasubramanian, G.; Neumann, P.; Twitchen, D.; Markham, M.; Kolesov, R.; Mizuochi, N.; Isoya, J.; Achard, J.; Beck, J.; Tissler, J., Ultralong spin coherence time in isotopically engineered diamond. *Nature materials* **2009,** *8* (5), 383-387.

70. statista.com Market volume of lab-grown diamonds worldwide from 2009 to 2030,. https://www.statista.com/statistics/1078280/global-market-volume-of-lab-grown-diamonds/ (accessed on 22 February 2021).

71. Hausmann, B.; Choy, J.; Babinec, T.; Shields, B.; Bulu, I.; Lukin, M.; Lončar, M., Diamond nanophotonics and applications in quantum science and technology. Wiley Online Library: 2012.

72. Aharonovich, I.; Andrew, D., Greentree, and Steven Prawer. *Diamond photonics. Nat. Photonics* **2011,** *5* (7), 397-405.

73. Coe, S.; Sussmann, R., Optical, thermal and mechanical properties of CVD diamond. *Diamond and Related Materials* **2000,** *9* (9-10), 1726-1729.

74. Rath, P.; Khasminskaya, S.; Nebel, C.; Wild, C.; Pernice, W. H., Diamond-integrated optomechanical circuits. *Nature communications* **2013,** *4* (1), 1-9.

75. Twitchen, D.; Pickles, C.; Coe, S.; Sussmann, R.; Hall, C., Thermal conductivity measurements on CVD diamond. *Diamond and related materials* **2001,** *10* (3-7), 731-735.

76. Hausmann, B. J.; Shields, B.; Quan, Q.; Maletinsky, P.; McCutcheon, M.; Choy, J. T.; Babinec, T. M.; Kubanek, A.; Yacoby, A.; Lukin, M. D., Integrated diamond networks for quantum nanophotonics. *Nano letters* **2012,** *12* (3), 1578-1582.

77. Faraon, A.; Santori, C.; Huang, Z.; Acosta, V. M.; Beausoleil, R. G., Coupling of nitrogen-vacancy centers to photonic crystal cavities in monocrystalline diamond. *Physical review letters* **2012,** *109* (3), 033604.

78. Faraon, A.; Barclay, P. E.; Santori, C.; Fu, K.-M. C.; Beausoleil, R. G., Resonant enhancement of the zero-phonon emission from a colour centre in a diamond cavity. *Nature Photonics* **2011,** *5* (5), 301.

79. Nistor, P.; May, P., Diamond thin films: giving biomedical applications a new shine. *Journal of the royal society interface* **2017,** *14* (134), 20170382.

80. Aharonovich, I.; Neu, E., Diamond nanophotonics. *Advanced Optical Materials* **2014,** *2* (10), 911-928.

81. Peschel, G., Carbon-carbon bonds: hybridization. *Obtained online from: http://www. physik. fu-berlin. de/einrichtungen/ag/ag-reich/lehre/Archiv/ss2011/docs/Gina_Peschel-Handout. pdf, published on* **2011,** *5* (5).

82. Markham, M.; Dodson, J.; Scarsbrook, G.; Twitchen, D.; Balasubramanian, G.; Jelezko, F.; Wrachtrup, J., CVD diamond for spintronics. *Diamond and Related Materials* **2011,** *20* (2), 134-139.

83. Balmer, R.; Friel, I.; Woollard, S.; Wort, C.; Scarsbrook, G.; Coe, S.; El-Hajj, H.; Kaiser, A.; Denisenko, A.; Kohn, E., Unlocking diamond's potential as an electronic material. *Philosophical Transactions of the Royal Society A: Mathematical, Physical and Engineering Sciences* **2008,** *366* (1863), 251-265.

84. Dandy, D. S.; Coltrin, M. E., Diamond Thin Films Handbook. *Marcel Dekker, Inc* **2002**.

85. Balmer, R.; Brandon, J.; Clewes, S.; Dhillon, H.; Dodson, J.; Friel, I.; Inglis, P.; Madgwick, T.; Markham, M.; Mollart, T., Chemical vapour deposition synthetic diamond: materials, technology and applications. *Journal of Physics: Condensed Matter* **2009,** *21* (36), 364221.

86. Yamada, H.; Chayahara, A.; Mokuno, Y.; Tsubouchi, N.; Shikata, S.-i.; Fujimori, N., Developments of elemental technologies to produce inch-size single-crystal diamond wafers. *Diamond and Related materials* **2011,** *20* (4), 616-619.

87. May, P. W., CVD diamond: a new technology for the future? *Endeavour* **1995,** *19* (3), 101-106.

88. Aharonovich, I.; Castelletto, S.; Simpson, D.; Su, C.; Greentree, A.; Prawer, S., Diamond-based single-photon emitters. *Reports on progress in Physics* **2011,** *74* (7), 076501.

89. Aharonovich, I.; Englund, D.; Toth, M., Solid-state single-photon emitters. *Nature Photonics* **2016,** *10* (10), 631-641.

90. Asmussen, J.; Grotjohn, T. A.; Schuelke, T., Advances in plasma synthesis of UNCD films. In *Ultananocrystalline Diamond*, Elsevier: 2012; pp 53-83.

91. May, P. W.; Mankelevich, Y. A., From ultrananocrystalline diamond to single crystal diamond growth in hot filament and microwave plasma-enhanced CVD reactors: a unified model for growth rates and grain sizes. *The Journal of Physical Chemistry C* **2008,** *112* (32), 12432-12441.

92. Bundy, F.; Hall, H. T.; Strong, H.; Wentorfjun, R., Man-made diamonds. *nature* **1955,** *176* (4471), 51-55.

93. Bovenkerk, H.; Bundy, F.; Hall, H.; Strong, H.; Wentorf, R., Preparation of diamond. *Nature* **1959,** *184* (4693), 1094-1098.

94. Polyakov, S.; Denisov, V.; Kuzmin, N.; Kuznetsov, M.; Martyushov, S. Y.; Nosukhin, S.; Terentiev, S.; Blank, V., Characterization of top-quality type IIa synthetic diamonds for new X-ray optics. *Diamond and Related Materials* **2011,** *20* (5-6), 726-728.

95. Palyanov, Y. N.; Kupriyanov, I. N.; Borzdov, Y. M., High-pressure synthesis and characterization of Sn-doped single crystal diamond. *Carbon* **2019,** *143*, 769-775.

96. Jones, A. C.; Hitchman, M. L., Overview of chemical vapour deposition. *Chemical Vapour Deposition: Precursors, Processes and Applications* **2009,** *1*, 1-36.

97. Pezzagna, S.; Rogalla, D.; Wildanger, D.; Meijer, J.; Zaitsev, A., Creation and nature of optical centres in diamond for single-photon emission—overview and critical remarks. *New Journal of Physics* **2011,** *13* (3), 035024.

98. Wang, C.; Kurtsiefer, C.; Weinfurter, H.; Burchard, B., Single photon emission from SiV centres in diamond produced by ion implantation. *Journal of Physics B: Atomic, Molecular and Optical Physics* **2005,** *39* (1), 37.

99. Gaebel, T.; Popa, I.; Gruber, A.; Domhan, M.; Jelezko, F.; Wrachtrup, J., Stable single-photon source in the near infrared. *New Journal of Physics* **2004,** *6* (1), 98.

100. Beveratos, A.; Kühn, S.; Brouri, R.; Gacoin, T.; Poizat, J.-P.; Grangier, P., Room temperature stable single-photon source. *The European Physical Journal D-Atomic, Molecular, Optical and Plasma Physics* **2002,** *18* (2), 191-196.

101. Brown, R. H.; Twiss, R. Q., Correlation between photons in two coherent beams of light. *Nature* **1956,** *177* (4497), 27-29.

102. Ju, Z.; Lin, J.; Shen, S.; Wu, B.; Wu, E., Preparations and applications of single color centers in the diamond. *Advances in Physics: X* **2021,** *6* (1), 1858721.

103. Ekimov, E.; Lyapin, S.; Kondrin, M., Tin-vacancy color centers in micro-and polycrystalline diamonds synthesized at high pressures. *Diamond and Related Materials* **2018,** *87*, 223-227.

104. Ditalia Tchernij, S.; Lühmann, T.; Herzig, T.; Küpper, J.; Damin, A.; Santonocito, S.; Signorile, M.; Traina, P.; Moreva, E.; Celegato, F., Single-photon emitters in lead-implanted single-crystal diamond. *ACS Photonics* **2018,** *5* (12), 4864-4871.

105. Tchernij, S. D.; Herzig, T.; Forneris, J.; Kupper, J.; Pezzagna, S.; Traina, P.; Moreva, E.; Degiovanni, I.; Brida, G.; Skukan, N., Single-photon-emitting optical centers in diamond fabricated upon Sn implantation. *ACS photonics* **2017,** *4* (10), 2580-2586.

106. Wikipedia Atomic radii of the elements. https://en.wikipedia.org/wiki/Atomic_radii_of_the_elements_(data_page) (accessed on 17 February 2021).

107. Doherty, M. W.; Manson, N. B.; Delaney, P.; Jelezko, F.; Wrachtrup, J.; Hollenberg, L. C., The nitrogen-vacancy colour centre in diamond. *Physics Reports* **2013,** *528* (1), 1-45.

108. Mochalin, V. N.; Shenderova, O.; Ho, D.; Gogotsi, Y., The properties and applications of nanodiamonds. *Nature nanotechnology* **2012,** *7* (1), 11-23.

109. Smith, W.; Sorokin, P.; Gelles, I.; Lasher, G., Electron-spin resonance of nitrogen donors in diamond. *Physical Review* **1959,** *115* (6), 1546.

110. Clark, C.; Norris, C., Photoluminescence associated with the 1.673, 1.944 and 2.498 eV centres in diamond. *Journal of Physics C: Solid State Physics* **1971,** *4* (14), 2223.

111. Collins, A. T., The detection of colour-enhanced and synthetic gem diamonds by optical spectroscopy. *Diamond and related materials* **2003,** *12* (10-11), 1976-1983.

112. Iakoubovskii, K.; Adriaenssens, G., Optical transitions at the substitutional nitrogen centre in diamond. *Journal of Physics: Condensed Matter* **2000,** *12* (6), L77.

113. Hossain, F. M.; Doherty, M. W.; Wilson, H. F.; Hollenberg, L. C., Ab Initio electronic and optical properties of the N− V− center in diamond. *Physical review letters* **2008,** *101* (22), 226403.

114. Santori, C.; Tamarat, P.; Neumann, P.; Wrachtrup, J.; Fattal, D.; Beausoleil, R. G.; Rabeau, J.; Olivero, P.; Greentree, A. D.; Prawer, S., Coherent population trapping of single spins in diamond under optical excitation. *Physical review letters* **2006,** *97* (24), 247401.

115. Kayci, M.; Chang, H.-C.; Radenovic, A., Electron spin resonance of nitrogen-vacancy defects embedded in single nanodiamonds in an ABEL trap. *Nano letters* **2014,** *14* (9), 5335-5341.

116. Wilson, E. A.; Manson, N.; Wei, C., Perturbing an electromagnetic induced transparency within an inhomogeneously broadened transition. *Physical Review A* **2003,** *67* (2), 023812.

117. Wei, C.; Manson, N. B., Observation of the dynamic Stark effect on electromagnetically induced transparency. *Physical Review A* **1999,** *60* (3), 2540.

118. Chang, K.; Eichler, A.; Rhensius, J.; Lorenzelli, L.; Degen, C. L., Nanoscale imaging of current density with a single-spin magnetometer. *Nano letters* **2017,** *17* (4), 2367-2373.

119. Maurer, P. C.; Kucsko, G.; Latta, C.; Jiang, L.; Yao, N. Y.; Bennett, S. D.; Pastawski, F.; Hunger, D.; Chisholm, N.; Markham, M., Room-temperature quantum bit memory exceeding one second. *Science* **2012,** *336* (6086), 1283-1286.

120. Bernien, H.; Hensen, B.; Pfaff, W.; Koolstra, G.; Blok, M. S.; Robledo, L.; Taminiau, T.; Markham, M.; Twitchen, D. J.; Childress, L., Heralded entanglement between solid-state qubits separated by three metres. *Nature* **2013,** *497* (7447), 86-90.

121. Wahl, U.; Correia, J.; Villarreal, R.; Bourgeois, E.; Gulka, M.; Nesládek, M.; Vantomme, A.; Pereira, L., Direct Structural Identification and Quantification of the Split-Vacancy Configuration for Implanted Sn in Diamond. *Physical Review Letters* **2020,** *125* (4), 045301.

122. Goss, J.; Jones, R.; Breuer, S.; Briddon, P.; Öberg, S., The twelve-line 1.682 eV luminescence center in diamond and the vacancy-silicon complex. *Physical review letters* **1996,** *77* (14), 3041.

123. Goss, J.; Briddon, P.; Shaw, M., Density functional simulations of silicon-containing point defects in diamond. *Physical Review B* **2007,** *76* (7), 075204.

124. Bradac, C.; Gao, W.; Forneris, J.; Trusheim, M. E.; Aharonovich, I., Quantum nanophotonics with group IV defects in diamond. *Nature Communications* **2019,** *10* (1), 1-13.

125. Neu, E.; Steinmetz, D.; Riedrich-Möller, J.; Gsell, S.; Fischer, M.; Schreck, M.; Becher, C., Single photon emission from silicon-vacancy colour centres in chemical vapour deposition nano-diamonds on iridium. *New Journal of Physics* **2011,** *13* (2), 025012.

126. Hepp, C.; Müller, T.; Waselowski, V.; Becker, J. N.; Pingault, B.; Sternschulte, H.; Steinmüller-Nethl, D.; Gali, A.; Maze, J. R.; Atatüre, M., Electronic structure of the silicon vacancy color center in diamond. *Physical Review Letters* **2014,** *112* (3), 036405.

127. Jahnke, K. D.; Sipahigil, A.; Binder, J. M.; Doherty, M. W.; Metsch, M.; Rogers, L. J.; Manson, N. B.; Lukin, M. D.; Jelezko, F., Electron–phonon processes of the silicon-vacancy centre in diamond. *New Journal of Physics* **2015,** *17* (4), 043011.

128. Neu, E.; Agio, M.; Becher, C., Photophysics of single silicon vacancy centers in diamond: implications for single photon emission. *Optics express* **2012,** *20* (18), 19956-19971.

129. Rogers, L. J.; Jahnke, K. D.; Metsch, M. H.; Sipahigil, A.; Binder, J. M.; Teraji, T.; Sumiya, H.; Isoya, J.; Lukin, M. D.; Hemmer, P., All-optical initialization, readout, and coherent preparation of single silicon-vacancy spins in diamond. *Physical review letters* **2014,** *113* (26), 263602.

130. Evans, R. E.; Sipahigil, A.; Sukachev, D. D.; Zibrov, A. S.; Lukin, M. D., Narrow-linewidth homogeneous optical emitters in diamond nanostructures via silicon ion implantation. *Physical Review Applied* **2016,** *5* (4), 044010.

131. Sipahigil, A.; Jahnke, K. D.; Rogers, L. J.; Teraji, T.; Isoya, J.; Zibrov, A. S.; Jelezko, F.; Lukin, M. D., Indistinguishable photons from separated silicon-vacancy centers in diamond. *Physical review letters* **2014,** *113* (11), 113602.

132. Rogers, L. J.; Jahnke, K. D.; Teraji, T.; Marseglia, L.; Müller, C.; Naydenov, B.; Schauffert, H.; Kranz, C.; Isoya, J.; McGuinness, L. P., Multiple intrinsically identical single-photon emitters in the solid state. *Nature communications* **2014,** *5* (1), 1-6.

133. Gu, E.; Chen, W.-Y.; Gu, J.; Burridge, P.; Wu, J. C., Molecular imaging of stem cells: tracking survival, biodistribution, tumorigenicity, and immunogenicity. *Theranostics* **2012,** *2* (4), 335.

134. Urano, Y., Novel live imaging techniques of cellular functions and in vivo tumors based on precise design of small molecule-based 'activatable'fluorescence probes. *Current opinion in chemical biology* **2012,** *16* (5-6), 602-608.

135. Merson, T. D.; Castelletto, S.; Aharonovich, I.; Turbic, A.; Kilpatrick, T. J.; Turnley, A. M., Nanodiamonds with silicon vacancy defects for nontoxic photostable fluorescent labeling of neural precursor cells. *Optics letters* **2013,** *38* (20), 4170-4173.

136. Feng, T.; Schwartz, B. D., Characteristics and origin of the 1.681 eV luminescence center in chemical-vapor-deposited diamond films. *Journal of applied physics* **1993,** *73* (3), 1415-1425.

137. Turukhin, A.; Liu, C.-H.; Gorokhovsky, A.; Alfano, R.; Phillips, W., Picosecond photoluminescence decay of Si-doped chemical-vapor-deposited diamond films. *Physical Review B* **1996,** *54* (23), 16448.

138. Pingault, B.; Becker, J. N.; Schulte, C. H.; Arend, C.; Hepp, C.; Godde, T.; Tartakovskii, A. I.; Markham, M.; Becher, C.; Atatüre, M., All-optical formation of coherent dark states of silicon-vacancy spins in diamond. *Physical review letters* **2014,** *113* (26), 263601.

139. Iwasaki, T.; Ishibashi, F.; Miyamoto, Y.; Doi, Y.; Kobayashi, S.; Miyazaki, T.; Tahara, K.; Jahnke, K. D.; Rogers, L. J.; Naydenov, B., Germanium-vacancy single color centers in diamond. *Scientific reports* **2015,** *5*, 12882.

140. Palyanov, Y. N.; Kupriyanov, I. N.; Borzdov, Y. M.; Khokhryakov, A. F.; Surovtsev, N. V., High-Pressure Synthesis and Characterization of Ge-Doped Single Crystal Diamond. *Crystal Growth & Design* **2016,** *16* (6), 3510-3518.

141. Nadolinny, V.; Komarovskikh, A. Y.; Palyanov, Y. N.; Kupriyanov, I.; Borzdov, Y. M.; Rakhmanova, M.; Yuryeva, O.; Veber, S., EPR study of germanium-vacancy defects in diamonds. *Journal of Structural Chemistry* **2016,** *57* (5), 1041-1043.

142. Iwasaki, T.; Miyamoto, Y.; Taniguchi, T.; Siyushev, P.; Metsch, M. H.; Jelezko, F.; Hatano, M., Tin-vacancy quantum emitters in diamond. *Physical review letters* **2017,** *119* (25), 253601.

143. Ditalia Tchernij, S.; Luhmann, T.; Herzig, T.; Kupper, J.; Damin, A.; Santonocito, S.; Signorile, M.; Traina, P.; Moreva, E.; Celegato, F., Single-photon emitters in lead-implanted single-crystal diamond. *ACS Photonics* **2018,** *5* (12), 4864-4871.

144. Trusheim, M. E.; Pingault, B.; Wan, N. H.; De Santis, L.; Chen, K. C.; Walsh, M.; Rose, J. J.; Becker, J. N.; Lienhard, B.; Bersin, E., Transform-limited photons from a tin-vacancy spin in diamond. *arXiv preprint arXiv:1811.07777* **2018**.

145. Trusheim, M. E.; Pingault, B.; Wan, N. H.; Gündoğan, M.; De Santis, L.; Debroux, R.; Gangloff, D.; Purser, C.; Chen, K. C.; Walsh, M., Transform-limited photons from a coherent tin-vacancy spin in diamond. *Physical Review Letters* **2020,** *124* (2), 023602.

146. Sukachev, D. D.; Sipahigil, A.; Nguyen, C. T.; Bhaskar, M. K.; Evans, R. E.; Jelezko, F.; Lukin, M. D., Silicon-vacancy spin qubit in diamond: a quantum memory exceeding 10 ms with single-shot state readout. *Physical review letters* **2017,** *119* (22), 223602.

147. Siyushev, P.; Metsch, M. H.; Ijaz, A.; Binder, J. M.; Bhaskar, M. K.; Sukachev, D. D.; Sipahigil, A.; Evans, R. E.; Nguyen, C. T.; Lukin, M. D., Optical and microwave control of germanium-vacancy center spins in diamond. *Physical Review B* **2017,** *96* (8), 081201.

148. Boldyrev, K.; Mavrin, B.; Sherin, P. S.; Popova, M., Bright luminescence of diamonds with Ge-V centers. *Journal of Luminescence* **2018,** *193*, 119-124.

149. Teraji, T.; Yamamoto, T.; Watanabe, K.; Koide, Y.; Isoya, J.; Onoda, S.; Ohshima, T.; Rogers, L. J.; Jelezko, F.; Neumann, P., Homoepitaxial diamond film growth: High purity, high crystalline quality, isotopic enrichment, and single color center formation. *physica status solidi (a)* **2015,** *212* (11), 2365-2384.

150. Sedov, V.; Martyanov, A.; Savin, S.; Bolshakov, A.; Bushuev, E.; Khomich, A.; Kudryavtsev, O.; Krivobok, V.; Nikolaev, S.; Ralchenko, V., Growth of polycrystalline and single-crystal CVD diamonds with bright photoluminescence of Ge-V color centers using germane GeH4 as the dopant source. *Diamond and Related Materials* **2018,** *90*, 47-53.

151. Zhou, Y.; Mu, Z.; Adamo, G.; Bauerdick, S.; Rudzinski, A.; Aharonovich, I.; Gao, W.-b., Direct writing of single germanium vacancy center arrays in diamond. *New Journal of Physics* **2018,** *20* (12), 125004.

152. Riedrich-Möller, J.; Kipfstuhl, L.; Hepp, C.; Neu, E.; Pauly, C.; Mücklich, F.; Baur, A.; Wandt, M.; Wolff, S.; Fischer, M., One-and two-dimensional photonic crystal microcavities in single crystal diamond. *Nature nanotechnology* **2012,** *7* (1), 69-74.

153. Lee, J. C.; Aharonovich, I.; Magyar, A. P.; Rol, F.; Hu, E. L., Coupling of silicon-vacancy centers to a single crystal diamond cavity. *Optics express* **2012,** *20* (8), 8891-8897.

154. Atatüre, M.; Englund, D.; Vamivakas, N.; Lee, S.-Y.; Wrachtrup, J., Material platforms for spin-based photonic quantum technologies. *Nature Reviews Materials* **2018,** *3* (5), 38-51.

155. Zhang, G.; Cheng, Y.; Chou, J.-P.; Gali, A., Material platforms for defect qubits and single-photon emitters. *Applied Physics Reviews* **2020,** *7* (3), 031308.

156. Awschalom, D. D.; Hanson, R.; Wrachtrup, J.; Zhou, B. B., Quantum technologies with optically interfaced solid-state spins. *Nature Photonics* **2018,** *12* (9), 516-527.

157. Siampour, H.; Kumar, S.; Davydov, V. A.; Kulikova, L. F.; Agafonov, V. N.; Bozhevolnyi, S. I., On-chip excitation of single germanium vacancies in nanodiamonds embedded in plasmonic waveguides. *Light: Science & Applications* **2018,** *7* (1), 1-9.

158. Machielse, B.; Bogdanovic, S.; Meesala, S.; Gauthier, S.; Burek, M. J.; Joe, G.; Chalupnik, M.; Sohn, Y.-I.; Holzgrafe, J.; Evans, R. E., Quantum interference of

electromechanically stabilized emitters in nanophotonic devices. *Physical Review X* **2019,** *9* (3), 031022.

159. Benedikter, J.; Kaupp, H.; Hümmer, T.; Liang, Y.; Bommer, A.; Becher, C.; Krueger, A.; Smith, J. M.; Hänsch, T. W.; Hunger, D., Cavity-enhanced single-photon source based on the silicon-vacancy center in diamond. *Physical Review Applied* **2017,** *7* (2), 024031.

160. Häußler, S.; Benedikter, J.; Bray, K.; Regan, B.; Dietrich, A.; Twamley, J.; Aharonovich, I.; Hunger, D.; Kubanek, A., Diamond photonics platform based on silicon vacancy centers in a single-crystal diamond membrane and a fiber cavity. *Physical Review B* **2019,** *99* (16), 165310.

161. Bray, K.; Regan, B.; Trycz, A.; Previdi, R.; Seniutinas, G.; Ganesan, K.; Kianinia, M.; Kim, S.; Aharonovich, I., Single crystal diamond membranes and photonic resonators containing germanium vacancy color centers. *ACS Photonics* **2018,** *5* (12), 4817-4822.

162. Alkahtani, M.; Cojocaru, I.; Liu, X.; Herzig, T.; Meijer, J.; Küpper, J.; Lühmann, T.; Akimov, A. V.; Hemmer, P. R., Tin-vacancy in diamonds for luminescent thermometry. *Applied Physics Letters* **2018,** *112* (24), 241902.

163. Nguyen, C. T.; Evans, R. E.; Sipahigil, A.; Bhaskar, M. K.; Sukachev, D. D.; Agafonov, V. N.; Davydov, V. A.; Kulikova, L. F.; Jelezko, F.; Lukin, M. D., All-optical nanoscale thermometry with silicon-vacancy centers in diamond. *Applied Physics Letters* **2018,** *112* (20), 203102.

164. Plakhotnik, T.; Aman, H.; Chang, H.-C., All-optical single-nanoparticle ratiometric thermometry with a noise floor of 0.3 K Hz− 1/2. *Nanotechnology* **2015,** *26* (24), 245501.

165. Tomljenovic-Hanic, S.; Steel, M.; de Sterke, C. M.; Salzman, J., Diamond based photonic crystal microcavities. *Optics Express* **2006,** *14* (8), 3556-3562.

166. Magyar, A. P.; Lee, J. C.; Limarga, A. M.; Aharonovich, I.; Rol, F.; Clarke, D. R.; Huang, M.; Hu, E. L., Fabrication of thin, luminescent, single-crystal diamond membranes. *Applied Physics Letters* **2011,** *99* (8), 081913.

167. Ziegler, J. F.; Ziegler, M. D.; Biersack, J. P., SRIM–The stopping and range of ions in matter (2010). *Nuclear Instruments and Methods in Physics Research Section B: Beam Interactions with Materials and Atoms* **2010,** *268* (11-12), 1818-1823.

168. Bray, K.; Kato, H.; Previdi, R.; Sandstrom, R.; Ganesan, K.; Ogura, M.; Makino, T.; Yamasaki, S.; Magyar, A. P.; Toth, M., Single crystal diamond membranes for nanoelectronics. *Nanoscale* **2018,** *10* (8), 4028-4035.

169. Hiramatsu, M.; Hori, M., Aligned growth of single-walled and double-walled carbon nanotube films by control of catalyst preparation. *Carbon Nanotubes-Synthesis, Characterization, Applications* **2011**.

170. Goodwin, D. G., Scaling laws for diamond chemical-vapor deposition. I. Diamond surface chemistry. *Journal of Applied Physics* **1993,** *74* (11), 6888-6894.

171. Harris, S. J., Mechanism for diamond growth from methyl radicals. *Applied Physics Letters* **1990,** *56* (23), 2298-2300.

172. Harris, S. J.; Goodwin, D., Growth on the reconstructed diamond (100) surface. *The Journal of Physical Chemistry* **1993,** *97* (1), 23-28.

173. Farhat, S.; Findeling, C.; Silva, F.; Hassouni, K.; Gicquel, A., Role of the plasma composition at the surface on diamond growth. *Le Journal de Physique IV* **1998,** *8* (PR7), Pr7-391-Pr7-399.

174. Asmussen, J.; Reinhard, D., *Diamond films handbook*. CRC Press: 2002.

175. Prelas, M. A., *Handbook of industrial diamonds and diamond films*. Routledge: 2018.

176. Battaile, C.; Srolovitz, D.; Butler, J., Morphologies of diamond films from atomic-scale simulations of chemical vapor deposition. *Diamond and Related Materials* **1997,** *6* (9), 1198-1206.

177. Battaile, C.; Srolovitz, D.; Butler, J., A kinetic Monte Carlo method for the atomic-scale simulation of chemical vapor deposition: application to diamond. *Journal of applied physics* **1997,** *82* (12), 6293-6300.

178. Butler, J. E.; Woodin, R. L., Thin film diamond growth mechanisms. *Philosophical Transactions of the Royal Society of London. Series A: Physical and Engineering Sciences* **1993,** *342* (1664), 209-224.

179. Kamo, M.; Sato, Y.; Matsumoto, S.; Setaka, N., Diamond synthesis from gas phase in microwave plasma. *Journal of crystal growth* **1983,** *62* (3), 642-644.

180. Kamo, M.; Yurimoto, H.; Sato, Y., Epitaxial growth of diamond on diamond substrate by plasma assisted CVD. *Applied Surface Science* **1988,** *33*, 553-560.

181. Tokuda, N., Homoepitaxial diamond growth by plasma-enhanced chemical vapor deposition. *Novel Aspects of Diamond* **2019**, 1-29.

182. Cheng, C.-L.; Chang, H.-C.; Lin, J.-C.; Song, K.-J.; Wang, J.-K., Direct observation of hydrogen etching anisotropy on diamond single crystal surfaces. *Physical review letters* **1997,** *78* (19), 3713.

183. Wang, Z. L.; Bentley, J.; Clausing, R.; Heatherly, L.; Horton, L., Direct correlation of microtwin distribution with growth face morphology of CVD diamond films by a novel TEM technique. *Journal of materials research* **1994,** *9* (6), 1552-1561.

184. Geis, M., Growth of device-quality homoepitaxial diamond thin films. *MRS Online Proceedings Library (OPL)* **1989,** *162*.

185. Chu, C.; Hauge, R.; Margrave, J.; D'evelyn, M., Growth kinetics of (100),(110), and (111) homoepitaxial diamond films. *Applied physics letters* **1992,** *61* (12), 1393-1395.

186. Ackermann, L.; Kulisch, W., Investigation of diamond etching and growth by in situ scanning tunneling microscopy. *Diamond and related materials* **1999,** *8* (7), 1256-1260.

187. Maeda, H.; Ohtsubo, K.; Irie, M.; Ohya, N.; Kusakabe, K.; Morooka, S., Determination of diamond [100] and [111] growth rate and formation of highly oriented diamond film by microwave plasma-assisted chemical vapor deposition. *Journal of materials research* **1995,** *10* (12), 3115-3123.

188. Sakaguchi, I.; Nishitani-Gamo, M.; Loh, K. P.; Haneda, H.; Ando, T., Homoepitaxial growth and hydrogen incorporation on the chemical vapor deposited (111) diamond. *Journal of applied physics* **1999,** *86* (3), 1306-1310.

189. Achard, J.; Tallaire, A.; Sussmann, R.; Silva, F.; Gicquel, A., The control of growth parameters in the synthesis of high-quality single crystalline diamond by CVD. *Journal of Crystal Growth* **2005,** *284* (3-4), 396-405.

190. Zhou, W.; Wang, Z. L., *Scanning microscopy for nanotechnology: techniques and applications*. Springer science & business media: 2007.

191. Webb, R. H., Confocal optical microscopy. *Reports on Progress in Physics* **1996,** *59* (3), 427.

192. Goldstein, J. I.; Newbury, D. E.; Michael, J. R.; Ritchie, N. W.; Scott, J. H. J.; Joy, D. C., *Scanning electron microscopy and X-ray microanalysis*. Springer: 2017.

193. Filik, J., Raman spectroscopy: a simple, non-destructive way to characterise diamond and diamond-like materials. *Spectroscopy Europe* **2005,** *17* (5), 10.

194. Barnard, A. S., Diamond standard in diagnostics: nanodiamond biolabels make their mark. *Analyst* **2009,** *134* (9), 1751-1764.

195. Gao, L.; Shao, L.; Chen, B.-C.; Betzig, E., 3D live fluorescence imaging of cellular dynamics using Bessel beam plane illumination microscopy. *Nature protocols* **2014,** *9* (5), 1083-1101.

196. Juette, M. F.; Terry, D. S.; Wasserman, M. R.; Zhou, Z.; Altman, R. B.; Zheng, Q.; Blanchard, S. C., The bright future of single-molecule fluorescence imaging. *Current opinion in chemical biology* **2014,** *20*, 103-111.

197. Kusumi, A.; Tsunoyama, T. A.; Hirosawa, K. M.; Kasai, R. S.; Fujiwara, T. K., Tracking single molecules at work in living cells. *Nature chemical biology* **2014,** *10* (7), 524.

198. Lodahl, P.; Mahmoodian, S.; Stobbe, S., Interfacing single photons and single quantum dots with photonic nanostructures. *Reviews of Modern Physics* **2015,** *87* (2), 347.

199. Vaijayanthimala, V.; Cheng, P.-Y.; Yeh, S.-H.; Liu, K.-K.; Hsiao, C.-H.; Chao, J.-I.; Chang, H.-C., The long-term stability and biocompatibility of fluorescent nanodiamond as an in vivo contrast agent. *Biomaterials* **2012,** *33* (31), 7794-7802.

200. Ho, D.; Wang, C.-H. K.; Chow, E. K.-H., Nanodiamonds: The intersection of nanotechnology, drug development, and personalized medicine. *Science Advances* **2015,** *1* (7), e1500439.

201. Ermakova, A.; Pramanik, G.; Cai, J.-M.; Algara-Siller, G.; Kaiser, U.; Weil, T.; Tzeng, Y.-K.; Chang, H.-C.; McGuinness, L.; Plenio, M. B., Detection of a few metallo-protein molecules using color centers in nanodiamonds. *Nano letters* **2013,** *13* (7), 3305-3309.

202. Neumann, P.; Jakobi, I.; Dolde, F.; Burk, C.; Reuter, R.; Waldherr, G.; Honert, J.; Wolf, T.; Brunner, A.; Shim, J. H., High-precision nanoscale temperature sensing using single defects in diamond. *Nano letters* **2013,** *13* (6), 2738-2742.

203. Schröder, T.; Mouradian, S. L.; Zheng, J.; Trusheim, M. E.; Walsh, M.; Chen, E. H.; Li, L.; Bayn, I.; Englund, D., Quantum nanophotonics in diamond. *JOSA B* **2016,** *33* (4), B65-B83.

204. Lenzini, F.; Gruhler, N.; Walter, N.; Pernice, W. H., Diamond as a Platform for Integrated Quantum Photonics (Adv. Quantum Technol. 3/2018). *Advanced Quantum Technologies* **2018,** *1* (3), 1870031.

205. Eaton, S. M.; Hadden, J. P.; Bharadwaj, V.; Forneris, J.; Picollo, F.; Bosia, F.; Sotillo, B.; Giakoumaki, A. N.; Jedrkiewicz, O.; Chiappini, A., Quantum micro–nano devices fabricated in diamond by femtosecond laser and ion irradiation. *Advanced Quantum Technologies* **2019,** *2* (5-6), 1900006.

206. Piracha, A. H.; Rath, P.; Ganesan, K.; Kühn, S.; Pernice, W. H.; Prawer, S., Scalable fabrication of integrated nanophotonic circuits on arrays of thin single crystal diamond membrane windows. *Nano letters* **2016,** *16* (5), 3341-3347.

207. Piracha, A. H.; Ganesan, K.; Lau, D. W.; Stacey, A.; McGuinness, L. P.; Tomljenovic-Hanic, S.; Prawer, S., Scalable fabrication of high-quality, ultra-thin single crystal diamond membrane windows. *Nanoscale* **2016,** *8* (12), 6860-6865.

208. Aharonovich, I.; Lee, J. C.; Magyar, A. P.; Buckley, B. B.; Yale, C. G.; Awschalom, D. D.; Hu, E. L., Homoepitaxial growth of single crystal diamond membranes for quantum information processing. *Advanced materials* **2012,** *24* (10), OP54-OP59.

209. Crane, M. J.; Petrone, A.; Beck, R. A.; Lim, M. B.; Zhou, X.; Li, X.; Stroud, R. M.; Pauzauskie, P. J., High-pressure, high-temperature molecular doping of nanodiamond. *Science advances* **2019,** *5* (5), eaau6073.

210. Ekimov, E.; Kondrin, M.; Krivobok, V.; Khomich, A.; Vlasov, I.; Khmelnitskiy, R.; Iwasaki, T.; Hatano, M., Effect of Si, Ge and Sn dopant elements on structure and photoluminescence of nano-and microdiamonds synthesized from organic compounds. *Diamond and Related Materials* **2019,** *93*, 75-83.

211. Sipahigil, A.; Evans, R. E.; Sukachev, D. D.; Burek, M. J.; Borregaard, J.; Bhaskar, M. K.; Nguyen, C. T.; Pacheco, J. L.; Atikian, H. A.; Meuwly, C.; Camacho, R. M.; Jelezko, F.; Bielejec, E.; Park, H.; Lončar, M.; Lukin, M. D., An integrated diamond nanophotonics platform for quantum optical networks. *Science* **2016,** *354*, 847.

212. Kalb, N.; Reiserer, A. A.; Humphreys, P. C.; Bakermans, J. J. W.; Kamerling, S. J.; Nickerson, N. H.; Benjamin, S. C.; Twitchen, D. J.; Markham, M.; Hanson, R., Entanglement distillation between solid-state quantum network nodes. *Science* **2017,** *356* (6341), 928-932.

213. Aslam, N.; Pfender, M.; Neumann, P.; Reuter, R.; Zappe, A.; Fávaro de Oliveira, F.; Denisenko, A.; Sumiya, H.; Onoda, S.; Isoya, J.; Wrachtrup, J., Nanoscale nuclear magnetic resonance with chemical resolution. *Science* **2017,** *357* (6346), 67-71.

214. Acosta, V. M.; Santori, C.; Faraon, A.; Huang, Z.; Fu, K. M. C.; Stacey, A.; Simpson, D. A.; Ganesan, K.; Tomljenovic-Hanic, S.; Greentree, A. D.; Prawer, S.; Beausoleil, R. G., Dynamic Stabilization of the Optical Resonances of Single Nitrogen-Vacancy Centers in Diamond. *Phys. Rev. Lett.* **2012,** *108* (20).

215. Schmidgall, E. R.; Chakravarthi, S.; Gould, M.; Christen, I. R.; Hestroffer, K.; Hatami, F.; Fu, K.-M. C., Frequency Control of Single Quantum Emitters in Integrated Photonic Circuits. *Nano Lett.* **2018**.

216. Neu, E.; Steinmetz, D.; Riedrich-Moeller, J.; Gsell, S.; Fischer, M.; Schreck, M.; Becher, C., Single photon emission from silicon-vacancy centres in CVD-nano-diamonds on iridium *New J. Phys.* **2011,** *13*, 025012.

217. Becker, J. N.; Görlitz, J.; Arend, C.; Markham, M.; Becher, C., Ultrafast all-optical coherent control of single silicon vacancy colour centres in diamond. *Nat. Commun.* **2016,** *7*, 13512.

218. Hepp, C.; Müller, T.; Waselowski, V.; Becker, J. N.; Pingault, B.; Sternschulte, H.; Steinmüller-Nethl, D.; Gali, A.; Maze, J. R.; Atatüre, M.; Becher, C., Electronic Structure of the Silicon Vacancy Color Center in Diamond. *Phys. Rev. Lett.* **2014,** *112* (3), 036405.

219. Zhou, Y.; Rasmita, A.; Li, K.; Xiong, Q.; Aharonovich, I.; Gao, W.-b., Coherent control of a strongly driven silicon vacancy optical transition in diamond. *Nat. Commun.* **2017,** *8*, 14451.

220. Zhang, J. L.; Ishiwata, H.; Babinec, T. M.; Radulaski, M.; Müller, K.; Lagoudakis, K. G.; Dory, C.; Dahl, J.; Edgington, R.; Soulière, V.; Ferro, G.; Fokin, A. A.; Schreiner, P. R.; Shen, Z.-X.; Melosh, N. A.; Vučković, J., Hybrid Group IV Nanophotonic Structures Incorporating Diamond Silicon-Vacancy Color Centers. *Nano Lett.* **2016,** *16* (1), 212-217.

221. Rogers, L. J.; Jahnke, K. D.; Teraji, T.; Marseglia, L.; Müller, C.; Naydenov, B.; Schauffert, H.; Kranz, C.; Isoya, J.; McGuinness, L. P.; Jelezko, F., Multiple intrinsically identical single-photon emitters in the solid state. *Nat. Commun.* **2014,** *5*, 4739.

222. Arend, C.; Becker, J. N.; Sternschulte, H.; Steinmüller-Nethl, D.; Becher, C., Photoluminescence excitation and spectral hole burning spectroscopy of silicon vacancy centers in diamond. *Physical Review B* **2016,** *94* (4), 045203.

223. Jahnke, K. D.; Sipahigil, A.; Binder, J.; Doherty, M. W.; Metsch, M.; Rogers, L. J.; Manson, N. B.; Lukin, M. D.; Jelezko, F., Electron–phonon processes of the silicon-vacancy centre in diamond. *New J. Phys.* **2015,** *17* (4), 043011.

224. Bhaskar, M. K.; Sukachev, D. D.; Sipahigil, A.; Evans, R. E.; Burek, M. J.; Nguyen, C. T.; Rogers, L. J.; Siyushev, P.; Metsch, M. H.; Park, H.; Jelezko, F.; Lončar, M.; Lukin, M. D., Quantum Nonlinear Optics with a Germanium-Vacancy Color Center in a Nanoscale Diamond Waveguide. *Phys. Rev. Lett.* **2017,** *118* (22), 223603.

225. Siyushev, P.; Metsch, M. H.; Ijaz, A.; Binder, J. M.; Bhaskar, M. K.; Sukachev, D. D.; Sipahigil, A.; Evans, R. E.; Nguyen, C. T.; Lukin, M. D.; Hemmer, P. R.; Palyanov, Y. N.; Kupriyanov, I. N.; Borzdov, Y. M.; Rogers, L. J.; Jelezko, F., Optical and microwave control of germanium-vacancy center spins in diamond. *Phys. Rev. B* **2017,** *96* (8), 081201.

226. Boldyrev, K. N.; Mavrin, B. N.; Sherin, P. S.; Popova, M. N., Bright luminescence of diamonds with Ge-V centers. *J. Lumin.* **2018,** *193*, 119-124.

227. Iwasaki, T.; Ishibashi, F.; Miyamoto, Y.; Doi, Y.; Kobayashi, S.; Miyazaki, T.; Tahara, K.; Jahnke, K. D.; Rogers, L. J.; Naydenov, B.; Jelezko, F.; Yamasaki, S.; Nagamachi, S.; Inubushi, T.; Mizuochi, N.; Hatano, M., Germanium-Vacancy Single Color Centers in Diamond. *Scientific Reports* **2015,** *5*, 12882.

228. Ralchenko, V. G.; Sedov, V. S.; Khomich, A. A.; Krivobok, V. S.; Nikolaev, S. N.; Savin, S. S.; Vlasov, I. I.; Konov, V. I., Observation of the Ge-vacancy color center in microcrystalline diamond films. *Bulletin of the Lebedev Physics Institute* **2015,** *42* (6), 165-168.

229. Tchernij, S. D.; Herzig, T.; Forneris, J.; Küpper, J.; Pezzagna, S.; Traina, P.; Moreva, E.; Degiovanni, I. P.; Brida, G.; Skukan, N.; Genovese, M.; Jakšić, M.; Meijer, J.; Olivero, P., Single-Photon-Emitting Optical Centers in Diamond Fabricated upon Sn Implantation. *ACS Photonics* **2017,** *4* (10), 2580-2586.

230. Li, K.; Zhou, Y.; Rasmita, A.; Aharonovich, I.; Gao, W. B., Nonblinking Emitters with Nearly Lifetime-Limited Linewidths in CVD Nanodiamonds. *Physical Review Applied* **2016,** *6* (2), 024010.

231. Evans, R. E.; Sipahigil, A.; Sukachev, D. D.; Zibrov, A. S.; Lukin, M. D., Narrow-Linewidth Homogeneous Optical Emitters in Diamond Nanostructures via Silicon Ion Implantation. *Physical Review Applied* **2016,** *5*, 044010.

232. Meesala, S.; Sohn, Y.-I.; Pingault, B.; Shao, L.; Atikian, H. A.; Holzgrafe, J.; Gündoğan, M.; Stavrakas, C.; Sipahigil, A.; Chia, C.; Evans, R.; Burek, M. J.; Zhang, M.; Wu, L.; Pacheco, J. L.; Abraham, J.; Bielejec, E.; Lukin, M. D.; Atatüre, M.; Lončar, M., Strain engineering of the silicon-vacancy center in diamond. *Phys. Rev. B* **2018,** *97* (20), 205444.

233. Becker, J. N.; Pingault, B.; Groß, D.; Gündoğan, M.; Kukharchyk, N.; Markham, M.; Edmonds, A.; Atatüre, M.; Bushev, P.; Becher, C., All-Optical Control of the Silicon-Vacancy Spin in Diamond at Millikelvin Temperatures. *Phys. Rev. Lett.* **2018,** *120* (5), 053603.

234. Schröder, T.; Mouradian, S. L.; Zheng, J.; Trusheim, M. E.; Walsh, M.; Chen, E. H.; Li, L.; Bayn, I.; Englund, D., Quantum nanophotonics in diamond [Invited]. *J. Opt. Soc. Am. B* **2016,** *33* (4), B65-B83.

235. Mouradian, S. L.; Schröder, T.; Poitras, C. B.; Li, L.; Goldstein, J.; Chen, E. H.; Walsh, M.; Cardenas, J.; Markham, M. L.; Twitchen, D. J.; Lipson, M.; Englund, D., Scalable Integration of Long-Lived Quantum Memories into a Photonic Circuit. *Physical Review X* **2015,** *5* (3), 031009.

236. Burek, M. J.; Meuwly, C.; Evans, R. E.; Bhaskar, M. K.; Sipahigil, A.; Meesala, S.; Machielse, B.; Sukachev, D. D.; Nguyen, C. T.; Pacheco, J. L.; Bielejec, E.; Lukin, M. D.; Lončar, M., Fiber-Coupled Diamond Quantum Nanophotonic Interface. *Physical Review Applied* **2017,** *8* (2), 024026.

237. Riedrich-Möller, J.; Arend, C.; Pauly, C.; Mücklich, F.; Fischer, M.; Gsell, S.; Schreck, M.; Becher, C., Deterministic Coupling of a Single Silicon-Vacancy Color Center to a Photonic Crystal Cavity in Diamond. *Nano Lett.* **2014,** *14* (9), 5281-5287.

238. Magyar, A.; Lee, J. C.; Limarga, A. M.; Aharonovich, I.; Rol, F.; Clarke, D. R.; Huang, M. B.; Hu, E. L., Fabrication of Thin, Luminescent, Single-crystal Diamond Membranes. *Appl. Phys. Lett.* **2011,** *99*, 081913.

239. Olivero, P.; Rubanov, S.; Reichart, P.; Gibson, B. C.; Huntington, S. T.; Rabeau, J.; Greentree, A. D.; Salzman, J.; Moore, D.; Jamieson, D. N.; Prawer, S., Ion-beam-assisted lift-off technique for three-dimensional micromachining of freestanding single-crystal diamond. *Adv. Mater.* **2005,** *17* (20), 2427.

240. Zhu, X.; Saito, S.; Kemp, A.; Kakuyanagi, K.; Karimoto, S.-i.; Nakano, H.; Munro, W. J.; Tokura, Y.; Everitt, M. S.; Nemoto, K.; Kasu, M.; Mizuochi, N.; Semba, K., Coherent coupling of a superconducting flux qubit to an electron spin ensemble in diamond. *Nature* **2011,** *478* (7368), 221-224.

241. Zhong, T.; Kindem, J. M.; Miyazono, E.; Faraon, A., Nanophotonic coherent light–matter interfaces based on rare-earth-doped crystals. *Nat. Commun.* **2015,** *6*, 8206.

242. Faraon, A.; Santori, C.; Huang, Z. H.; Acosta, V. M.; Beausoleil, R. G., Coupling of Nitrogen-Vacancy Centers to Photonic Crystal Cavities in Monocrystalline Diamond. *Phys. Rev. Lett.* **2012,** *109* (3).

243. Mitchell, M.; Khanaliloo, B.; Lake, D. P.; Masuda, T.; Hadden, J. P.; Barclay, P. E., Single-crystal diamond low-dissipation cavity optomechanics. *Optica* **2016,** *3* (9), 963-970.

244. Bray, K.; Sandstrom, R.; Elbadawi, C.; Fischer, M.; Schreck, M.; Shimoni, O.; Lobo, C.; Toth, M.; Aharonovich, I., Localization of narrowband single photon emitters in nanodiamonds. *ACS applied materials & interfaces* **2016,** *8* (11), 7590-7594.

245. Radulaski, M.; Zhang, J. L.; Tzeng, Y. K.; Lagoudakis, K. G.; Ishiwata, H.; Dory, C.; Fischer, K. A.; Kelaita, Y. A.; Sun, S.; Maurer, P. C., Nanodiamond integration with photonic devices. *Laser & Photonics Reviews* **2019,** *13* (8), 1800316.

246. Bogdanov, S. I.; Shalaginov, M. Y.; Lagutchev, A. S.; Chiang, C.-C.; Shah, D.; Baburin, A. S.; Ryzhikov, I. A.; Rodionov, I. A.; Kildishev, A. V.; Boltasseva, A., Ultrabright room-temperature sub-nanosecond emission from single nitrogen-vacancy centers coupled to nanopatch antennas. *Nano letters* **2018,** *18* (8), 4837-4844.

247. Evans, R. E.; Bhaskar, M. K.; Sukachev, D. D.; Nguyen, C. T.; Sipahigil, A.; Burek, M. J.; Machielse, B.; Zhang, G. H.; Zibrov, A. S.; Bielejec, E., Photon-mediated interactions between quantum emitters in a diamond nanocavity. *Science* **2018,** *362* (6415), 662-665.

248. Bradley, C.; Randall, J.; Abobeih, M.; Berrevoets, R.; Degen, M.; Bakker, M.; Markham, M.; Twitchen, D.; Taminiau, T., A ten-qubit solid-state spin register with quantum memory up to one minute. *Physical Review X* **2019,** *9* (3), 031045.

249. Bhaskar, M. K.; Sukachev, D. D.; Sipahigil, A.; Evans, R. E.; Burek, M. J.; Nguyen, C. T.; Rogers, L. J.; Siyushev, P.; Metsch, M. H.; Park, H., Quantum nonlinear optics with a germanium-vacancy color center in a nanoscale diamond waveguide. *Physical review letters* **2017,** *118* (22), 223603.

250. Malykhin, S.; Mindarava, Y.; Ismagilov, R.; Orekhov, A.; Jelezko, F.; Obraztsov, A., Formation of GeV, SiV, and NV Color Centers in Single Crystal Diamond Needles Grown by Chemical Vapor Deposition. *physica status solidi (b)* **2019,** *256* (9), 1800721.

251. Chen, D.; Mu, Z.; Zhou, Y.; Fröch, J. E.; Rasmit, A.; Diederichs, C.; Zheludev, N.; Aharonovich, I.; Gao, W.-b., Optical gating of resonance fluorescence from a single germanium vacancy color center in diamond. *Physical review letters* **2019,** *123* (3), 033602.

252. Rugar, A. E.; Lu, H.; Dory, C.; Sun, S.; McQuade, P. J.; Shen, Z.-X.; Melosh, N. A.; Vuckovic, J., Generation of Tin-Vacancy Centers in Diamond via Shallow Ion Implantation and Subsequent Diamond Overgrowth. *Nano Letters* **2020,** *20* (3), 1614-1619.

253. Aharonovich, I.; Lee, J. C.; Magyar, A. P.; Buckley, B. B.; Yale, C. G.; Awschalom, D. D.; Hu, E. L., Homoepitaxial Growth of Single Crystal Diamond Membranes for Quantum Information Processing. *Adv. Mater.* **2012,** *24*, OP54-OP59.

254. Piracha, A. H.; Rath, P.; Ganesan, K.; Kühn, S.; Pernice, W. H. P.; Prawer, S., Scalable Fabrication of Integrated Nanophotonic Circuits on Arrays of Thin Single Crystal Diamond Membrane Windows. *Nano Lett.* **2016,** *16* (5), 3341-3347.

255. Wang, W.; Ramezani, M.; Väkeväinen, A. I.; Törmä, P.; Rivas, J. G.; Odom, T. W., The rich photonic world of plasmonic nanoparticle arrays. *Materials today* **2018,** *21* (3), 303-314.

256. Wang, D.; Guan, J.; Hu, J.; Bourgeois, M. R.; Odom, T. W., Manipulating light–matter interactions in plasmonic nanoparticle lattices. *Accounts of chemical research* **2019,** *52* (11), 2997-3007.

257. Henzie, J.; Lee, J.; Lee, M. H.; Hasan, W.; Odom, T. W., Nanofabrication of plasmonic structures. *Annual review of physical chemistry* **2009,** *60*, 147-165.

258. Yang, A.; Hoang, T. B.; Dridi, M.; Deeb, C.; Mikkelsen, M. H.; Schatz, G. C.; Odom, T. W., Real-time tunable lasing from plasmonic nanocavity arrays. *Nature communications* **2015,** *6* (1), 1-7.

259. Kravets, V. G.; Kabashin, A. V.; Barnes, W. L.; Grigorenko, A. N., Plasmonic surface lattice resonances: a review of properties and applications. *Chemical reviews* **2018,** *118* (12), 5912-5951.

260. Trycz, A.; Regan, B.; Kianinia, M.; Bray, K.; Toth, M.; Aharonovich, I., Bottom up engineering of single crystal diamond membranes with germanium vacancy color centers. *Optical Materials Express* **2019,** *9* (12), 4708-4715.